Performance Testing and Modeling of Printed Circuit Heat Exchangers for Advanced Nuclear Reactor Applications

by

Minghui Chen

A dissertation submitted in partial fulfillment
of the requirements for the degree of
Doctor of Philosophy
(Nuclear Engineering and Radiological Sciences)
in the University of Michigan
2018

Doctoral Committee:

Professor Xiaodong Sun, Chair
Professor Richard N. Christensen, The Ohio State University and University of Idaho
Professor Annalisa Manera
Assistant Research Scientist Victor Petrov
Professor Kevin Pipe

Minghui Chen

chenum@umich.edu

ORCID ID: 0000-0002-7380-3037

This dissertation is dedicated to my parents for their endless love,

support,

and encouragement.

Acknowledgements

This research was performed using funding received from the U.S. Department of Energy Office of Nuclear Energy. I want to thank the following people for their support during my study.

First and foremost, I wish to express my deepest gratitude to my advisor Professor Xiaodong Sun for his expert guidance and support all the time. I am very thankful to Professor Richard N. Christensen for his encouragement and numerous valuable suggestions throughout the entire research work. This work would not have been completed without their efforts.

I would like to thank my committee members, Professor Annalisa Manera, Dr. Victor Petrov, and Professor Kevin Pipe for their willingness to help and providing me valuable feedback on my research work. I would also like to thank Professor Fei Gao for his comments during my prospectus exam.

Many thanks to Professor Vivek Utgikar (University of Idaho) and Dr. Piyush Sabharwall (Idaho National Laboratory) for their advice on the heat exchanger design and testing. Special thanks must go to Dr. James E. O'Brien (Idaho National Laboratory) for providing me an opportunity to work at Idaho National Laboratory as an intern. It would be remiss of me if I do not acknowledge the assistance from Dr. Su-Jong Yoon (Idaho National Laboratory) on the PCHE simulations.

I would like to thank all my friends for their help and for making my graduate life enjoyable at both The Ohio State University and the University of Michigan. A special thank you to Dr. Qiuping Lv for his friendship and help that have made the past a few years a lot easier. I would like to personally thank David Arcilesi, Dr. Benjamin Doup, Juanjuan Guo, Dr. Tae Kyu Ham, Dr. Inhun Kim, Hsun-Chia Lin, Qingqing Liu, Yalan Qian, Dr. Shanbin Shi, Chengqi Wang, Dr. Limin Wang, Kevin Wegman, Xiao Wu, Dr. Xinquan Zhou, Sheng Zhang, and Xiaoqin Zhang for making laboratory life enjoyable.

Last but not least, I want to express my great appreciation of my family. Mom and Dad, words cannot describe my thanks for the support and endless love you have provided with throughout these difficult years. I love you both more than anything.

Table of Contents

List of Figures

List of Tables

Abstract

The primary mission of very-high-temperature reactors (VHTRs) is to generate electricity and provide high-temperature process heat for industrial applications with high efficiency, which relies on an effective intermediate heat exchanger (IHX) that transfers heat from the primary fluid (i.e., helium) to a secondary fluid. A printed circuit heat exchanger (PCHE) is one of the leading IHX candidates to be employed in VHTRs due to its compactness and capability for high-temperature, high-pressure applications with high effectiveness.

In this study, the thermal-hydraulic performance of a fabricated zigzag-channel PCHE was investigated. New pressure drop and heat transfer correlations were developed based on the experimental data. Local thermal-hydraulic performance of the PCHE indicated that fully-developed flow conditions were never achieved, which was attributed to the wavy nature of zigzag flow channels as well as the large temperature variations along the flow direction. This study concluded that heat transfer discrepancies between the hot side and cold side were caused by the differences in both thermal boundary conditions and thermophysical properties. Several effects on the PCHE's thermal-hydraulic performance were also studied, including the fluid and solid thermophysical properties, radiuses of curvature at zigzag bends, channel configurations, channel pitch lengths in the fluid flow direction, and zigzag pitch angles. It was found that the mean pressure loss factors and mean Nusselt numbers in zigzag channels with sharp bends were 4–6% larger than those in zigzag channels with bends with a curvature radius of 4 mm. A multi-objective

optimization for the PCHE's geometry was conducted based on the numerically obtained correlations. A total number of 142 points on the Pareto front were obtained. Users can select the optimal geometrical parameters for the zigzag-channel PCHE designs from the obtained Pareto front based on their needs. In addition, the stress field of a simplified three-dimensional geometry was obtained. It was observed that the highest stress occurred at diffusion-bonded interfaces and that it was less than the maximum allowable stress of the structural material.

Furthermore, a computer code was developed to predict both the steady-state and transient behaviors of both straight-channel and zigzag-channel PCHEs. Comparisons of the numerical results with the experimental data indicated that the dynamic model was successful in predicting the experimental transient scenarios. The numerical results could also provide useful insight on control strategy development for an integrated high-temperature reactor system with process heat applications, for instance, using the helium mass flow rates or helium inlet temperatures variations to adjust the heat exchanger effectiveness and heat transfer rate.

Finally, the heat exchanger model was implemented into a system dynamic code to simulate the transient behavior of a 20-MWth Fluoride-salt-cooled High-temperature Reactor (FHR). Results were obtained for three initiating events: a positive reactivity insertion, a step increase of the helium flow rate, and a step increase of the helium inlet temperature to the secondary heat exchanger (SHX). The results demonstrated that the FHR reactor, for the three transient scenarios analyzed, had inherent safety features. The results also showed that the intermediate loop consisting of the IHX and SHX played a significant role in the transient progression of the integral system.

This study provides critical insights into the thermal-hydraulic performance of PCHEs that can be applied to nuclear power, offshore industry, solar power, dual cycles for process heat applications, and cooling of electronics and fuel cells.

Chapter 1 Introduction

1.1 Background

According to the U.S. Energy Information Administration's (EIA's) 2017 International Energy Outlook, the global energy consumption is expected to increase 28% between 2015 and 2040 (EIA, 2017). Nuclear power plants currently generate 11% of the world's electricity. It is projected that nuclear power is the world's second fastest-growing source of energy and will increase by an average of 1.5% per year between 2015 and 2040. In the United States, nuclear power currently accounts for about 20% of all electricity generation and more than 60% of clean electric power generation. Most of the world's nuclear power is generated by second- and third-generation nuclear power plants. Although a significant share of existing nuclear plants will be retired in the 2030s, rising demand for clean electricity from all over the world will stimulate nuclear energy development. To achieve safety, reliability, sustainability, economic competitiveness, and proliferation resistance for future nuclear power, technologies are required to be improved in nuclear energy development. The Generation IV International Forum was formed to further promote nuclear energy to fulfill future energy needs (Abrams et al., 2002). Significant effort in the U.S. was invested in new technology development for next generation nuclear plants (NGNPs).

The very-high-temperature reactor (VHTR) is one promising candidate for the NGNP due to its capability of generating electricity with high efficiencies and providing high-temperature process

heat for industrial applications. The VHTR nuclear heat supply system (NHSS) consists of a helium-cooled, graphite-moderated, thermal neutron spectrum reactor and an intermediate heat transport loop. There are two reactor core concepts, namely, the prismatic block and the pebble bed. The NHSS is designed with the capability of delivering high-pressure, high-temperature helium to a power conversion unit (PCU) for electricity production and an industrial plant for heat process applications. The helium temperature at the reactor core outlet is reduced to 800 °C in the first stage and would then be increased to 1,000 °C or above in later development stages (Nestell and Sam, 2015). The VHTR can be utilized for a number of applications with such high coolant outlet temperatures. The electric power production may use a Rankine cycle through a high-pressure steam generator, a direct Brayton cycle gas turbine using the primary helium coolant as the working fluid, or an indirect-cycle gas turbine using a secondary helium fluid. The process heat applications may include hydrogen production, coal gasification, petroleum refining, bio-fuel production, and production of chemical feed stocks for use in the fertilizer and chemical industries (Mylavarapu, 2011).

The efficiency of electricity generation and process heat applications of VHTRs is significantly dependent upon intermediate heat exchangers (IHXs). An IHX is a key component for transferring thermal energy from the primary coolant to a secondary coolant, which could be helium, supercritical carbon dioxide (sCO_2), or molten salt. In addition, an IHX serves as an interface that isolates the VHTR primary system from the plant for electricity generation and process heat applications. Therefore, it must be sufficiently robust to maintain the entire system integrity during normal and off-normal conditions. Since helium typically has low heat transfer capability due to its low volumetric thermal capacity and low thermal conductivity, a compact heat exchanger with

a high surface area to volume ratio, generally has 700 m^2/m^3 or higher (Shah and Sekulic, 2003), is preferable to be employed as an IHX in VHTRs. Printed circuit heat exchanger (PCHE) stands out from several heat exchanger candidates due to its high effectiveness, compactness, robustness, and its ability to withstand high pressures and temperatures. The first PCHE was developed in Australia during the 1980s and a company called Heatric was founded based on that PCHE fabrication technology (Heatric, 2017). PCHEs are plate-type compact heat exchangers in which flow channels (typically, with small hydraulic diameters) are etched into flat metal plates using a photochemical machining process. There are several PCHE designs with respect to the flow channel geometries, such as straight, zigzag, S-shape finned, and airfoil finned channels. The etched metal plates are grinded and lapped to remove any scratches on the plate surfaces and then are made flat and parallel. Finally, the etched plates are stacked together with a prescribed arrangement configuration and diffusion bonded to create a high-integrity solid block before flow distribution headers are attached to the heat exchanger block (Heatric, 2017; Mylavarapu et al., 2009; Chen et al., 2015a; and Chen et al., 2015c).

1.2 Literature Review of Studies on PCHEs

Little attention was paid to PCHEs for their application on advanced nuclear reactors during their early development. Studies focused on the primary side and power conversion system and treated the PCHE-type IHX as a simplified interface (Wang, 2003; Gezelius, 2004; and Dostal, 2004). Many studies have been conducted on PCHEs in recent years that can be divided into four categories: experimental and numerical studies on their thermal-hydraulic performance, optimization of their geometrical parameters, stress analysis of their mechanical integrity, and

studies on their dynamic behavior. In what follows, a literature review on each of these four categories is presented.

1.2.1 On steady-state thermal-hydraulic performance

A number of studies have been performed on the steady-state thermal-hydraulic performance of PCHEs in recent years. Nikitin et al. (2006) investigated the heat transfer and pressure drop characteristics of a 3-kW PCHE with a compactness of 1050 m^2/m^3 in an sCO_2 loop. The PCHE comprised zigzag channels and the working fluid was sCO_2 on both the hot and cold sides. It was found that the overall heat transfer coefficients varied from 300 to 650 $W/(m^2\text{-}K)$. Further investigation on the pressure loss due to various channel shapes was conducted by Tsuzuki et al. (2007), which included performing three-dimensional (3-D) thermal-hydraulic simulations of a PCHE with S-shape finned channels. The authors concluded that the PCHE with S-shape finned channels showed similar thermal performance as the PCHE with zigzag channels, while it reduced pressure loss by approximately 20%. An experimental study was carried out by Ngo et al. (2007) to investigate the thermal-hydraulic characteristics of PCHEs with zigzag and S-shape finned channels. They found that both PCHEs had higher heat transfer performance than conventional shell-and-tube heat exchangers. However, the PCHE with zigzag channels had a 24–34% higher Nusselt number than the PCHE with S-shape finned channels, while the pressure drop in the zigzag channels was 4 to 5 times larger than that in the S-shape finned channels for the same Reynolds numbers. Both studies indicated that the thermal-hydraulic performance of PCHEs was a strong function of channel shape and geometrical parameters.

These studies mainly focused on the thermal-hydraulic performance of PCHEs with a working fluid of sCO_2. There are also many studies on PCHEs utilizing different fluid combinations, such as air, nitrogen, and helium gases. Song (2005) tested a PCHE using air as the working fluid in a low Reynolds number region. Friction factors in the wavy channels were found to be about 50% larger than those in straight circular pipes for the same Reynolds number range. Kim (2012) conducted comprehensive numerical and experimental studies on zigzag-channel PCHEs based on helium-helium, helium-water, and gas mixture (helium and CO_2)-water working fluid combinations. The global Nusselt number correlation was found to be inapplicable for predicting the local Nusselt number in zigzag channels. It was also found that the log-mean temperature difference (LMTD) method was ineffective for PCHE designs when the temperature differences were significant on either side. Correlations for calculating Fanning friction factors and Nusselt numbers were proposed for zigzag-channel PCHEs.

Mylavarapu et al. (2012) designed and constructed a high-temperature helium test facility (HTHF) that could facilitate compact heat exchanger thermal-hydraulic testing using helium as the working fluid at temperatures and pressures up to 800 °C and 3.0 MPa with helium mass flow rates ranging from 15 to 49 kg/h. Two similar straight-channel PCHEs were fabricated using Alloy 617 plates for the heat exchanger cores and were tested in the HTHF in the counter-flow configuration to gauge their thermal-hydraulic performance (Mylavarapu et al., 2014). The authors proposed correlations to determine the hydrodynamic entrance length and Fanning friction factor in the entrance region for the laminar flow in semicircular ducts (Mylavarapu et al., 2016). Figley et al. (2013) conducted a numerical study on the thermal-hydraulic performance of a straight-channel PCHE using FLUENT based on the study performed by Mylavarapu et al. (2012). Convective heat

transfer coefficients and Fanning friction factors were obtained for both the laminar and laminar-to-transition flow regimes. The laminar viscous model was selected for the laminar flow cases, while the standard k-ω turbulence model was used for the transition flow cases. Flow transitions were observed at the Reynolds numbers of 2,300 and 3,100 for circular and semicircular straight channels, respectively. Bartel et al. (2013a) and Chen et al. (2013a) preliminary designed both wavy-channel and offset strip-fin PCHEs for VHTR applications. Ma et al. (2015) performed a thermal-hydraulic performance study of zigzag-channel PCHEs with helium as the working fluid. The authors found that the flow and temperature in zigzag channels can't achieve a fully-developed flow at high-temperature conditions due to significant variations of the helium thermophysical properties associated with the large temperature change along the fluid flow directions. However, a steady condition was observed in low-temperature operating conditions. The local Nusselt number and friction factor at high temperatures agreed well with those at low temperatures when the Reynolds numbers were greater than 900. In addition, based on the numerical simulations, the authors suggested to use a larger inclination angle on the cold side when utilizing hybrid channels.

Aneesh et al. (2106) also carried out a numerical study on straight-channel PCHEs with helium as the working fluid and Alloy 617 as the heat exchanger structural material. The authors investigated the effects of heat exchanger operating conditions, fluid thermophysical properties, plate arrangements (i.e., single or double banking), and hemispherical dimples inside the channels. Khan et al. (2016) conducted three-dimensional steady-state conjugate heat transfer simulations to study zigzag-channel PCHEs with various incline angles and presented detailed PCHE thermal-hydraulic characteristics. Flow enhancement and secondary flow regimes were found in zigzag channels. Flow enhancement could increase heat transfer while the secondary flow due to flow

separation and vortex formation would affect heat transfer augmentation. In addition, the authors demonstrated better thermal-hydraulic performance for zigzag-channel PCHEs as compared to straight-channel PCHEs. Despite their work on PCHEs using helium as a working fluid, no experimental testing had been performed in typical VHTR operating conditions. Chen et al. (2016a) presented the fabrication procedure of a counter-flow PCHE with zigzag channels that could be used in high-temperature and high-pressure conditions and performed a thermal-hydraulic investigation of the fabricated PCHE at high temperatures.

Yoon et al. (2017) conducted a comprehensive numerical study of the friction factor and heat transfer for zigzag-channel PCHEs of various geometrical parameters. General explicit correlations were developed for both the friction factor and Nusselt number as a function of geometrical parameters, Reynolds and Prandtl numbers based on STAR-CCM+ computational results. The correlations are applicable to a wide of flow channel geometries in laminar flow regime. The study indicated that the friction factor for zigzag channels in PCHEs was mainly influenced by zigzag channel geometry while the Nusselt number was influenced by the overall heat exchanger design, including the plenum sections. As sCO_2 Brayton cycle becomes more attractive thanks to the development of high-temperature materials and compact heat exchangers, more and more studies on compact mini-channel heat exchangers have been performed (Baik et al., 2017; Kim et al., 2017; and Meshram et al., 2016).

1.2.2 On optimization of geometrical parameters

Due to one unique fabrication technique (i.e., photochemical machining) used for PCHEs, various mini-channel shapes and geometries could be realized. It is important to optimize the channel geometry for PCHEs because the shape of heat transfer surfaces could affect their thermal-hydraulic performance, as well as their mechanical integrity. The optimization of geometrical parameters for PCHEs could stem from a study on PCHE cost analysis (Gezelius, 2004). The author analyzed the cost of PCHEs by calculating the ratio of the blower power to the total heat exchanger duty, which was a simplified way to highlight dependencies among the most important geometrical parameters. This study assumed that PCHEs consisted only of straight flow channels. Kim et al. (2008) also carried out a cost analysis and optimization study of PCHEs for VHTR applications. The authors designed a PCHE for a 600-MW_{th} VHTR, which was optimized based on analysis of its capital and operational costs. Several factors, such as heat exchanger geometrical parameters, reactor thermal duty, lifetime, and working fluids, were included in the optimum sizing model. However, the result may not be the real optimized point, but it is still useful for providing a cost-effective method for PCHE optimization for a given VHTR.

More complex models, such as multi-objective optimization and genetic algorithms, have been used for PCHE optimization studies. Lee and Kim (2012) conducted an optimization study of zigzag flow channels of a PCHE for nuclear power plant application. A multi-objective genetic algorithm was used with two non-dimensional objective functions in terms of heat transfer and friction loss. Five optimal designs on the Pareto-optimal front were selected and compared using objective functions. In a later study, Lee et al. (2013) performed a multi-objective optimization of a double-faced type PCHE with zigzag channels. In addition, an exergy analysis was carried out and the results showed that the designs located at the opposite extremes of the Pareto-optimal front

had an energy saving advantage over the reference design. For zigzag channels, the influences of the pitch lengths, diameters, and zigzag angles on the Nusselt number and friction factor were not independent but interacted with each other. Bartel et al. (2015) performed a comparative study of PCHE designs for a typical VHTR design and concluded that the zigzag-channel PCHE with an inclination angle of 15º provided the best performance in heat transfer while incurring a moderate pressure drop penalty as compared to the straight-channel PCHEs. Wang et al. (2017) investigated heat transfer and fluid flow behaviors in zigzag channels and analyzed the effect of the geometrical parameters of zigzag channels on thermal-hydraulic performance. A combination of computational fluid dynamics (CFD), artificial neural network (ANN), and Non-Dominated Sorting Genetic Algorithm (NSGA-II) methods were applied to optimize the geometrical parameters of zigzag channels. This method considerably shortened the time needed for optimization. A set of multi-objective optimal geometrical parameters were obtained, from which engineers could select the best design points based on their considerations. In addition to optimization of zigzag-channel PCHEs, a number of studies were conducted for other channel shapes, such as airfoil fin and S-shaped fin types (Xu et al., 2014; Zhang et al., 2016; and Kwon et al., 2017).

1.2.3 On stress analysis and mechanical integrity

As noted, IHX-type PCHEs are anticipated to operate at high temperatures with pressure drops, so the determination of thermal stresses is critical in predicting of the lifetime of a PCHE. Although the ASME code Section VIII qualifies the use of zigzag-channel PCHEs, no detailed heat exchanger design procedures for high-temperature, high-pressure nuclear service are provided in the code. A detailed background and description on the state-of-the-art PCHE designs for

mechanical integrity have been reported by Nestell and Sham (2015) along with some studies on structural assessment, including both experimental and numerical research.

Pra et al. (2007) carried out an experimental transient test on a mock-up PCHE to study its thermomechanical behavior and they concluded that the PCHE recuperator could meet the requirements for use in high-temperature gas-cooled reactors. Oh and Kim (2008) performed a stress analysis for a Heatric's PCHE using an ABAQUS two-dimensional model and investigated several heat exchanger stress behavior effects. They found that the lifetime of a PCHE-type IHX was approximately 35 years at an operating temperature of 900 °C and the off-set channel configuration design reduced stress concentration by a maximum of 50%, which could lead to a significant increase in PCHE lifetime. This study also concluded that a three-dimensional stress analysis was required to produce more accurate results. Song (2011) conducted a structural behavior analysis of a small-scale PCHE prototype under high-temperature conditions. It was found that the greatest amount of stress occurred at both the inlet and outlet chambers. Local stress near the channels, however, was not presented in the paper. Lee and Lee (2014) assessed the structural integrity of zigzag-channel PCHEs for sodium-cooled fast reactor (SFR) applications. They found that PCHEs made of Stainless Steel 316 were anticipated to have mechanical integrity in compliance with ASME standards because the plasticity sufficiently reduced local stress concentration at channel tips. The temperatures used in the analysis were for SFRs, so the conclusion could not be applied to PCHEs for VHTR applications. Significant effort on performing stress analyses of PCHE mechanical integrity will be necessary in the near future.

1.2.4 On transient performance

Understanding dynamic behavior is of importance in the design of PCHE-type IHXs for use in advanced nuclear power plants since some transients may lead to accidents and the dynamic response of the IHXs would play an essential role in accident progression. Any transient in the power conversion systems or process heat plants will propagate back to the reactor's primary coolant system via the PCHE. It is therefore critical to understand how the PCHE would dynamically respond to transients and a dynamic response analysis of the PCHE becomes imperative. Although many studies on the steady-state thermal-hydraulic performance of PCHEs have been conducted, limited research on transient analyses of PCHEs, both numerical and experimental, has been conducted. In literature, the only available experimental transient test of a mock-up PCHE was carried out by Pra et al. (2007). Several transient cycles were performed to study the thermomechanical behavior of the PCHE, although no dynamic model was proposed, and the temperature transients were not analyzed in their study. Carstens (2007) derived a series of equations to solve a PCHE for transients in an sCO_2 power cycle. A quick solution could be obtained for both the steady states and transients of the PCHE, however, the method could not accurately calculate PCHE performance. Ravindran et al. (2010) designed a straight-channel PCHE for the NGNP and conducted a loss of coolant accident (LOCA) simulation for the plant using RELAP5-3D. To simplify, the semicircular channels of the PCHE were mapped into rectangular geometries, which would lead to some distortions even in the steady-state calculations. Bartel et al. (2013b) made an attempt to model transient behavior of wavy-channel PCHEs. However, no results were reported in their paper. Chen et al. (2015b) analyzed the dynamic response of an offset-strip-fin plate-type heat exchanger used as a secondary heat exchanger (SHX)

in a fluoride-salt-cooled high-temperature test reactor (FHTR). The adopted model was verified using a commercial software "DYNSIM" while no experimental data were available to validate the dynamic model. In a later study, Chen et al. (2016b) performed both experiments and numerical simulations for a straight-channel PCHE utilizing the same numerical model. The dynamic model was successful in predicting the steady-state and transient behaviors of the straight-channel PCHE. Nonetheless, no transient simulation or experiment was carried out for the zigzag-channel PCHE.

Although literature on PCHE transient analyses is sparse, a number of dynamic studies have been performed on plate-type heat exchangers for both steady-state and transient conditions. Since PCHEs are plate-type heat exchangers, the dynamic models developed for plate-type heat exchangers could be applied to PCHEs. Pingaud et al. (1989) performed steady-state and transient simulations of a plate-fin heat exchanger. A dynamic model was developed based on the mass, momentum, and energy balances to simulate the heat exchanger's performance and mechanical integrity under severe perturbations. However, the model was too complicated to be adopted for other heat exchangers. Lakshmanan and Potter (1990) developed a numerical model, named as "cinematic" model, based on energy balance by assuming there was no heat capacitance in solid plates and the fluid flow was plug flow. The "cinematic" model offered a convenient and fast method to simulate the steady-state and transient behaviors of plate-type heat exchangers. Sharifi et al. (1995) proposed a general dynamic model based on the "cinematic" model that could be applied to plate-type heat exchangers with different geometrical dimensions. Experiments were conducted to assess the applicability of the dynamic model and the numerical solutions and experimental data were found in good agreement. Roetzel and Xuan (1999) summarized mathematical models for the analytical and numerical treatment of transient processes in a variety

of heat exchangers, such as plate-type heat exchangers, shell-and-tube heat exchangers, and double-pipe heat exchangers. They solved the differential equations using the numerical inversion of the Laplace and Fourier transforms, providing a simple approach to analyze the dynamic behavior of heat exchangers. However, the method could not be applied with ease to a large system with multiple heat exchangers coupled together. A simple method used earlier could be adopted for PCHE transient analyses.

1.3 Research Objectives

Although many studies have been performed on PCHEs, no experiment prior to this study has been conducted on the thermal-hydraulic performance of zigzag-channel PCHEs under VHTRs' typical operating conditions with the heat exchanger hot-side helium inlet temperature at 800 °C or above, to the author's best of knowledge. Most studies in the literature used PCHEs acquired from a commercial vendor and there could be non-trivial uncertainties in the geometrical parameters of the heat exchangers, which will propagate to uncertainties associated with any correlations developed based on the experimental data. Also, the local thermal-hydraulic performance of zigzag-channel PCHEs has not been thoroughly investigated, as there are still many unknowns regarding different ways affecting its performance. Limited studies on the thermal boundary conditions of zigzag-channel PCHEs are available. As noted, the dynamic behavior of PCHE-type IHXs is of importance for advanced nuclear reactors. However, research on the dynamic performance of PCHEs is scarce.

To address these issues, the principal objectives of the current research are to investigate, both experimentally and numerically, the pressure drop and heat transfer characteristics of high-temperature PCHEs for use in advanced nuclear reactors and to model both the steady-state and dynamic behaviors of zigzag PCHEs using the developed heat exchanger models. The specific objectives of the current research are outlined as follows:

(1) To design and fabricate a reduced-scale high-temperature PCHE with zigzag channels;
(2) To experimentally test the fabricated PCHE under typical VHTR operating conditions;
(3) To develop heat transfer and pressure drop correlations based on the obtained experimental data;
(4) To numerically model both the steady-state and dynamic performance of the fabricated heat exchanger; and
(5) To study the application of PCHEs in an advanced nuclear reactor (i.e., FHTR).

1.4 Dissertation Organization

During this research period, a number of papers (Chen et al., 2013a; Chen et al., 2013b; Chen, 2015a; Chen et al., 2015b; Chen et al., 2015c; Chen et al., 2016a; Chen et al., 2016b; Chen et al., 2018a; and Chen et al., 2018b) were published. Most of the relevant content will be covered in this dissertation that consists of seven chapters. A summary for each chapter is presented as follows:

Chapter 1 briefly introduces the background of this dissertation, reviews related literature on PCHEs, and outlines the objectives for the current research.

Chapter 2 introduces the fundamentals of heat exchanger thermal design. The developed one-dimensional code for heat exchanger thermal design is described in detail. A comparison between the results obtained from the one-dimensional code and the conventional LMTD method is carried out for both the IHX-type and reduced-scaled PCHE designs. Fabrication techniques and fabrication aspects of the zigzag-channel PCHE are briefly discussed.

Chapter 3 supplies brief information regarding the high-temperature helium test facility and presents the experimental data reduction methodology. The pressure drop and heat transfer characteristics of the fabricated zigzag-channel PCHE are presented. A method for developing new pressure drop and heat transfer correlations based on the obtained experimental data is illustrated. The heat loss analysis of the fabricated PCHE is also introduced.

Chapter 4 covers the numerical study of the fabricated zigzag-channel PCHE. Local and global thermal-hydraulic characteristics of the simulated PCHE are presented with the various effects on its performance. A numerical investigation of the simulated PCHE's thermal boundary conditions is also carried out. In addition, PCHE channel geometry optimization using a multi-objective optimization method is provided. Finally, the stress field of a simplified 3-D geometry is numerically obtained.

Chapter 5 presents numerical models to simulate the dynamic performance of both the straight-channel and zigzag-channel PCHEs. The obtained numerical results are compared with the data obtained from experiments to demonstrate feasibility of the dynamic model.

Chapter 6 introduces a case study for the dynamic modeling of a PCHE with offset-strip fins coupled with an FHTR. Analyses of three transient scenarios are presented.

Chapter 7 summarizes the results and major conclusions for the present research and provides some recommendations for future work.

Chapter 2 PCHE Design and Fabrication

2.1 Overview

This chapter briefly introduces the fundamentals of heat exchanger thermal design and rating. One-dimensional code for heat exchanger design is developed and described in detail. A comparison between the one-dimensional code method and conventional LMTD method is carried out for both the IHX-type and reduced-scaled PCHE designs. Finally, fabrication techniques and fabrication aspects of the reduced-scale PCHE with zigzag channels are described.

2.2 Heat Exchanger Thermal Design

The thermal design of a heat exchanger is generally referred to as heat exchanger sizing, while the performance evaluation of an existing heat exchanger is referred to as heat exchanger rating. In the heat exchanger rating process, the heat transfer and pressure drop performance, as well as the effectiveness and fluid outlet temperatures, of a heat exchanger are determined. Sizing is the heat exchanger thermal-hydraulic design process and involves the quantitative evaluation of the heat transfer and pressure drop as well as the heat exchanger's physical dimensions. In this process, the heat exchanger's construction type, material, flow arrangement, and physical size are determined. One could convert a heat exchanger sizing process to a heat exchanger rating process by iteratively specifying the dimensions until the heat transfer performance and pressure drop meet the

requirements. The PCHE thermal design in the current research is considered to be heat exchanger sizing.

A PCHE is a diffusion-bonded compact heat exchanger with a variety of channel shape options, including straight, zigzag (wavy), offset-strip fins, and airfoil fins. The PCHE design or sizing is a trial-and-error process based upon (1) design conditions, i.e., fluid inlet and outlet temperatures and flow rates; (2) heat transfer surface area and overall heat transfer coefficient; (3) pressure drops across both sides of the PCHE; and (4) fabrication capabilities. Although a reasonable heat exchanger design can be obtained from the sizing process, other factors, such as the capital cost and operational cost of the heat exchanger, need to be considered when finalizing its design. Following Chen (2015a), Hesselgreaves (2001), Shah and Sekulic (2003), and Thulukkanam (2013), the basic heat exchanger performance variables involved in the heat exchanger thermal design are summarized as follows.

During the heat exchanger's steady-state operation, the rate equations for both the hot and cold sides are,

$$\dot{Q}_h = \dot{m}_h c_{p,h} \left(T_{h,i} - T_{h,o} \right) \tag{2.1}$$

and

$$\dot{Q}_c = \dot{m}_c c_{p,c} \left(T_{c,o} - T_{c,i} \right) \tag{2.2}$$

where T represents the mean fluid temperature; subscripts h and c refer to the hot and cold fluids; and subscripts i and o designate the inlet and outlet of the fluids. The heat load of the hot and cold sides includes: the (a) heat exchange between the hot side and cold sides and (b) heat loss

from the heat exchanger surface to its surroundings. The total heat loss from the heat exchanger is represented as,

$$\dot{Q}_{loss} = \dot{Q}_h - \dot{Q}_c . \tag{2.3}$$

The heat capacity rate, $\dot{m}c_p$, is denoted as C for convenience. The maximum and minimum of the two streams are $C_{\max}$ and $C_{\min}$. Therefore, the maximum possible heat exchanged between the streams, $\dot{Q}_{\max}$, is given by,

$$\dot{Q}_{\max} = C_{\min}\left(T_{h,i} - T_{c,i}\right). \tag{2.4}$$

Equation (2.4) represents the heat transfer capability of a heat exchanger with an infinite surface area. The heat exchanger effectiveness, ε, can be given as,

$$\varepsilon = \frac{C_h\left(T_{h,i} - T_{h,o}\right)}{C_{\min}\left(T_{h,i} - T_{c,i}\right)} \text{ or } \varepsilon = \frac{C_c\left(T_{c,o} - T_{c,i}\right)}{C_{\min}\left(T_{h,i} - T_{c,i}\right)}, \tag{2.5}$$

where the effectiveness of the exchanger can be obtained directly from the heat capacity rates and terminal temperatures, which are given in the heat exchanger sizing process. C_h and C_c are the hot and cold sides' heat capacity rates, respectively, one of which will be $C_{\min}$ unless the exchanger is balanced. In a two-stream heat exchanger, the stream with a larger temperature change is called the "weak" stream, having the lower thermal capacity rate of $C_{\min}$. The stream with the smaller temperature change is said to be the "strong" stream, which has the higher thermal capacity rate of $C_{\max}$.

For a countercurrent flow arrangement, the maximum driving force for the heat transfer between the two fluids is the LMTD. The heat transfer rate equation is given by,

$$\dot{Q} = UA\Delta T_{lm}, \tag{2.6}$$

where the log-mean temperature difference, ΔT_{lm}, is defined as,

$$\Delta T_{lm} = \frac{\Delta T_1 - \Delta T_2}{\ln\left(\frac{\Delta T_1}{\Delta T_2}\right)}, \tag{2.7}$$

where ΔT_1 and ΔT_2 are the terminal temperature differences regardless of heat exchanger configuration. Some limiting values of ΔT_{lm} are,

$$\Delta T_{lm} = \begin{cases} \dfrac{\Delta T_1 + \Delta T_2}{2} & \left(\Delta T_1 \to \Delta T_2\right) \\ \Delta T_1 = \Delta T_2 & \left(\Delta T_1 = \Delta T_2\right) \end{cases}. \tag{2.8}$$

UA is the product of the overall heat transfer coefficient, U, and the total hot- or cold-side heat transfer area, A, which is referred to as heat transfer conductance. The overall heat transfer coefficient U combines the convective and conductive mechanisms responsible for the heat transfer from the hot-side fluid to the wall and from the wall to the cold-side fluid. The inverse of the heat transfer conductance UA is referred to as the overall heat transfer resistance. Overall thermal resistance is expressed by,

$$\frac{1}{UA} = \frac{1}{A_h h_h} + \frac{t_w}{A_w k_w} + \frac{1}{A_c h_c}, \tag{2.9}$$

where A_h, A_c, and A_w are the heat transfer areas of the hot side, cold side, and wall of the heat exchanger, respectively; h_h and h_c denote the hot-side and cold-side heat transfer coefficients, respectively; t_w denotes wall thickness; and k_w is the thermal conductivity of the wall material.

The fouling resistance is neglected in the current study. In addition, the wall resistance could be neglected for a thin wall with a large thermal conductivity value.

The ratio of overall thermal conductance to the smaller heat capacity rate is referred to as the Number of Transfer Unit (NTU), which designates the non-dimensional heat transfer size or thermal size of the heat exchanger. NTU can be expressed as,

$$\mathrm{NTU} = \frac{UA}{C_{\min}} = \frac{1}{C_{\min}} \int_A U \mathrm{d}A \,. \tag{2.10}$$

NTU provides a measurement of a heat exchanger's size, even though it does not necessarily represent the physical size of a heat exchanger due to two other factors: U and $C_{\min}$. As the NTU value increases, the exchanger's effectiveness generally increases as well. A higher NTU can be obtained by increasing either U, A, both, or by decreasing $C_{\min}$.

For the heat exchanger, the basic design assumptions are: (1) the working fluid flow rates in the primary and secondary loops are equivalent and thus it is a balanced-flow heat exchanger; (2) the heat exchanger operates at steady state; (3) flow distribution in each channel is uniform; (4) the hot and cold plates have identical geometry; (5) the cross section of the flow passage is approximately semicircular for zigzag-channel PCHEs; (6) heat conduction in the plate and fluid along the flow direction is neglected; and (7) heat loss from the exchanger surface to the surroundings is neglected. A general flowchart of the conventional LMTD method for heat exchanger thermal design is shown in Figure 2-1.

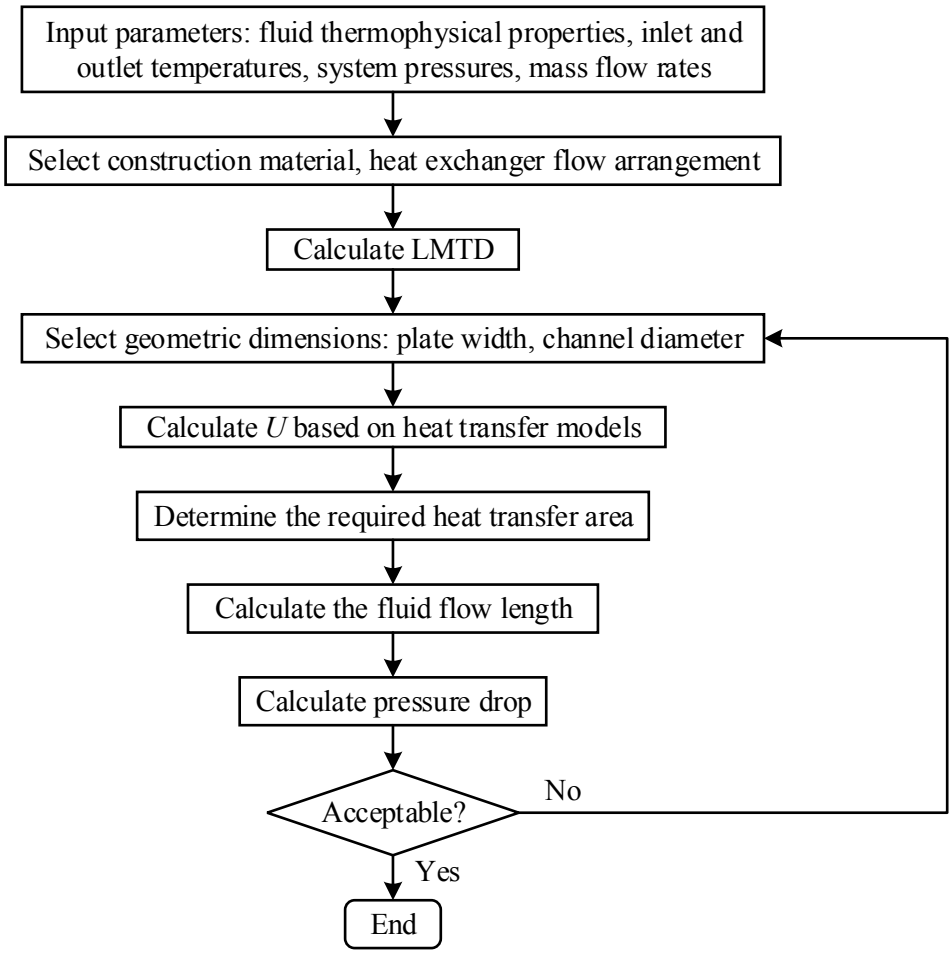

Figure 2-1. General flowchart of conventional LMTD method for heat exchanger thermal design.

2.3 One-Dimensional Design Code

Fluid properties affect heat transfer and pressure drop in heat exchangers. Simply using the log-mean temperature difference method or applying energy balance across the entire heat exchanger is not valid for heat exchanger thermal design when the fluid properties change significantly along the heat exchanger's flow path. In addition, the non-linear change of local heat transfer coefficients leads to a non-uniform overall heat transfer coefficient, which could substantially deviate the energy balance. This could be solved by dividing a heat exchanger into multiple axial segments

and then applying energy balance and the LMTD method to each segment. One-dimensional design code can be utilized for the thermal design since the fluid properties do not vary dramatically, which is attributed to the small fluid temperature variances across a small heat exchanger segment. The heat exchanger is modeled in one dimension with three parallel channels as shown in Figure 2-2. The top and bottom channels are the hot-side and cold-side fluid streams, respectively, and the second channel represents the solid wall for separating hot and cold fluid streams. The following are the assumptions made when developing the one-dimensional code for heat exchanger thermal design:

1. The heat exchanger operates in steady state;
2. The flow distribution into each channel on each side is uniform;
3. The hot and cold plates have identical geometry;
4. The cross-sectional shape of the flow passage is approximately semicircular;
5. The fluid and solid thermophysical properties are considered to be constant in a small heat exchanger segment;
6. Heat conduction in the plate and fluid along the fluid flow directions on both sides is neglected; and
7. Heat loss from the exchanger surface to the surroundings is neglected.

Based on assumptions 2 to 6, the multi-channel heat exchangers can be modeled into three channels. Below is a step-by-step procedure for developing the one-dimensional code for heat exchanger thermal design.

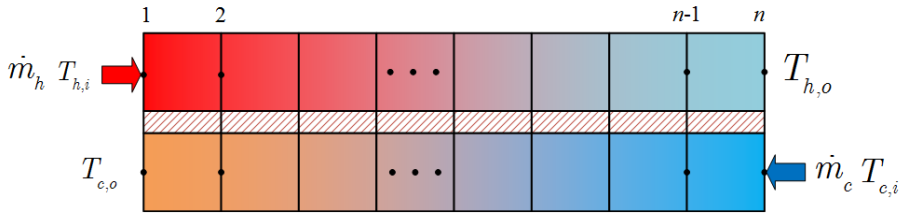

Figure 2-2. Nodal structure for one-dimensional design code.

1. Divide the heat exchanger into a number of segments based on the prescribed temperature spacing on the hot side of the heat exchanger.
2. For the first heat exchanger segment, determine the temperature at location 2 on the cold side using Equations (2.1) and (2.2).
3. Compute the fluid mean temperature and the fluid thermophysical properties on each fluid side in the first heat exchanger segment. With these mean temperatures, determine c_p, μ, k, Pr, and ρ on each fluid side.
4. Calculate Reynolds number, Re, and determine f and Nu on each fluid side from the given design data for each surface and the thermal-hydraulic correlations.
5. Compute the convective heat transfer coefficient, h, on each side and the overall heat transfer coefficient, U.
6. Calculate the length for the first heat exchanger segment.
7. Compute the pressure drop on each fluid side.
8. Repeat steps 2 to 7 for the remaining heat exchanger segments.
9. Sum all lengths for all segments to get the total required length of the heat exchanger. Sum all pressure drops to get the total pressure drop on each fluid side.
10. If the total pressure drops on both sides are within input specifications, the solution to the heat exchanger sizing is completed; modify the front free flow area by changing the number

of channels if the evaluated total pressure drop on either side exceeds the setting limit, which is typically 1% of the system pressure. Finer alterations, such as using the same number of flow channels for all plates, may be conducted during this procedure.

2.4 Thermal-Hydraulic Model

The heat transfer and pressure drop characteristics play an important role in PCHE sizing or the thermal design process. Many experimental and numerical studies have been conducted to develop thermal-hydraulic models for designing PCHEs. Printed circuit heat exchangers typically operate at a low Reynolds number regime for VHTR applications because large operational costs would be incurred should the PCHE be operated at a high Reynolds number regime. The helium flow in the small channels would need a tremendous amount of pumping power. As noted, the current study centers on a zigzag-channel PCHE design with a semicircular flow channel cross section. Models used for heat transfer and pressure drop calculations are given as follows:

Fanning friction factor:

$$f \cdot \mathrm{Re} = 15.78 + 0.6677\,\mathrm{Re}^{0.81258} \tag{2.11}$$

Heat transfer coefficient:

$$\mathrm{Nu} = 4.089 + 0.0083\,\mathrm{Re}^{0.86054} \tag{2.12}$$

Equations (2.11) and (2.12) were developed for the flow and heat transfer in semicircular flow channels. f and Nu denote the Fanning friction factor and Nusselt number, respectively. Figure

2-3 displaces the cross section of four PCHE channels, where t_p is the plate thickness, d is the flow channel diameter, P is the channel pitch, and t_e is the equivalent thickness of the plate.

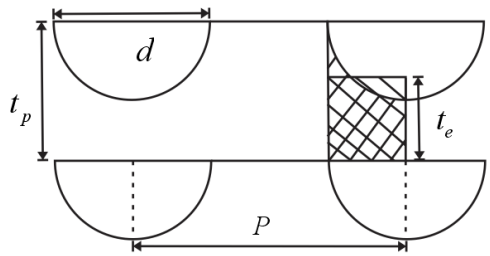

Figure 2-3. Schematic of cross section for four channels.

When considering thermal resistance due to heat conduction in the PCHE plates, an equivalent thickness t_e for all the plates was used (Kim, 2012):

$$t_e = t_p - \frac{\pi}{8} d, \tag{2.13}$$

where t_p is the plate thickness and d is the channel diameter.

2.5 Thermal Design Results and Comparisons

PCHE operating conditions were obtained from a referenced VHTR design (Bartel et al., 2015). The thermal duty of the PCHE was 600 MW. Helium was used for both the hot and cold sides. The construction material for the heat exchanger core was Alloy 617. The selected inlet pressures on the hot side and the cold side were 7.0 and 7.97 MPa, respectively. Due to fabrication capability constraints, the maximum plate width was set as 0.6 m and the maximum plate length in the flow direction was set as 1.5 m. The pressure drops on both the hot and cold sides were assumed not to exceed 1% of the inlet pressure of the fluids. The PCHE was designed under the nominal operation

condition using both classic LMTD method and the one-dimensional code, and key parameters are listed in Table 2-1. Note that the design parameters were not necessary optimized, rather they were based on current reasonable manufacturing capabilities (i.e., photochemical etching and diffusion bonding).

The volume of a prototypic zigzag-channel PCHE as an IHX for a 600 MW_{th} reactor is greater than 25 m^3. It is important to understand the PCHE's thermal-hydraulic performance shown in experiments. However, performing experiments using such a large-sized heat exchanger prototype is extremely expensive and time consuming. To obtain the IHX's thermal-hydraulic performance and verify its function for advanced nuclear reactor applications, a scaled-down approach, i.e., reducing the volume of the test PCHE while maintaining similar performance to the prototype, was adopted for this design (Chen, 2015a).

For this study, the main purpose of scaling down the zigzag-channel PCHE was to ensure the flow and heat transfer mechanisms of the PCHE to be tested were similar to those of the prototypical PCHE. In other words, the operating Reynolds number of the test PCHE must be similar to that of the prototype, given that the channel geometry of both the prototype and test model were the same. The channel Reynolds number can be obtained from the energy balance equations as:

$$\dot{Q} = \dot{m} c_p \Delta T \tag{2.14}$$

$$\dot{Q} = UA\Delta T_{lm} \tag{2.15}$$

From Equations (2.14) and (2.15), the Reynolds number ratio of the test model to the prototypic PCHE can be expressed as,

$$\left(\mathrm{Re}\right)_R = \left(\frac{\rho v d_h}{\mu}\right)_R = \left(\dot{m}\right)_R = \left[\frac{\left(0.5\pi d + d\right) L \Delta T_{lm}}{\Delta T}\right]_R = \left(\frac{L \Delta T_{lm}}{\Delta T}\right)_R . \quad (2.16)$$

To preserve the heat transfer and pressure drop characteristics of the test model and prototypical heat exchanger, the Reynolds number ratio should be equal to one. From Equation (2.16), only by adjusting ΔT_{lm} and ΔT can the Reynolds number ratio for the test model and the prototype be kept at that value because the flow length of the test model should be much smaller than the length of the prototype. Another key purpose of this study was to determine the performance of the PCHE in high-temperature conditions. Therefore, the hot-side helium inlet temperature was maintained at 800 °C for the scaled-down PCHE. The flow length was chosen to be approximately 0.2 m due to the size limitation of the test facility.

One reasonable test unit was obtained. Table 2-1 shows the comparisons between the test unit and the prototypical parameters when the Reynolds numbers on the hot sides were the same for both the scaled-down test unit and the prototypical PCHE. With the same input parameters, the LMTD method underestimated the pressure drop while it overestimated the heat transfer when compared with the values obtained from the one-dimensional design code. The main reason for this was that the fluid thermophysical properties changed dramatically along the fluid flow direction, which led to a non-uniform overall heat transfer coefficient. Compared to the 1-D code method, the obtained heat exchanger lengths from the LMTD method were underestimated by about 3.7 and 8.7% for the prototypical design and test unit design, respectively. It should be noted that the heat transfer coefficient and Fanning friction factor were estimated using Kim's correlations (Kim, 2012), which were based on the LMTD method. In the current study, the geometrical parameters selected

for the test unit were based on the LMTD method. Both the one-dimensional code and LMTD method for zigzag-channel PCHE thermal designs were attached in the Appendix.

Table 2-1. Comparison between test model and prototype.

Parameters	Units	Prototype		Test unit	
		LMTD method	1-D code	LMTD method	1-D code
Thermal duty	kW	600,000		13	
Hot-side fluid inlet temperature	°C	800		800	
Cold-side fluid inlet temperature	°C	520		350	
Hot-side fluid outlet temperature	°C	543		462	
Cold-side fluid outlet temperature	°C	776		688	
LMTD	°C	23		112	
Hot-side inlet pressure	MPa	7.0		2.0	
Cold-side inlet pressure	MPa	7.97		2.0	
Hot-side mass flow rate	kg/s	449.57	449.88	7.35×10^{-3}	
Cold-side mass flow rate	kg/s	451.33	451.68	7.35×10^{-3}	
Total number of plates	–	8440		16	
Flow length	m	0.78	0.81	0.21	0.23
Hot-side Reynolds number	–	1,753	1,512	1,753	1,521
Cold-side Reynolds number	–	1,789	1,538	1,915	1,673
Hot-side Nusselt number	–	9.2	8.6	9.2	8.6
Cold-side Nusselt number	–	9.3	8.7	9.6	9.0
Overall heat transfer coefficient	$W/(m^2\text{-}°C)$	1,214	1,173	1,206	1,108
Hot-side pressure drop	kPa	28.5	30.3	23.3	27.0
Cold-side pressure drop	kPa	24.6	26.2	19.6	22.6

2.6 Fabrication Techniques for the Zigzag-Channel PCHE

To reiterate, a PCHE is one of the promising IHX candidates for VHTRs because of its high compactness and strong robustness. PCHE fabrication techniques should be seriously considered because PCHEs will be used in severe environments for long periods of time. A brief introduction to fabrication processes and techniques of the scaled-down zigzag-channel PCHE, and its detailed design aspects are presented below.

2.6.1 Photochemical machining

Photochemical machining (PCM) is a process that employs chemical etchants through photoresist to remove the selected area on the working material. It is used to produce a variety of precision patterns in a flat piece of metal. Figure 2-4 shows the stages of the PCM process.

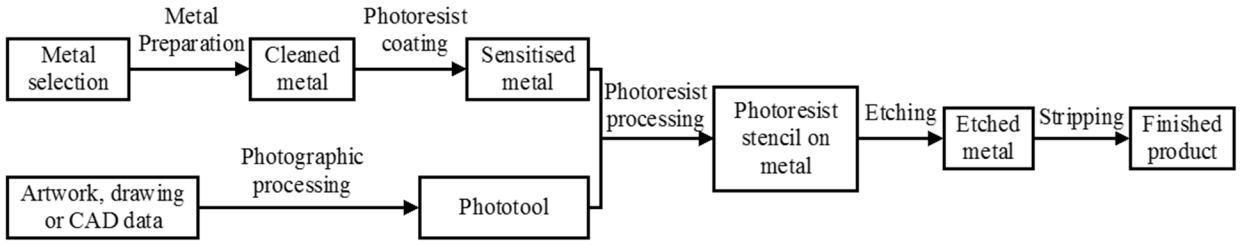

Figure 2-4. Stages of photochemical machining procedures (Allen, 2004).

The working material is required to be thoroughly cleaned so that the photo-resistant coating can adhere to its surface. A phototool, consisting of transparent and opaque regions created by computer-aided design (CAD), is then transferred to the coated metal by activating the polymer within the photoresist. A certain amount of ultraviolet (UV) light is applied to the metal to develop

the selected areas, which are then etched by spraying etchant on the metal surface. Finally, the remaining resistant on the metal surface is stripped and the sheets or parts are cleaned and dried for further processing. This photochemical machining technique was verified for etching Alloy 617 metal by Mylavarapu (2011). It required a strong corrosive etchant because of the large chromium and nickel content present in Alloy 617.

A surface examination of the etched plates was conducted to determine channel surface roughness. The roughness on the internal flow channel imparted by the chemical etching process could lead to a variation in the local hydraulic diameter, resulting in an increased heat transfer coefficient as well as friction factor. If the roughness is small enough compared to the channel diameter, the roughness effects can be neglected for laminar flow (Mylavarapu, 2011). Since the PCHE operates in the laminar and laminar-to-turbulent flow transition regions, it is valuable to know the channel roughness. In addition, the plate's surface roughness affects the quality of diffusion bonding. Therefore, it is of great importance to measure the roughness of both the channel surface and plate surface.

Both the channel roughness and plate surface roughness were measured using the Veeco-Wyko NT9100 surface profiler. The Veeco-Wyko NT9100 optical profiler performs non-contact, 3-D surface measurements using vertical scanning interferometry (VSI) for a wide variety of topologies, as well as phase-shift interferometry (PSI) for more subtle profile changes (Operation Manual, 2007). The VSI mode used for measuring the channel surface roughness and image processing was completed using the built-in software package. Three measurements were carried out at three random locations on the channel surface. Figure 2-5 shows a 3-D image of the surface

characteristics of a representative channel interior surface. The measured region is 312 μm × 234 μm.

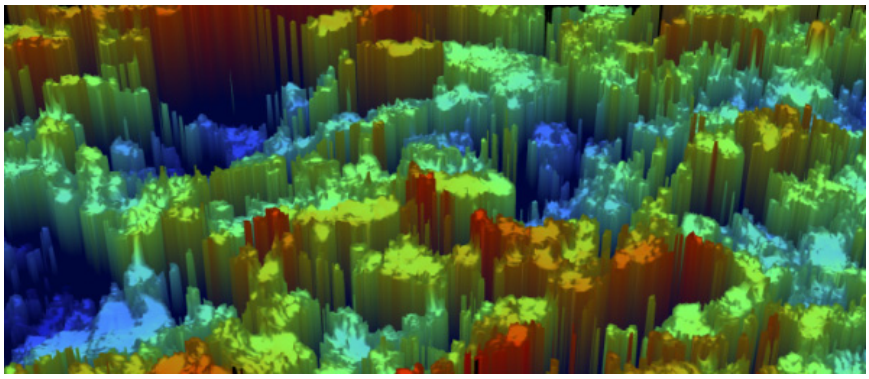

Figure 2-5. 3-D image of representative channel interior surface.

There are three roughness parameters in use here, namely, R_a, R_q, and R_t. R_a is the arithmetic average roughness of absolute values; R_q is the root mean squared roughness; and R_t is the maximum height of the profile. The measured data are listed in Table 2-2.

Table 2-2. Surface roughness of zigzag channels.

Data type	Unit	Measure #1	Measure #2	Measure #3	Average
R_a	μm	3.5	3.28	2.87	3.22
R_q		4.31	4.31	3.55	4.06
R_t		27.83	35.66	32.98	32.2

The values indicated that the channel roughness was small (0.1-0.5%) compared to the channel diameter and would not influence the flow pattern. The plate surface roughness was smaller than the channel roughness and was good for diffusion bonding.

2.6.2 Diffusion bonding

Diffusion bonding is a solid-state-joining welding process by which two nominally flat surfaces are joined at an elevated temperature under a certain amount of interfacial pressure for a period (Derby et al., 1982). The applied temperature is usually in the 50 to 80% region of the absolute material's melting point. The typical procedure for diffusion bonding is: parallel the plates, clean the plates' surfaces, press the stacked plates under a certain load, and heat the stack in a vacuum environment. Atoms diffuse across the interface and form the joint between plates. As shown in Figure 2-6, the stages of diffusion bonding are: (a) the initial "point" of contact that shows a residual oxide contaminant layer, (b) yielding and creep, leading to reduced voids and a thinner contaminant layer, (c) final yielding and creep, where some voids remain with a very thin contaminant layer, (d) continued vacancy diffusion, which eliminates the oxide layer, leaving few small voids, and (e) bonding is complete (Bartle, 1979).

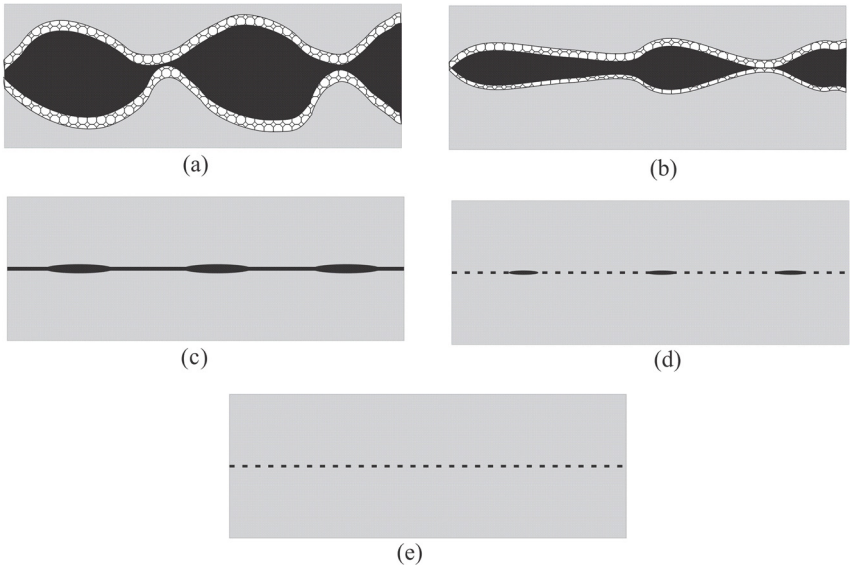

Figure 2-6. Schematic representation of diffusion bonding stages (Bartle, 1979).

Many diffusion bonding techniques are available for joining a variety of configurations and materials. Diffusion bonding is a reliable joint process with minimum distortion. To ensure the quality of diffusion bonding, several factors need to be considered. In what follows, some principal factors are briefly described.

(1) Surface preparation: Surface preparation is of significance prior to diffusion bonding. The plates must be grinded and paralleled, and the surface roughness and waviness should be controlled before bonding. Oxide and contaminants present on the surface will prevent the formation of a strong bond and should therefore be cleaned and controlled during the bonding process.

(2) Temperature and time: The applied temperature is usually in the 50 to 80% region of the absolute parent material's melting point. However, due to the increased creep resistance of high-temperature alloys, the temperature may need to be as high as 80 to 90% of the absolute parent material's melting point (Sabharwall et al., 2013). The time required to reach the desired temperature and pressure should be sufficient for two surfaces to bond. Increasing the bonding time may be necessary for material with high oxygen content to allow the interfacial oxidized films to sufficiently disperse.

(3) Pressure: Pressure or bonding load must be applied to the stack. The pressure applied in diffusion bonding is typically below the room temperature yield stress of the base metal so that no large-scale macroscopic deformation of the materials will occur.

(4) Bonding environment: Oxide film prevents the bonding process and hence leads to a low-quality bonding joint. To ensure the bonding process is protected and no oxidation film forms on the bonding surfaces, the bonding should be performed in a vacuum environment or one filled with inert gas.

Other factors, such as the material, filler material, and interlay, are important for the bonding process. Refer to the referenced study (Sabharwall et al., 2013) for detailed high-temperature heat exchanger fabrications.

2.7 Fabrication Aspects of the Zigzag-Channel PCHE

The reduced-scale zigzag-channel PCHE was fabricated using 1/16-inch (1.6-mm) thick Alloy 617 plates. A total of eight hot plates and eight cold plates were diffusion bonded together to form a metal block with 11 zigzag channels in each of these plates. Figure 2-7 shows the geometrical information for both the hot-side and cold-side plates of this PCHE. The cross section of the fluid passages is approximately semicircular with a nominal diameter of 2.0 mm and a pitch length of 2.5 mm in the span-wise (non-flow) direction. The shape of the flow passage is zigzag, and the angle between flow direction and the edge of the block is 15 degrees, as shown in Figure 2-7. This PCHE was designed in such a way that each side can withstand the maximum design pressure of 3.0 MPa for use in the HTHF.

The flow passages in each plate of the PCHE were made by applying a photochemical etching technique, which used strong chemical etchants to remove the selected area on surface of the plates.

Four 20.7-mm diameter through holes and four 6.35-mm diameter small through holes were also made on each of the 16 plates during the chemical etching process. Figure 2-8 shows an exploded view and a schematic of the fabricated PCHE. Two 12.7-mm thick plates, one on the top of the heat exchanger block and the other at the bottom, were also utilized to provide an added strength to the block. Four out of eight holes were used to direct the flow into and out of the channels. At the topmost plate, the four larger holes were connected to four headers. The other four smaller holes were used for plate alignment. Four pins were inserted into the four smaller holes before diffusion bonding to prevent the plates from sliding when adding large load on to the PCHE block to facilitate the bonding process.

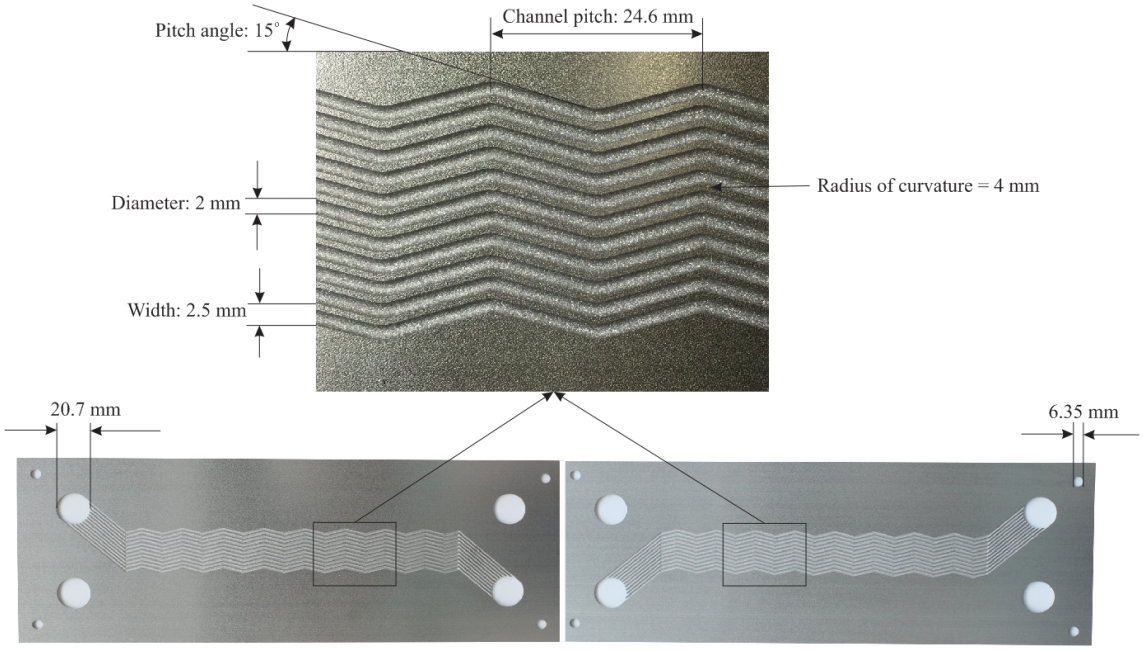

Figure 2-7. Images of one hot-side plate and one cold-side plate.

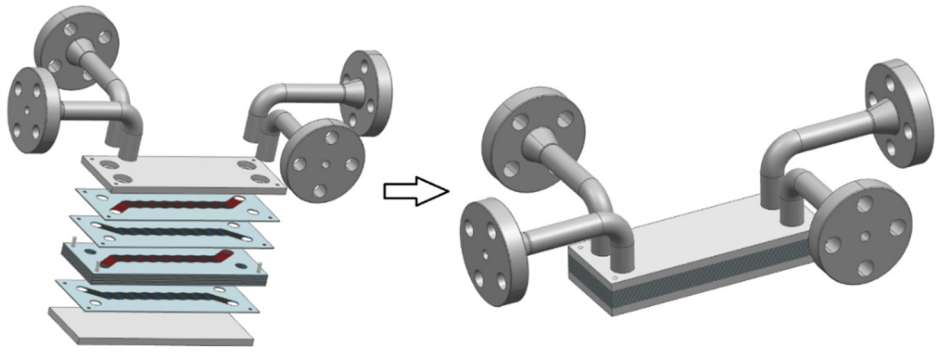

Figure 2-8. An exploded view and a schematic of the fabricated PCHE.

Once the photochemical etching process was completed, all the hot-side and cold-side plates were stacked alternately together and put into a furnace to be diffusion bonded. Before diffusion bonding, it should be prudently considered as to how to connect the four headers to the PCHE block. Two approaches were considered here: one is to perform diffusion bonding after welding the four headers on to the topmost plate, and the other is to bond the plates together while simultaneously brazing these flow distribution tubes on to the topmost plate. Figure 2-9 shows the schematic of these two approaches for joining the four headers/tubes on to the PCHE stack.

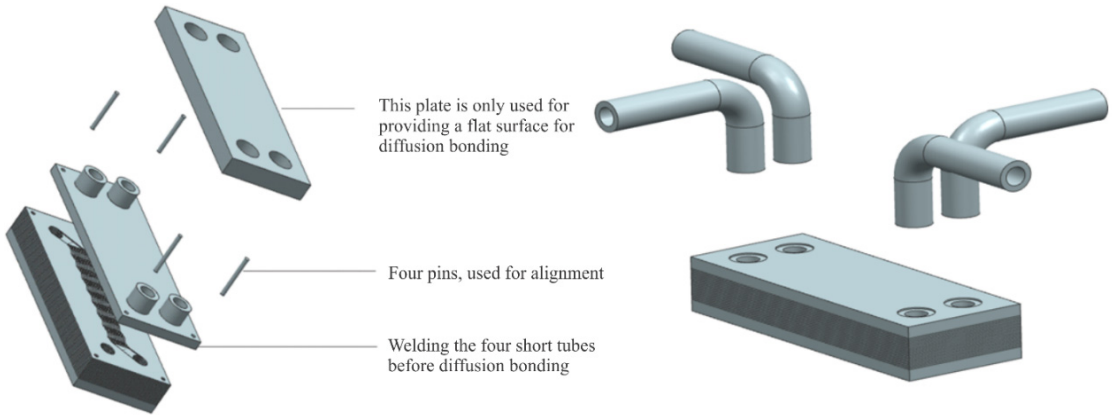

(a) Diffusion bonding after welding the four headers on to the topmost plate

(b) Diffusion bonding the plates together while brazing the tubes on to the topmost plate

Figure 2-9. Schematic of two approaches to join the four headers onto the PCHE stack.

The most common way to connect the four headers to the PCHE block is to weld these headers on to the topmost plate after all the plates are diffusion bonded. These headers could be welded on to the diffusion-bonded blocks by the Gas-Tungsten Arc Welding (GTAW) technique or other welding techniques with Alloy 617 as the filler material. In this process, damage may be caused to the PCHE bonded block due to the large thermal stress from the welding process. To reduce any potential thermal gradient and localized thermal stress, four short tubes could be welded on the topmost plate before diffusion bonding and other connecting tubes will be separately welded on these four short tubes later. The four short tubes could provide a reasonable distance between the welding location and the PCHE block, hence reducing thermal gradient in to the bonded block. Welding tubes onto the topmost plate before diffusion bonding can relieve the local stress and it does not negatively affect the welding quality. However, it is challenging and potentially expensive to weld the tubes from the bonding surface side since the bottom surface of the topmost plate could be deflected due to the large thermal gradient from the welding process. Therefore, grinding the bottom surface back to its original flatness is required before diffusion bonding. In addition, a supporting plate must accommodate the weld fillet radius and thus pushes the effective loading area away from the tubes. It might not be a big issue, but taken to the extreme, it may cause channels crosstalk near the unloaded area.

Brazing of four headers onto the PCHE bonded block was used in the current study because it is an isothermal process and subsequently would not introduce large stress in diffusion bonds. Diffusion bonding the plates together while simultaneously brazing the tubes on to the topmost plate protects the integrity of the diffusion-bonded block and brazed joints. However, the aluminum and titanium content of Alloy 617 could cause incomplete wetting. The brazing parts

should be plated with nickel before the brazing process to prevent any incomplete wetting. By applying the above-mentioned techniques, the fabrication of the reduced-scale PCHE was completed. Figure 2-10 shows a picture of the diffusion-bonded block and channel inlets on plates through one of these headers. It was observed that the inlet channels were aligned, and the inlet recession surface was smoothed.

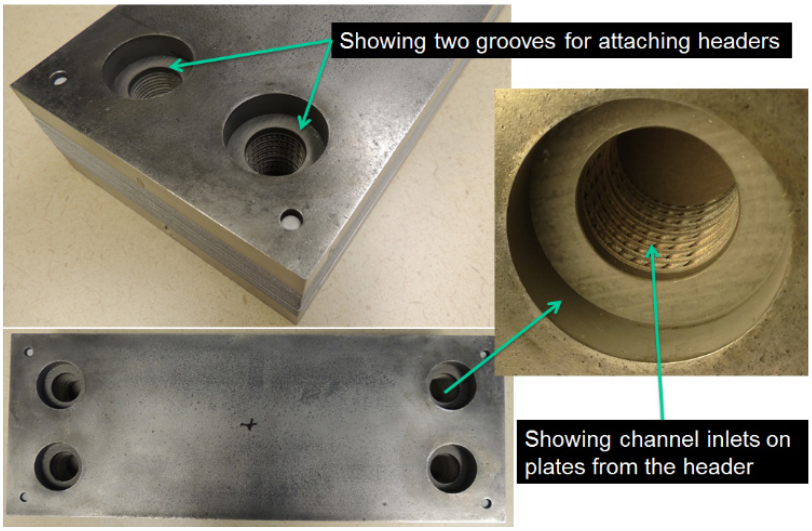

Figure 2-10. Photographs of the diffusion-bonded block and the channel inlets on plates.

A leakage test for the entire heat exchanger was conducted per ASTM helium leak test standard E493 using a helium leak detector. The diffusion-bonded block passed the leak test initially, but there was a leak near the brazed joint (leakage rate is about 6×10^{-9} l/sec). Re-brazing was performed to fix the small leak.

In summary, a zigzag-channel PCHE was designed using helium-to-helium working fluid combination, which had a nominal thermal load of approximately 13.0 kW. The design pressure and temperature were 3.0 MPa and 800 °C, respectively. The PCHE block was made of Alloy 617 plates and the four headers were made of Alloy 800H pipes. The PCHE block dimension is 13.35’’

× 4.96'' × 2'' (339.1 × 126 × 50.8 mm^3) with eight plates on each of the hot and cold sides, consisting of 11 chemically-etched zigzag channels. The actual assembly with four flow distribution headers is shown in Figure 2-11.

Figure 2-11. Photo of the fabricated zigzag-channel PCHE with four headers assembled.

2.8 Conclusion

In this chapter, a 1-D code for heat exchanger thermal design was developed. One reduced-scale PCHE was fabricated using Alloy 617 plates for the heat exchanger core and Alloy 800H pipes for the heat exchanger flow distribution headers. A comparison between the results obtained from the 1-D code and conventional LMTD method was carried out for both the prototype PCHE-type IHX and reduced-scale PCHE, respectively. The fabrication techniques and fabrication aspects of the zigzag-channel PCHE were also presented.

Chapter 3 PCHE Performance Testing Experiments

3.1 Overview

In this chapter, pressure drop and heat transfer characteristics of the fabricated zigzag-channel PCHE are investigated experimentally in the HTHF. New pressure drop and heat transfer correlations are developed based on the obtained experimental data. Comparisons between the experimental data and the results obtained from the available PCHE and straight circular pipe correlations are conducted. Finally, a heat loss analysis is presented.

3.2 High-Temperature Helium Test Facility

Experiments were performed to examine the thermal-hydraulic characteristics of the zigzag-channel PCHE under various steady-state conditions. The experimental study capitalized on the high-temperature helium test facility. Figure 3-1 presents the 3-D layout of the high-temperature helium test facility and Figure 3-2 shows a simplified 2-D schematic of the HTHF showing the helium flow path for heat exchanger testing, where one of the two previously-fabricated straight-channel PCHEs was replaced by the current reduced-scale zigzag-channel PCHE (i.e., the PCHE being tested). The HTHF was designed and constructed to facilitate thermal-hydraulic performance testing of compact heat exchangers at temperatures and pressures up to 850 °C and 3.0 MPa, respectively (Mylavarapu, 2011). The HTHF consists of a pre-heater and a main-heater

to heat helium to elevated temperatures, a gas booster to boost the helium pressure to overcome the pressure drop in the loop, a cooler to cool the working fluid helium to low temperatures before returning to the gas booster, piping, high-temperature valves, and various instruments. The pre-heater and main-heater are similar electric heaters with the same maximum heating capacity of about 23.0 kW. Three heating elements, each having a maximum capacity of approximately 7.6 kW, were embedded in the inner surface of the ceramic fiber insulation and were virtually free-radiating. The maximum heating element temperature can reach 1,300 °C, enabling high-temperature tests in the test loop. The helium flow in the test facility had periodical fluctuations due to the reciprocating actions of the booster, which is a single-stage, double-acting, air-driving booster. Therefore, an inline air-driving pressure regulator valve, in addition to a helium surge tank, was installed at a downstream location of the booster to damp the flow oscillations. To assure the experimental data quality, all the instruments were calibrated against standards traceable to the National Institute of Standards and Technology (NIST).

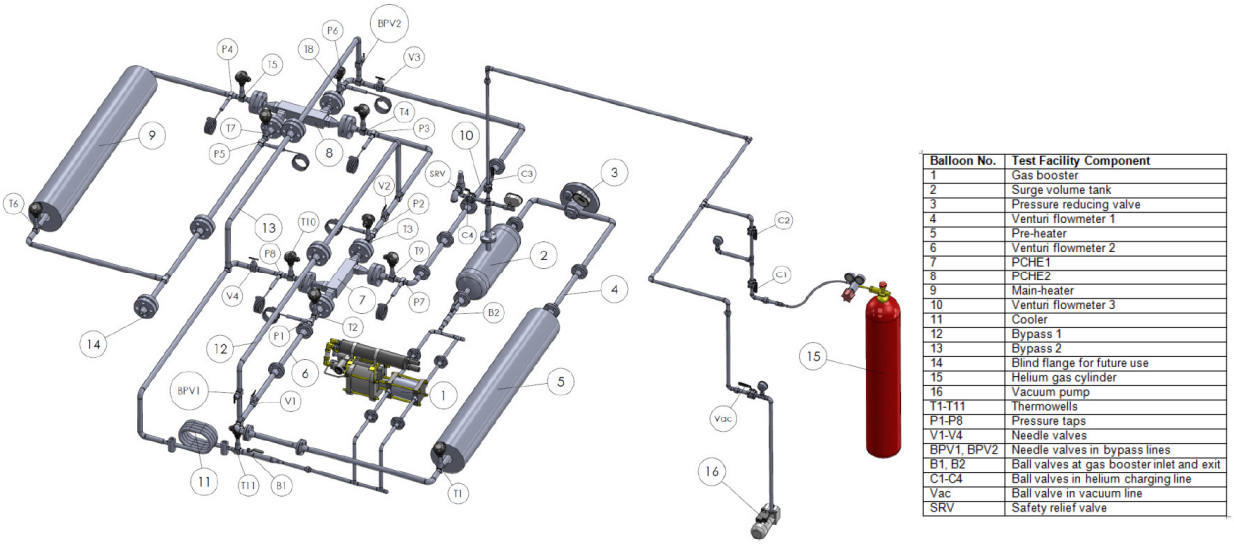

Balloon No.	Test Facility Component
1	Gas booster
2	Surge volume tank
3	Pressure reducing valve
4	Venturi flowmeter 1
5	Pre-heater
6	Venturi flowmeter 2
7	PCHE1
8	PCHE2
9	Main-heater
10	Venturi flowmeter 3
11	Cooler
12	Bypass 1
13	Bypass 2
14	Blind flange for future use
15	Helium gas cylinder
16	Vacuum pump
T1-T11	Thermowells
P1-P8	Pressure taps
V1-V4	Needle valves
BPV1, BPV2	Needle valves in bypass lines
B1, B2	Ball valves at gas booster inlet and exit
C1-C4	Ball valves in helium charging line
Vac	Ball valve in vacuum line
SRV	Safety relief valve

Figure 3-1. Layout of the high-temperature helium test facility (Mylavarapu, 2011).

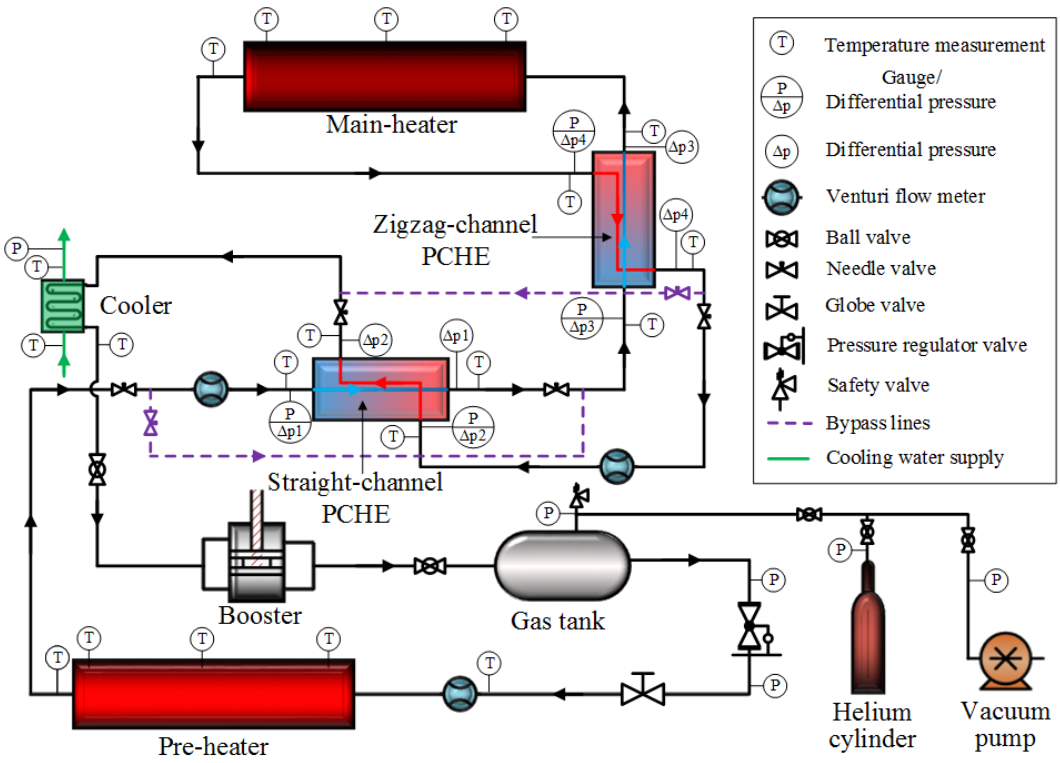

Figure 3-2. 2-D schematic of the high-temperature helium test facility (Chen et al., 2016a).

3.3 Experimental Data Reduction Method

3.3.1 Fanning friction factor

The test PCHE was installed in the HTHF for the determination of its pressure drop and heat transfer characteristics. The first step was to determine the friction characteristics, i.e., Fanning friction factor. The approach described by Chen (2015a) was adopted for this task. Figure 3-3 displays the pressure drop measurement locations on one side of the PCHE. Two differential pressure transducers were installed on each side of the test PCHE to measure pressure drops across both the hot and cold sides of the PCHE.

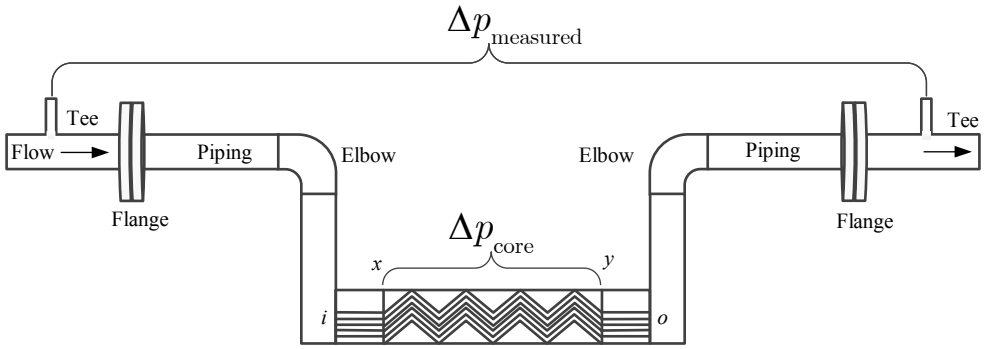

Figure 3-3. PCHE set-up schematic and illustration of pressure drop contributions.

It can be seen from Figure 3-3 that the total pressure drop measured on each side includes several contributors: pressure loss associated with the heat exchanger core; pressure loss associated with the fluid distribution devices, such as the distribution headers and plena; additional pressure loss at the straight-channel regions (i.e., regions between surfaces *i* and *x*, and *y* and *o* as shown in Figure 3-3) at the inlet and outlet of the heat exchanger (the average flow lengths for *i*-*x*, *x*-*y*, and *y*-*o* are 39.94, 203.3, and 34.11 mm, respectively); and pressure loss associated with the piping, fittings (tees and elbows), and flanges between the differential pressure measurement taps. Therefore, factors that cause pressure drop in the current PCHE are: (1) flow frictional losses in the heat exchanger core; (2) flow momentum rate change; (3) pressure drop associated with sudden contraction at the channel inlets; (4) pressure change associated with sudden expansion at the channel exits; and (5) pressure drops in straight-channel inlet and outlet regions, piping, fittings, and flanges.

To determine the friction characteristics of the PCHE core, it is necessary to exclude the pressure drop contributions that are not associated with the heat exchanger core frictional loss from the experimentally-measured pressure drop values. Other pressure drop contributions not related to

the heat exchanger core pressure drop were subtracted with the help of available empirical correlations in the literature. The experimental Fanning friction factor was then estimated from the core pressure drop for the zigzag channels of the PCHE. For the heat exchanger core frictional characteristics, the hot-side and cold-side pressure drops were separately obtained under elevated-temperature test conditions. Some assumptions made for pressure drop analysis were as follows: (1) the incoming flow is steady; (2) the fluid is uniformly distributed into each of the channel from the headers; (3) the channel geometry is identical for all channels on each of the cold and hot sides; (4) gravity effect is neglected since the heat exchanger is horizontally oriented; and (5) the cross sections of the flow channel passages are exactly semicircular. The total measured pressure drop is the sum of all the pressure drop contributions and can be expressed as,

$$\begin{aligned}\Delta p_{measured} = &\left(G^2/2\rho_i\right)\left[\left(1-\sigma^2+K_c\right)-\left(1-\sigma^2-K_e\right)\left(\rho_i/\rho_o\right)\right]+\\ &\left(G^2/2\rho_i\right)\left[2\left(\rho_i/\rho_o-1\right)+4f\left(l/d_h\right)\rho_i\left(1/\rho\right)_m\right]+\\ &\left(\Delta p_{straight-channel\ regions}+\Delta p_{fittings}+\Delta p_{piping}+\Delta p_{flanges}\right)\end{aligned} \quad . \tag{3.1}$$

The Fanning friction factor, f, the only unknown in Equation (3.1), can be determined from the experimental data. For flow in a straight circular pipe, Equation (3.2) can be used to calculate the Fanning friction factor for fully-developed flow.

$$f=\begin{cases}\dfrac{16}{\mathrm{Re}}, & \mathrm{Re}\le 2{,}300\\ \dfrac{1}{4}\left[\dfrac{1}{\left(0.79\ln\mathrm{Re}-1.64\right)}\right]^2, & \mathrm{Re}>2{,}300\end{cases} \tag{3.2}$$

3.3.2 Heat transfer coefficient

In the present experimental study, no local internal fluid and wall temperature measurements were available. Therefore, local and average convective heat transfer coefficients on both the hot and cold sides of the heat exchanger cannot be obtained directly. A typical method used for determining the average heat transfer coefficient on either side of the PCHE was adopted from Chen et al. (2016a) and is described in this section.

From the PCHE fabrication aspects, the hot-side heat transfer area and cold-side heat transfer area are the same (i.e., $A_{s,h} = A_{s,c} = A_s$). The overall thermal resistance is given by:

$$\frac{1}{UA_s} = \frac{1}{h_h A_{s,h}} + \frac{1}{h_c A_{s,c}} + R_w . \tag{3.3}$$

For a determined fluid, (i.e., helium), the heat transfer model is only a function of the Reynolds number (Nikitin et al., 2007 and Kim, 2012). The Prandtl number of helium was treated as a constant since its variations over the testing temperature range in the current study were less than 1%. The heat transfer coefficient for either side can be calculated from the Nusselt number, expressed as:

$$\mathrm{Nu} = c\,\mathrm{Re}^a \tag{3.4}$$

where a and c are constants. Therefore, the average heat transfer coefficient h is given by:

$$h = \frac{\mathrm{Nu}\lambda}{d_h} = \frac{c\,\mathrm{Re}^a\,\lambda}{d_h} . \tag{3.5}$$

Substituting Equation (3.5) into Equation (3.3) yields,

$$\frac{1}{Ud_h} = \frac{1}{c\,\mathrm{Re}_h^a\,\lambda_h} + \frac{1}{c\,\mathrm{Re}_c^a\,\lambda_c} + \frac{R_w A_s}{d_h} . \tag{3.6}$$

Two unknown constants a and c can be solved by using a nonlinear regression method to minimize the residual S as,

$$S = \sum_{j=1}^{N} \left[\frac{1}{U_j d_h} - \frac{R_{w,j} A_s}{d_h} - \frac{1}{c \, \mathrm{Re}_{h,j}^{a} \, \lambda_{h,j}} - \frac{1}{c \, \mathrm{Re}_{c,j}^{a} \, \lambda_{c,j}} \right]^2 . \tag{3.7}$$

Once a and c are determined, the Nusselt number correlation, i.e., Equation (3.4) is confirmed. The heat transfer coefficients for both the hot and cold sides can be calculated separately from the Nusselt number correlation.

To obtain the overall heat transfer coefficient of the zigzag-channel PCHE, it is necessary to determine the effective heat transfer area and consider the heat transfer contributions inside the heat exchanger. Figure 3-4 is a schematic showing the effective heat transfer area and heat conduction between the two adjacent ports. The heat transferred from the hot side to cold side consists of several contributions: (1) heat conduction from port #1 to port #2 and from port #3 to port #4; (2) heat transfer in the crossflow configurations in the X and Y regions; (3) heat transfer in the countercurrent flow region Z; and (4) heat loss to the surroundings. Four thermocouples were installed at locations 1, 2, 3, and 4 (see Figure 3-4) in the HTHF to measure the helium inlet and outlet temperatures of the test PCHE.

Three experimental data points were used to examine the heat conduction from port #1 to port #2 and from port #3 to port #4, i.e., contribution (1) as mentioned above. The average fraction of the total heat conduction to the total heat transferred from the hot side to cold side was about 0.4%, whereas the overall heat transfer coefficient was 1.1% higher than that without considering the heat conduction. Changes in the four terminal temperatures resulted in a decrease of the LMTD by

approximately 1.1%. A smaller LMTD gave a larger overall heat transfer coefficient when the heat conduction between the ports was neglected. In the current study, the heat conduction was considered. Note that the sum of the heat transfer area of regions X, Y, and Z, showing in Figure 3-4, is the effective heat transfer area that was used when processing the experimental data.

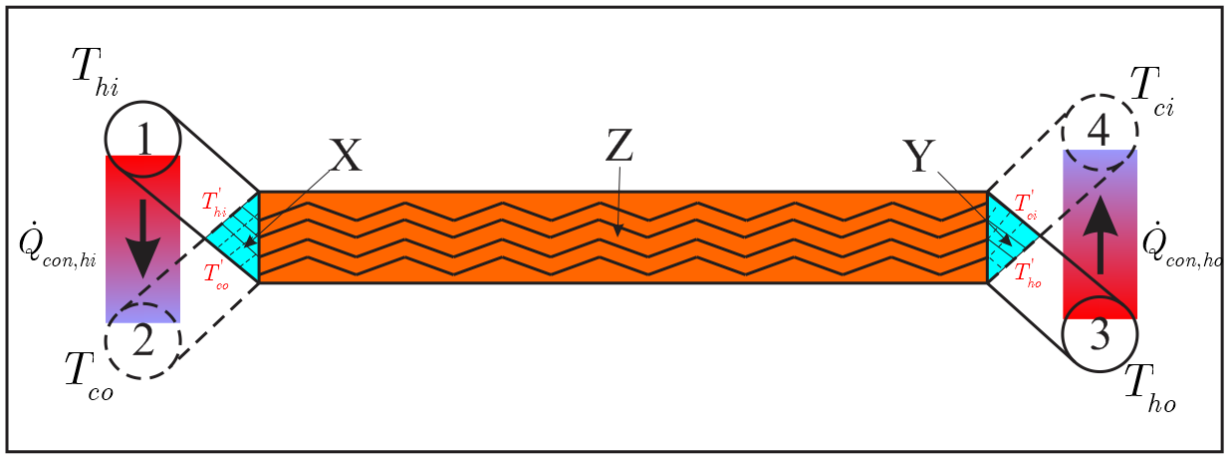

Figure 3-4. Schematic of the effective heat transfer area and heat conduction path (regions numbered 1, 2, 3, and 4 represent the hot-side and cold-side inlet/exit ports or plena).

3.3.3 Uncertainty analysis

An uncertainty analysis, considering error propagation, was performed using the root-sum-square method. The uncertainty in the Fanning friction factor was analyzed based on the simplified form of the heat exchanger core friction pressure drop given by

$$f = \frac{\Delta p}{2}\frac{d_h}{l}\frac{\rho A_c^2}{\dot{m}^2}. \tag{3.8}$$

The uncertainty in Fanning friction factor can be expressed as

$$\frac{\delta f}{f} = \sqrt{\left(\frac{\delta \Delta p}{\Delta p}\right)^2 + \left(\frac{\delta d_h}{d_h}\right)^2 + \left(2\frac{\delta \dot{m}}{\dot{m}}\right)^2 + \left(2\frac{\delta A_c}{A_c}\right)^2 + \left(\frac{\delta l}{l}\right)^2 + \left(\frac{\delta \rho}{\rho}\right)^2}. \tag{3.9}$$

The heat transfer model can be obtained using the nonlinear regression method. A perturbation method was adopted to determine the uncertainties in the obtained heat transfer correlation (Khartabil et al., 1992), i.e., uncertainties in constants a and c in Equation (3.4). The uncertainties in Re_h, Re_c, λ_h, λ_c, A_c, d_h, U, and R_w in Equation (3.7) can be determined from the experimental data. One of the eight variables was changed to its upper bound and the corresponding values of a_1 and c_1 were determined when running the nonlinear regression calculation. These two values were compared with the original values (i.e., a and c values) to determine the differences of Δa_1 and Δc_1. The same procedure was repeated for the low bound value of the same variable to obtain Δa_2 and Δc_2. These steps were repeated for the remaining seven variables. There were a total of 16 regression runs required to compute all individual relative errors in constants a and c. Finally, the uncertainties in a and c were calculated separately by taking the root-mean-square method as,

$$\begin{cases} \delta a = \sqrt{\dfrac{1}{n}\sum_{i=1}^{n}\left(\Delta a_i^2\right)} \\ \delta c = \sqrt{\dfrac{1}{n}\sum_{i=1}^{n}\left(\Delta c_i^2\right)} \end{cases}. \tag{3.10}$$

3.4 Experimental Results and Discussions

The thermal-hydraulic performance testing of the zigzag-channel PCHE was carried out in this section. The test loop was initially vacuumed by using a vacuum pump followed by charging the test loop with helium (with a purity rating of 99.9999%) to a desired pressure from a helium gas cylinder. The cooler was turned on during all the tests to lower the temperature of helium. The

primary measurements taken on the test PCHE consist of the helium inlet and outlet temperatures, pressure drops across the hot side and cold side, helium mass flow rates on both sides, and gage pressures at the inlet section of both sides. Due to the large thermal inertia of the test facility, it usually took more than five hours for the loop to reach the first steady-state condition starting from a room temperature. The criteria of reaching steady-state conditions were based on the standard deviations of the helium temperature, pressure, and helium mass flow rate measurements. The PCHE operation condition was considered as a steady state when the standard deviations of the four-measured helium inlet/outlet temperatures were less than 0.5 °C; the standard deviations of the measured static pressure and differential pressure were less than 3%; and the standard deviations of the measured helium mass flow rates were less than 2% in a two-minute duration at a sampling rate of 8 Hz (Mylavarapu et al., 2014).

Figure 3-5 shows a total number of 82 experimental data points plotted as functions of the helium mass flow rates, system pressures, and the PCHE hot-side helium inlet temperatures. The helium mass flow rates were varied from 22 to 39 kg/h, the system pressures were from 1.6 to 2.7 MPa while the hot-side helium inlet temperatures were increased from 199 to 802 °C. The maximum helium temperature, located at the exit of the main heater in the test loop, was about 840 °C. The heat exchanger thermal duty for each steady state was calculated based on the average thermal duty on both the hot and cold sides. The maximum heat exchanger thermal duty was about 15 kW in the current experiments. The heat loss ratio is defined as the ratio of the thermal duty difference between the hot side and cold side of the PCHE to the average thermal duty. The heat loss ratios were less than 10% for all experimental data points.

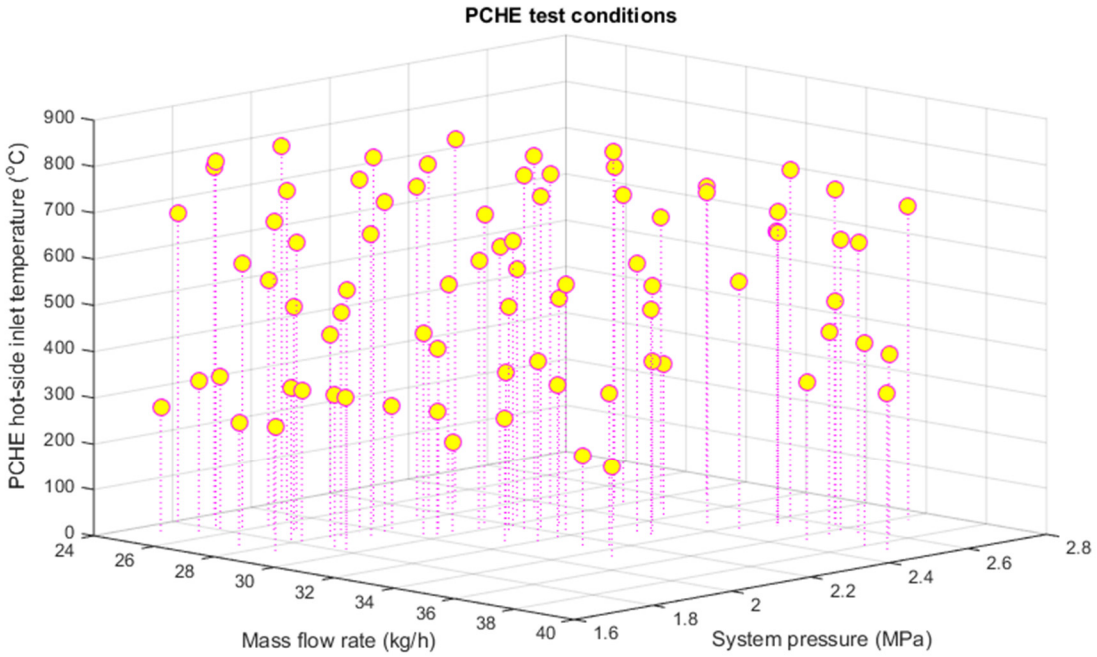

Figure 3-5. PCHE experimental test conditions.

3.4.1 Fanning friction factor

The experimental Fanning friction factors on both the hot and cold sides were obtained using the method described in Section 3.3.1 and plotted in Figure 3-6 and Figure 3-7 with the uncertainty bars representing the calculated uncertainties described in Section 3.3.3. In the current experiments, the relative uncertainties in the Reynolds numbers varied from 3.7 to 7.2%. It was observed from these figures that the Fanning friction factors tended to be a weak function of the Reynolds numbers when the Reynolds numbers were greater than about 2,200, which indicated the onset of the laminar-to-turbulent flow transition regime. The uncertainties of all the current experimental data were within ±10% when the flow variations were less than 2%. In addition, the uncertainties

of the friction factors were within ±6 and ±10% for the laminar and transition flow regimes, respectively, at 95% confidence level.

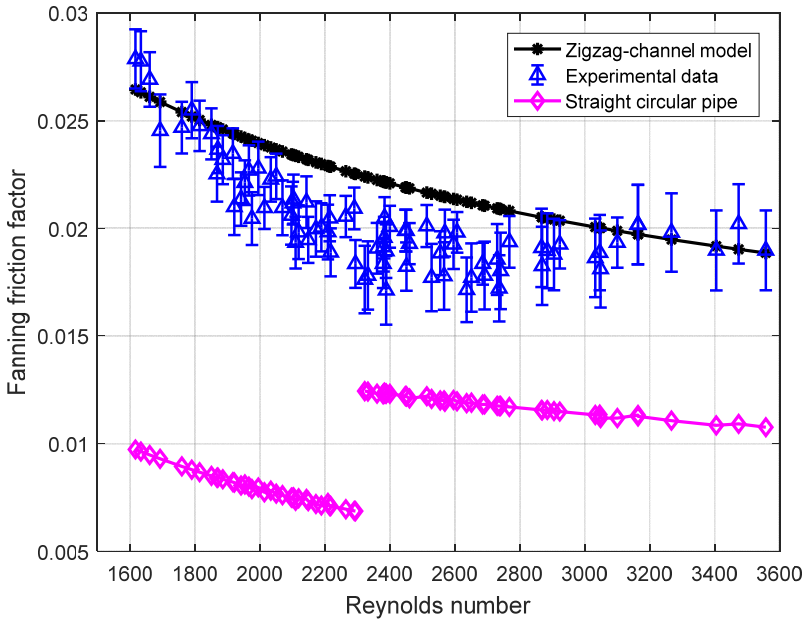

Figure 3-6. Cold-side Fanning friction factor.

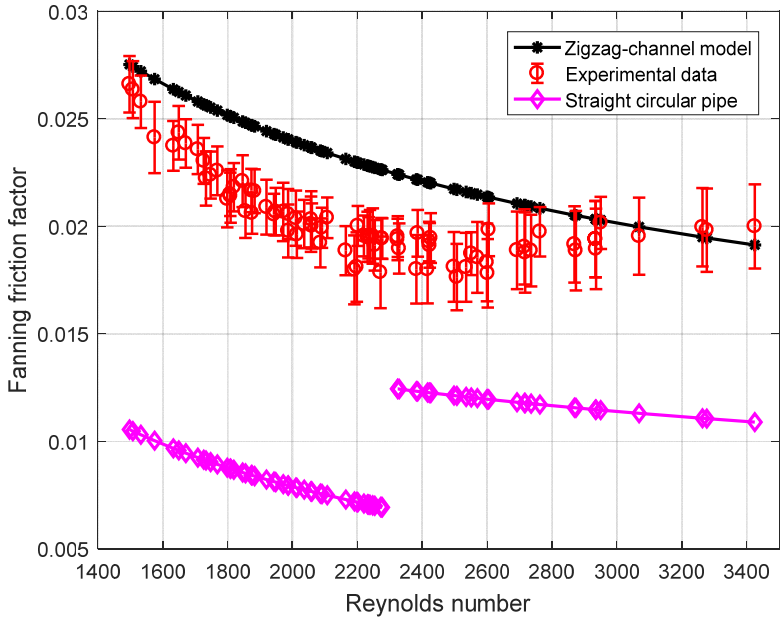

Figure 3-7. Hot-side Fanning friction factor.

The experimentally obtained Fanning friction factors were compared with the correlation developed by Kim (2012), as also shown in Figure 3-6 and Figure 3-7. The correlation shown in Equation (3.2) for fully-developed flow in straight circular pipe are also plotted in these two figures. The results calculated from the correlation developed by Kim slightly over predicted, in most cases, the experimentally obtained Fanning friction factor values. The largest differences were 29% for both the hot and cold sides. The discrepancies can be attributed to the geometric differences of the flow channels. The zigzag channels used in Kim's computational fluid dynamics simulations were with sharp turns at all bends in the channels, whereas a roundness was introduced at each bend in all channels of the currently-tested PCHE. Introducing a roundness to each bend smooths the fluid flow direction change and hence reduces the pressure drop. The second possible reason is due to the difference in the cross section of the flow channels. The channel cross sections in the test PCHE were not exactly semicircular due to the chemical etching properties, while Kim's numerical model was for the zigzag channel with a perfect semicircular cross section. When comparing the experimental data to the results obtained from the straight circular pipe correlations, it was found that the zigzag-channel Fanning friction factors were two to three times those in the laminar flow regime and about two times those in the transition flow regime.

Next, the obtained Fanning friction factors on both the hot and cold sides are plotted in Figure 3-8. It was observed that the Fanning friction factors on the hot side and cold side were different, especially in the laminar flow regime, which is postulated to be mainly due to the flow channel geometry. The channels' geometric parameters on the hot side and cold side are not identical due to manufacturing imperfections and tolerance. The Fanning friction factors on the cold side were

slightly larger than those on the hot side in the laminar flow regime, while in the transition flow regime, they became very similar.

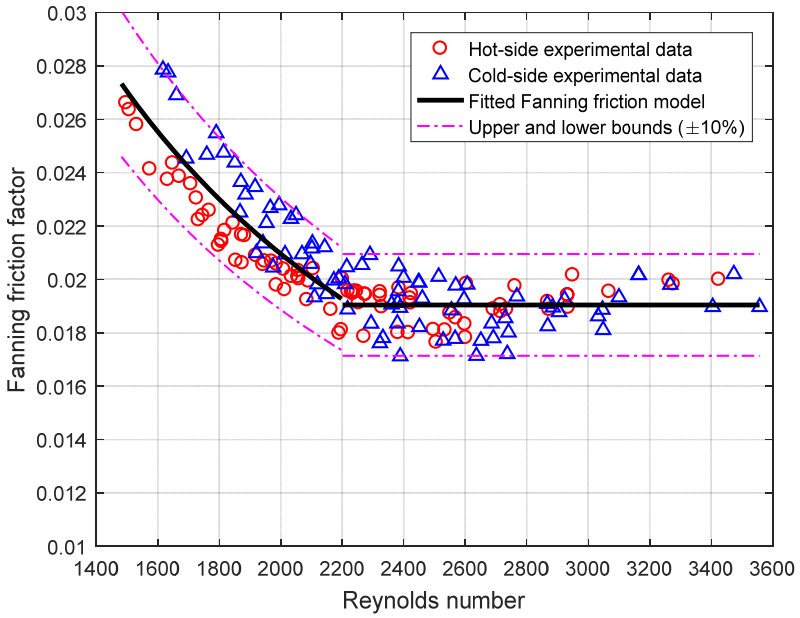

Figure 3-8. Experimentally determined Fanning friction factors for both the hot and cold sides and the fitted model.

A power function of the Reynolds number only was utilized to best fit 72 data points in the laminar flow regime for both the hot and cold sides. Since the Fanning friction factors were almost independent of the Reynolds numbers over the range covered in the transition flow regime, an average Fanning friction factor for the rest 92 experimental data points with twice the standard deviation of 0.000846, corresponding to the 95% confidence level, was selected for the transition flow regime. Following this exercise, we propose a new Fanning friction correlation for the current zigzag flow channels:

$$f = \begin{cases} \dfrac{17.639}{\mathrm{Re}^{0.8861 \pm 0.0017}} & 1,400 \le \mathrm{Re} \le 2,200 \\ 0.019044 \pm 0.001692 & 2,200 < \mathrm{Re} \le 3,558 \end{cases}. \tag{3.11}$$

The correlations shown above correlated 98 percent of the 164 experimental data points within ±10 percent deviations, as shown in Figure 3-8. Note that the proposed correlations are only valid for flow channels of similar geometry studied and the above-mentioned Reynolds number ranges.

3.4.2 Nusselt number

Local heat transfer coefficients could not be computed from our experiments since no internal wall and fluid temperature measurements were conducted in the current experimental tests. Therefore, the laminar-to-turbulent flow transition behavior could not be identified directly from the experimental data for heat transfer characteristics. The method used to determine the onset of the heat transfer transition regime in the current study was to examine the uncertainties in the constants of the fitted correlations using the nonlinear regression and uncertainty determination methods illustrated in Sections 3.3.2 and 3.3.3. Running nonlinear regression fittings for every 15 data points from low to high Reynolds numbers with a step of five data points, the uncertainty of the model in each run can be obtained. Also, the overall uncertainty of the model for the total 82 experimental data points can be calculated. Assuming the 15 data points for each nonlinear regression run were in the laminar regime (the highest Reynolds number is the onset of the transition regime), the uncertainties for all the runs and the overall uncertainty were compared as shown in Figure 3-9. It was observed that there was a steep jump and the fitted model uncertainty was larger than the overall uncertainty when Reynolds numbers were around 2,200. The computed uncertainties in the transition regime were larger than those in the laminar regime because both the flow and heat transfer behaviors in the transition flow regime are chaotic and difficult to predict. It was therefore reasonable to assume the onset of the laminar-to-turbulent heat transfer transition

regime occurred at a Reynolds number of approximately 2,200, which was the same as the onset of the transition regime for the fluid flow.

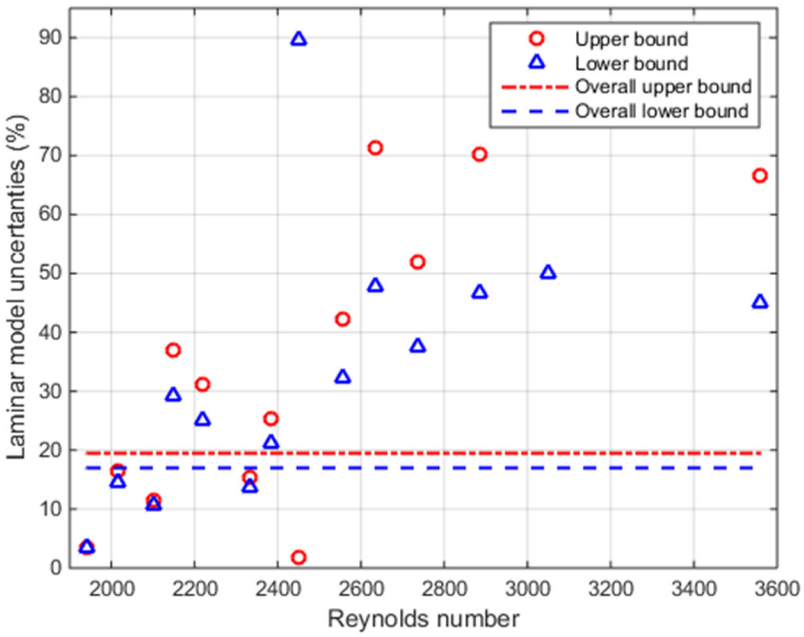

Figure 3-9. Fitted model uncertainties.

Following the heat transfer data reduction method illustrated in Section 3.3.2 for both the laminar and transition flow regimes, fitted correlations can be obtained from 67 data points that were randomly selected from the total 82 experimental data points using the nonlinear regression method as

$$\mathrm{Nu} = \begin{cases} \left(0.05516 \pm 0.00160\right)\mathrm{Re}^{\left(0.69195 \pm 0.00559\right)} & 1,400 \le \mathrm{Re} \le 2,200 \\ \left(0.09221 \pm 0.01397\right)\mathrm{Re}^{\left(0.62507 \pm 0.01949\right)} & 2,200 < \mathrm{Re} \le 3,558 \end{cases}. \tag{3.12}$$

The other 15 data points were used to validate the obtained correlations, i.e., Equation (3.12) described as follows. A comparison of the overall heat transfer coefficients obtained from the

experimental data and those calculated using Equations (3.6) and (3.12) is presented in Figure 3-10, which indicated that the two were in good agreement with each other. The differences were within 3% for both the laminar and transition flow regimes. Pra et al. (2008) conducted experiments on a Heatric PCHE mock up with similar geometry as the current tested PCHE at lower temperatures and found that Reynolds number power values are from 0.6 to 0.8, giving similar results as in the present tests.

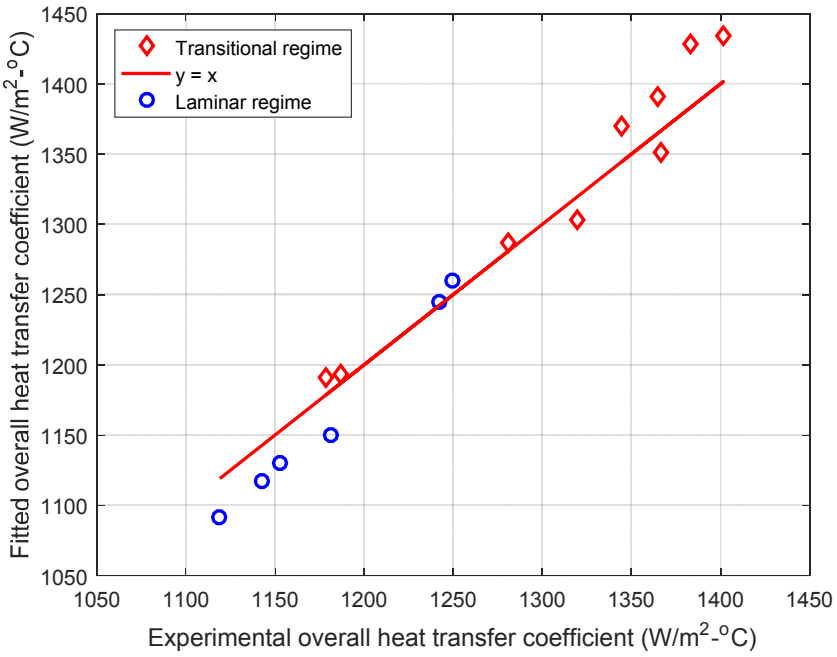

Figure 3-10. Overall heat transfer coefficient comparison between the fitted model and experiments.

Finally, the fitted Nusselt number as a function of Reynolds number only is plotted in Figure 3-11. It shows that the Nusselt numbers increased gradually with the increase of the Reynolds numbers, which was due to the helium velocity increase, resulting in a more turbulent fluid flow. The uncertainties of the Nusselt number correlations for the laminar and transition flow regimes were found to be ±7 and ±35%, respectively, at the 95% confidence level. As mentioned, the behavior in the transition flow regime is complicated, resulting in the higher uncertainties.

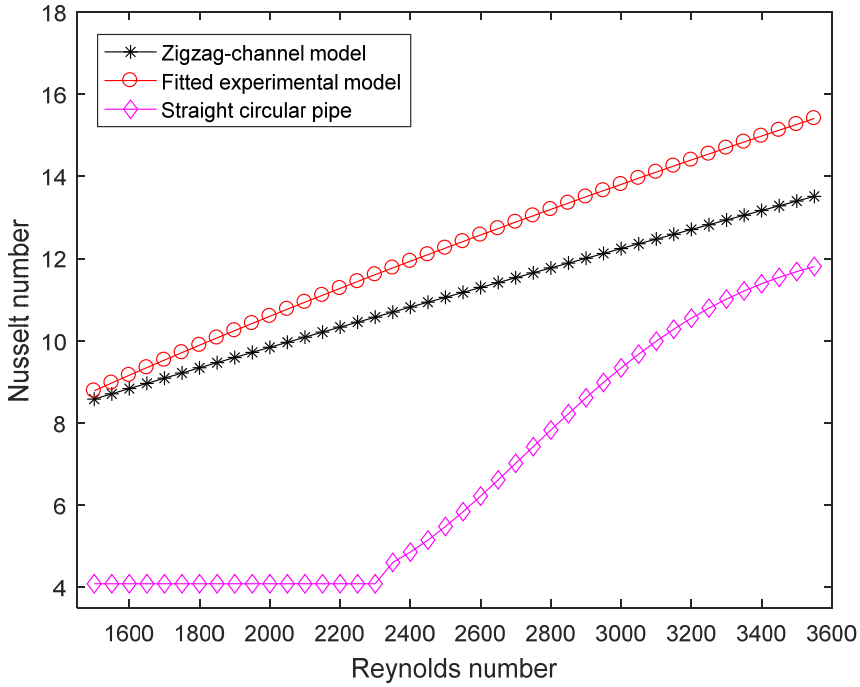

Figure 3-11. Fitted Nusselt number correlation compared with the zigzag and straight circular pipe correlations.

Figure 3-11 also shows a comparison between the Nusselt number correlations shown in Equation (3.12) and that gave in Kim's correlation developed for zigzag flow channels (Kim, 2012). There were some discrepancies between the two correlations, where Kim's correlation had a slower increasing trend in the Nusselt number with the Reynolds numbers than the current correlations. As the Reynolds numbers were increased, the differences between these two methods increased from 1 to 9%. The disagreement can be attributed to the differences in the channel geometry. In addition, the boundary conditions for the top, bottom, and two side walls used in Kim's simulation were periodic (Kim, 2012), while the actual testing boundary conditions in the current experiments may not reflect the condition used in Kim's simulations. A comparison of the Nusselt number correlation with fully-developed straight circular pipe correlations (Figley et al., 2013) is also presented in Figure 3-11. The heat transfer coefficient in the current PCHE was about twice to

three times that in straight circular pipes in the laminar flow regime and 1.5 to three times that in the transition flow regime.

3.5 Heat Loss Analysis

The reduced-scale zigzag-channel PCHE was operated under high-temperature conditions, the heat loss from the heat exchanger insulation surfaces to the surroundings may be significant. Although the total heat loss from both the hot and cold sides was accounted during the experimental data reduction, heat loss was assumed to be equal on both sides. Compared to the heat loss on cold side, hot side had higher temperature and could have larger heat loss. This section presents a method to determine the heat duty of the heat exchanger accounting for the heat loss to the surroundings following Yoon et al. (2016). To determine the heat loss of a heat exchanger, only the fluid inlet and outlet temperatures, mass flow rates, and pressures of the hot and cold fluids are required from experiments. Figure 3-12 displaces a simplified heat exchanger schematic showing the heat balance between the hot side and cold side, as well as the heat loss to the surroundings.

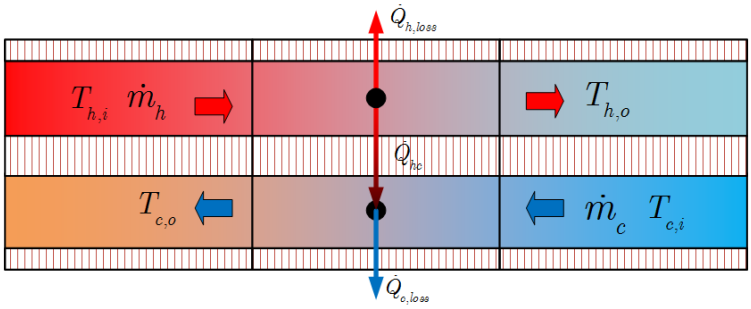

Figure 3-12. A simplified heat exchanger schematic for heat loss analysis.

From energy conservation,

$$\begin{cases} \dot{Q}_{h,net} = \dot{Q}_{hc} + \dot{Q}_{h,loss} = \dot{m}_c c_p \left(T_{h,i} - T_{h,o} \right) = C_h \Delta T_h \\ \dot{Q}_{c,net} = \dot{Q}_{hc} - \dot{Q}_{c,loss} = \dot{m}_c c_p \left(T_{c,o} - T_{c,i} \right) = C_c \Delta T_c \end{cases}. \tag{3.13}$$

The total heat loss from the heat exchanger insulation surface to the surroundings can be written as,

$$\dot{Q}_{t,loss} = \dot{Q}_{h,loss} + \dot{Q}_{c,loss} = \dot{Q}_{h,net} - \dot{Q}_{c,net} = C_h \Delta T_h - C_c \Delta T_c, \tag{3.14}$$

where C_h and C_c are the heat capacity rates of hot-side fluid and cold-side fluid, respectively. A heat loss ratio, γ, is defined as the ratio of the heat loss on hot side to the total heat loss. Therefore,

$$\dot{Q}_{h,loss} = \gamma \dot{Q}_{t,loss}, \quad \dot{Q}_{c,loss} = \left(1-\gamma\right) \dot{Q}_{t,loss}, \quad 0 < \gamma < 1. \tag{3.15}$$

The heat duty of the heat exchanger can be obtained by,

$$\dot{Q}_{hc} = \left(1-\gamma\right) C_h \Delta T_h + \gamma C_c \Delta T_c. \tag{3.16}$$

Then the heat exchanger effectiveness is,

$$\varepsilon \equiv \frac{\dot{Q}_{hc}}{\dot{Q}_{\max}} = \frac{\left(1-\gamma\right) C_h \Delta T_h + \gamma C_c \Delta T_c}{C_{\min} \left(T_{h,i} - T_{c,i} \right)}, \quad C_{\min} = \min\left(C_h, C_c \right). \tag{3.17}$$

From ϵ-NTU method, the heat exchanger effectiveness is given as,

$$\varepsilon = \frac{1 - \exp\left[-\mathrm{NTU}\left(1 - C^*\right) \right]}{1 - C^* \exp\left[-\mathrm{NTU}\left(1 - C^*\right) \right]}. \tag{3.18}$$

γ can be calculated based on Equations (3.17) and (3.18) as,

$$\gamma = \frac{\varepsilon C_{\min} \left(T_{h,i} - T_{c,i} \right) - C_h \Delta T_h}{C_c \Delta T_c - C_h \Delta T_h}. \tag{3.19}$$

However, it is necessary to measure the heat loss to calculate the NTU in Equation (3.18), which is not applicable in this analysis. An approximately estimation of heat loss ratio from the hot side can be obtained by,

$$\frac{\dot{Q}_{h,loss}}{\dot{Q}_{c,loss}} = \frac{\gamma Q_{t,loss}}{\left(1-\gamma\right)Q_{t,loss}} \approx \frac{\overline{T}_h - T_{air}}{\overline{T}_c - T_{air}}. \tag{3.20}$$

The heat loss ratio can be calculated by,

$$\gamma = \frac{\overline{T}_h - T_{air}}{\overline{T}_h - 2T_{air} + \overline{T}_c}. \tag{3.21}$$

The heat exchanger thermal duty for each steady state was calculated based on the average thermal duty on both the hot and cold sides and the maximum heat exchanger thermal duty was about 15 kW. Figure 3-13 (a) and (b) present the total heat loss and the hot-side heat loss ratio against the heat exchanger average temperature (i.e., the arithmetic mean temperature of the fluids at the four terminal locations of the heat exchanger), respectively. The heat loss ratio is defined as the ratio of the heat loss on hot side to the total heat loss. It can be observed that the maximum total heat loss is approximately 1.1 kW and the heat loss ratios on the hot side are between 53.5 to 55.6% for all experimental data points.

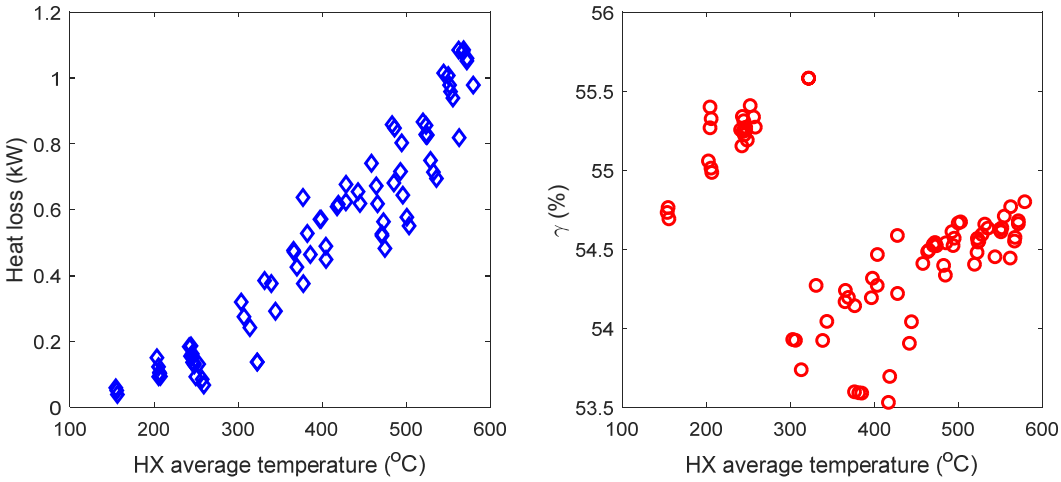

(a) (b)

Figure 3-13. Heat exchanger total heat loss and heat loss ratio.

3.6 Conclusion

In this study, the thermal-hydraulic performance of the fabricated zigzag-channel PCHE was investigated experimentally in the HTHF. The maximum PCHE test temperature reached was 802 °C. Pressure drop characteristics obtained from the experiments presented some discrepancies between the hot side and cold side, which could be mainly attributed to manufacturing variations and distortion of channels. The Fanning friction factors in zigzag channels were two to three times than those in straight circular pipes for laminar flow regime and about two times greater than those for transition flow regime. New pressure drop and heat transfer correlations for the zigzag-channel PCHE were also developed based on the obtained experimental data. Finally, heat loss from each side to the surroundings was also estimated.

Chapter 4 PCHE Numerical Modeling

4.1 Overview

This chapter presents a three-dimensional CFD study of the fabricated PCHE using a simplified geometry model. A comparison of the experimental data and simulation results is also carried out. Local thermal-hydraulic performance is numerically evaluated. In addition, several effects on PCHE's performance are examined, including the thermal boundary conditions, radiuses of curvature, thermophysical properties, zigzag angles, and channel flow pitch lengths. Optimization study of PCHE channel geometry using a multi-objective optimization method is also provided. Finally, the stress field of a short PCHE segment is numerically obtained.

4.2 Numerical Modeling

4.2.1 Numerical simulation model

A three-dimensional CFD study was carried out using STAR-CCM+. Modeling a full-size laboratory-scale PCHE is highly time consuming and can lead to prohibitively high computational costs. Therefore, a simplified geometry model that still could provide insights to the heat exchanger performance, consisting of one hot-side flow channel, one cold-side flow channel, and the associated solid structural metal, as shown in Figure 4-1, was modeled for the current

simulations. The cross-sectional shape of both cold- and hot-side channels is semicircular with a nominal diameter of 2.0 mm in the span-wise direction. The geometrical parameters of the computational domain were created to match the nominal values of the core region of the fabricated PCHE. The plate thickness is 1.6 mm and the width of the plate is 2.5 mm. The shape of the channels along the fluid flow direction is zigzag with a 4-mm-radius roundness at the tip of each bend. The geometry model was comprised of a total of 16 zigzag bends per channel. The plates were made of Alloy 617 whose thermophysical properties were found from Special Metals (Special Metals, 2017), as shown in Table 4-1. The specific heat capacity was formulated as a temperature-dependent function and the thermal conductivity values were tabulated as a table file. Both the specific heat capacity function and thermal conductivity table were implemented into STAR-CCM+. The density of Alloy 617 was considered as constant of 8,360 kg/m^3. The temperature-dependent thermophysical properties of helium were taken from NIST (National Institute of Standards and Technology) and were also implemented into STAR-CCM+. Note that the dependence of the helium density on its pressure was neglected since the pressure drop across the PCHE channels was relatively small compared to the operating pressure of 3.0 MPa.

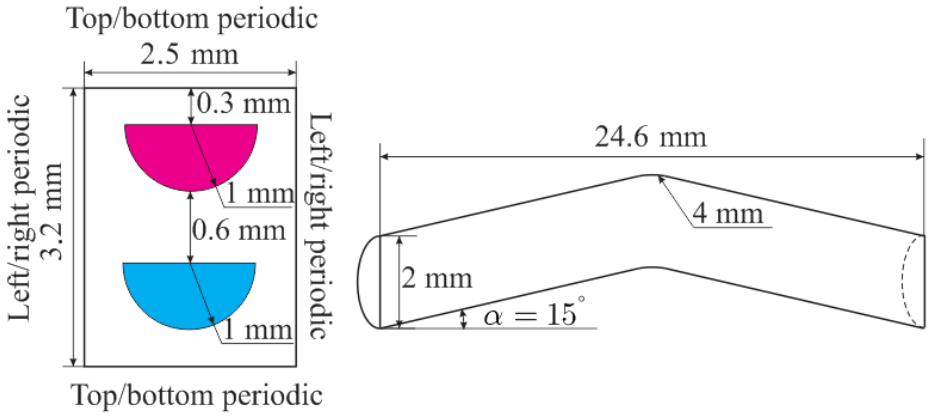

Figure 4-1. Simplified geometry model with its geometrical parameters and boundary conditions.

Table 4-1. Alloy 617 thermophysical properties (Special Metals, 2017).

Temperature, K	Thermal conductivity, W/m-K	Specific heat, J/kg-K
293.15	13.4	419
373.15	14.7	440
473.15	16.3	465
673.15	19.3	515
873.15	22.5	561
1,073.15	25.5	611
1,273.15	28.7	662

Three boundary conditions were used in the model: fluid inlet, fluid outlet, and wall. Fluid inlets were chosen as the mass flow rate inlets on both the hot and cold sides. The fluid outlets were selected as the pressure outlets on both sides. The left and right walls, as shown in Figure 4-1, were coupled and set as a periodic boundary type. Similarly, the top and bottom walls used a thermally-coupled periodic boundary type. The front and back surfaces were specified as adiabatic walls. In this numerical study, the helium inlet temperatures were 800 and 350 °C on the hot side and cold side, respectively. The helium outlet pressures on both sides were set to 3.0 MPa. To perform 3-D conjugate heat transfer simulations, steady state, laminar flow, and constant helium inlet temperatures were assumed while the thermal radiation effects and viscous dissipation were neglected in the simulations.

4.2.2 Grid independence study

To examine the spatial convergence of the CFD simulations, a grid independence study was conducted based on the Richardson's extrapolation method. Following Celik and Karatekin (1997), a summary of the method is presented. The cell or grid size h is defined as,

$$h = \left[\frac{1}{N} \sum_{k=1}^{N} \left(\Delta V_k \right) \right]^{1/3}, \tag{4.1}$$

where ΔV_k is the volume of the k^{th} cell and N is the total number of cells used for the entire computational domain. Three sets of grid sizes were selected with a refinement factor greater than 1.3 as suggested by Celik (2000). The refinement factor is defined as,

$$r = \frac{h_{coarse}}{h_{fine}}. \tag{4.2}$$

The apparent order for each monitored result is determined as,

$$p = \frac{1}{\ln r_{21}} \left| \ln \left(\frac{\phi_3 - \phi_2}{\phi_2 - \phi_1} \right) + \ln \left(\frac{r_{21}^p - s}{r_{32}^p - s} \right) \right|, \qquad s = \text{sign} \left(\frac{\phi_3 - \phi_2}{\phi_2 - \phi_1} \right), \tag{4.3}$$

where ϕ_1, ϕ_2, and ϕ_3 denote the simulated values for fine, medium, and coarse meshes, respectively. It is recommended that the value of p be limited from 1 to 2. However, it could be greater than 2 when local parameters are monitored. If $s = -1$, it is an indication of oscillatory convergence. Conversely, it is monotonic convergence when $s = 1$. The extrapolated value is computed as,

$$\phi_{ext}^{21} = \frac{\left(r_{21}^p \phi_1 - \phi_2 \right)}{\left(r_{21}^p - 1 \right)}. \tag{4.4}$$

The approximate relative error can be obtained as,

$$e_a^{21} = \left| \frac{\phi_1 - \phi_2}{\phi_1} \right|. \tag{4.5}$$

The grid convergence index (GCI) is determined by,

$$\text{GCI}_{fine}^{21} = \frac{F_s e_a^{21}}{r_{21}^p - 1}. \tag{4.6}$$

where F_s is a safety factor and it was selected as 1.25 for the three grids.

The software package, STAR-CCM+, provides several meshing strategies that can be used for different applications. In this study, parts-based meshing was selected with surface and polyhedral meshers. A grid independence study was carried out for the simplified simulation model with a helium mass flow rate of 1.1238×10^{-4} kg/s for both the cold and hot sides, which corresponded to the largest mass flow rate on both sides in the current simulations. Three grids with different numbers of cells were generated, as listed in Table 4-2. The helium outlet temperatures on both sides only had small differences compared to the finest mesh case. However, it presented an oscillatory convergence and the grid convergence indexes (GCIs) for the hot-side and cold-side temperatures were 0.39 and 0.26%, respectively. For the pressure drops along the channels, the GCIs were 4.1 and 3.78% on the hot side and cold side, respectively. The GCI represents the comparison of discrete solutions at different grid resolutions, which is a measure of how far the solution is from the unknown exact solution. Due the nature of the polyhedral mesh, one test is not sufficient for verifying conservative of the obtained GCIs. One additional set of grid independence study was conducted and gave similar GCIs. Therefore, in the current study, the fine mesh with a number of cells of 7.21 million, as shown in Figure 4-2, was considered sufficient and was used in all the following simulations.

Table 4-2. Results of grid independency study.

Mesh type	No. of cells, M	Grid size, 10^{-6} m	Δp_h, Pa	Δp_c, Pa	$T_{h,o}$, °C	$T_{c,o}$, °C
Fine mesh	7.21	61.5	27,939.8	23,139.0	511.5	642.7
Medium mesh	2.39	89.0	26,890.3	22,256.8	513.0	641.0
Coarse mesh	0.73	132.0	24,535.0	20,171.6	508.6	645.2
			Monotonic convergence		Oscillatory convergence	
Apparent order			2.07	2.21	1.79	2.31
Extrapolated value			28,856.8	23,838.8	509.9	644.1
Approximate relative error, %			3.76	3.81	0.29	0.27
Extrapolated relative error, %			3.18	2.94	0.31	0.20
GCI, %			4.10	3.78	0.39	0.26

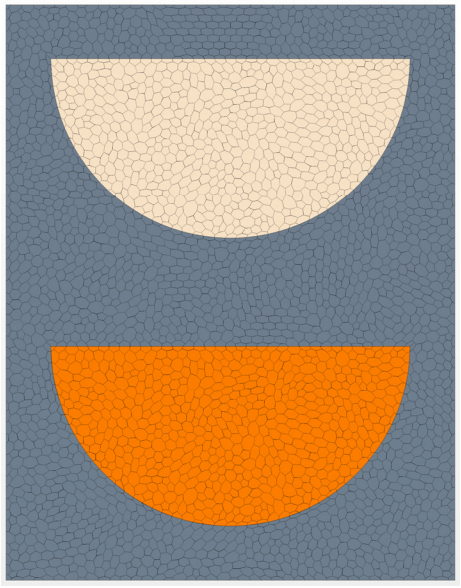

Figure 4-2. An image of the fine mesh.

4.2.3 Numerical data reduction and methodology

The global pressure loss factor for each fluid is defined as,

$$f_g = \frac{\triangle p_f d_h \overline{\rho} A_c^2}{2 l \dot{m}^2}, \tag{4.7}$$

where d_h, A_c, and l denote the channel hydraulic diameter, channel cross-sectional area, and actual fluid flow length, respectively. The mean fluid density, $\overline{\rho}$, is specified using the arithmetic mean temperature as the reference temperature based on the helium inlet and outlet temperatures on each side. Δp_f is the pressure loss, which can be expressed as,

$$\triangle p_f = \triangle p_t - \triangle p_{ad}, \tag{4.8}$$

where Δp_t and Δp_{ad} are the total pressure drop and the pressure drop due to flow acceleration or deceleration, respectively. The hydrostatic pressure drop was neglected in the simulations. For a small segment, the local pressure loss factor is defined as,

$$f_i = \frac{\triangle p_{f,i} d_h \overline{\rho} A_c^2}{2 \triangle l_i \dot{m}^2}, \tag{4.9}$$

where the subscript, i, denotes the i^{th} segment. The mean pressure loss factor over the entire flow channel can be computed as,

$$\overline{f} = \frac{1}{n} \sum_{i=1}^{n} f_i, \tag{4.10}$$

where *n* is the total number of segments along one flow channel. Basically, the first approach of calculating the global pressure loss factor is to apply Equation (4.9) to the entire channel length on each side.

Three heat transfer coefficient definitions were used in the numerical study, which are the local heat transfer coefficient, h_j, channel mean heat transfer coefficient, $\overline{h}$, and global heat transfer coefficient, h_g. The local heat transfer coefficient is defined as,

$$h_j = \frac{\dot{q}_j''}{\left|T_{f,j} - T_{w,j}\right|}, \tag{4.11}$$

where the subscript, j, denotes the j^{th} cross section; $\dot{q}''$ is the surface-averaged heat flux; T_w is the surface-averaged temperature on the wall that is in contact with the surrounding fluid; and T_f is the reference fluid temperature. For the local heat transfer coefficient definition, the fluid bulk (mean) temperature is used for T_f. The fluid mean temperature is given as (Incropera et al., 2007),

$$T_{f,c} = \frac{\int \rho u c_p T \mathrm{d}A}{\int \rho u c_p \mathrm{d}A}. \tag{4.12}$$

The mean heat transfer coefficient over the entire channel can be computed as,

$$\overline{h} = \frac{1}{m}\sum_{j=1}^{m} h_{c,j}, \tag{4.13}$$

where *m* is the total number of segmented cross sections.

The global heat transfer coefficient is given by,

$$h_g = \frac{\dot{q}_g''}{\left|T_{f,g} - T_{w,g}\right|}, \tag{4.14}$$

where $T_{f,g}$ is defined as the arithmetic mean of the fluid inlet and outlet temperatures and $T_{w,g}$ is the arithmetic mean of the four terminal temperatures of a heat exchanger. They can be written as,

$$T_{f,g} = \frac{\left(T_{in} + T_{out}\right)}{2} \ , \tag{4.15}$$

$$T_{w,g} = \frac{\left(T_{h,in} + T_{h,out} + T_{c,in} + T_{c,out}\right)}{4}. \tag{4.16}$$

4.3 Numerical and Experimental Comparisons

As studied in Chapter 3, the experimental pressure loss factors for the zigzag flow channels with uncertainty bars representing the calculated uncertainties at the 95% confidence level for both the hot and cold sides. The relative uncertainties in the Reynolds numbers varied from 3.7 to 7.2% in those experimental data. The uncertainties of the current experimental data were within $\pm$6% in the pressure loss factors in the laminar flow regime. The pressure loss factors obtained from the experimental data were approximately 17% less than the global pressure loss factors obtained from the numerical simulations, as shown in Figure 4-3. One of the reasons for the discrepancy could be any potential distortion in the cross-sectional shape and the dimensions of the flow channels after diffusion bonding. One example for the channel distortion is shown in Figure 4-4.

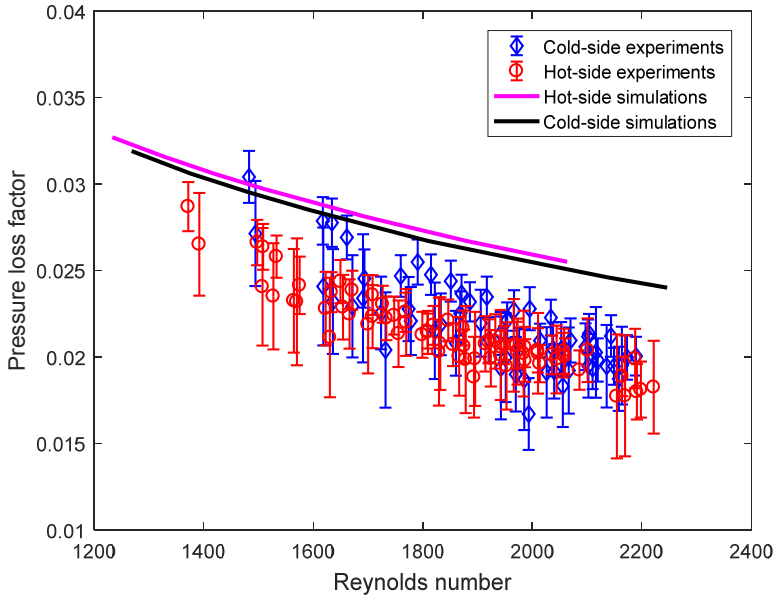

Figure 4-3. Comparison of experimental and numerical pressure loss factors.

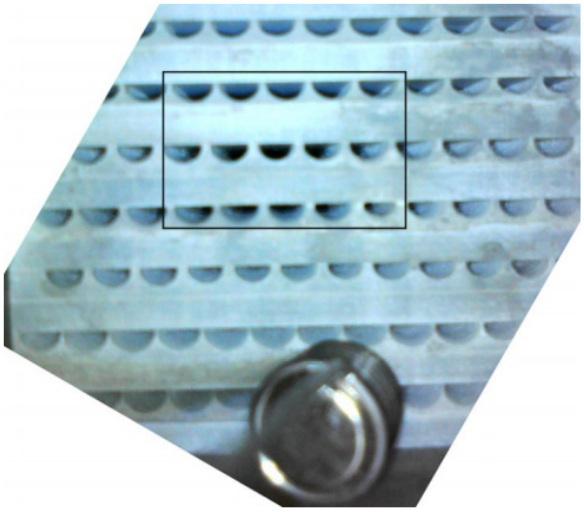

Figure 4-4. PCHE frontal face picture after diffusion bonding (Wegman, 2016).

Local heat transfer coefficients could not be deduced from the experimental data since no internal wall and fluid temperature measurements were conducted in the experiments available in the literature. The heat transfer coefficients obtained from the steady-state experiments were the global heat transfer coefficients. Figure 4-5 shows the comparison of the Nusselt numbers obtained from

the STAR-CCM+ simulations and the experimental values computed from Equation (4.14). The uncertainties of the Nusselt number for the laminar flow regime were found to be within ±10% on both sides, at the 95% confidence level. Although the numerically obtained Nusselt numbers were slightly higher than the experimental results, they had very similar trends and most of the simulation results were within the experimental uncertainty bars.

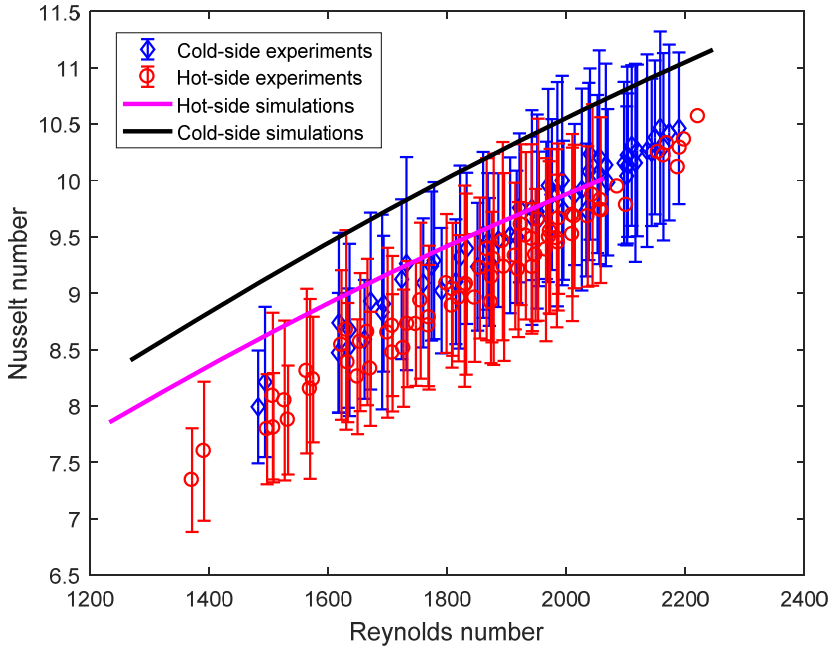

Figure 4-5. Comparison of the experimental and numerical Nusselt numbers.

4.4 Numerical Results and Discussions

4.4.1 Local thermal-hydraulic performance analysis

As noted, the local helium and solid temperatures and helium pressures inside the test PCHE were not available from our experiments. One advantage of the numerical simulations is that the local

information, such as the temperatures, pressures, and velocities, inside the heat exchanger can be readily obtained. The base case studied here is for both the hot-side and cold-cold inlets having the same mass flow rate of 5.108×10^{-5} kg/s, which gives a balanced heat capacity on the both sides. Figure 4-6 shows the temperature distributions in the fluid and solid metal inside the heat exchanger and Figure 4-7 displays the gauge pressure distribution on both the hot and cold sides along the fluid flow directions of the heat exchanger. It was observed that the temperature distributions on each side were approximately linear, which was expected due to the equal heat capacities ($\dot{m}c_p$) on the two sides. The helium flow on the cold side accelerated from the inlet to the outlet, while the helium velocity decreased from the inlet to the outlet on the hot side, as shown in Figure 4-8. The changes in the helium temperature along the helium flow directions resulted in helium density decreasing on the cold side while increasing on the hot side of the heat exchanger. It can also be seen that the velocity on the hot side was higher than that on the cold side inside the heat exchanger, which is due to the smaller helium density on the hot side. In addition, the pressure drop on the hot side was slightly larger than that on the cold side, as shown in Figure 4-7. Figure 4-9 shows the contours of the local pressure, velocity magnitude, and temperature on several cross sections inside the flow channel. The velocity profile inside the heat exchanger changed along the fluid flow direction, which indicated that a fully-developed flow condition and periodic changes were not reached in the current simulations. This could be attributed to the wavy nature of the zigzag flow channels as well as the temperature variations along the flow channels, resulting in large fluid property variations.

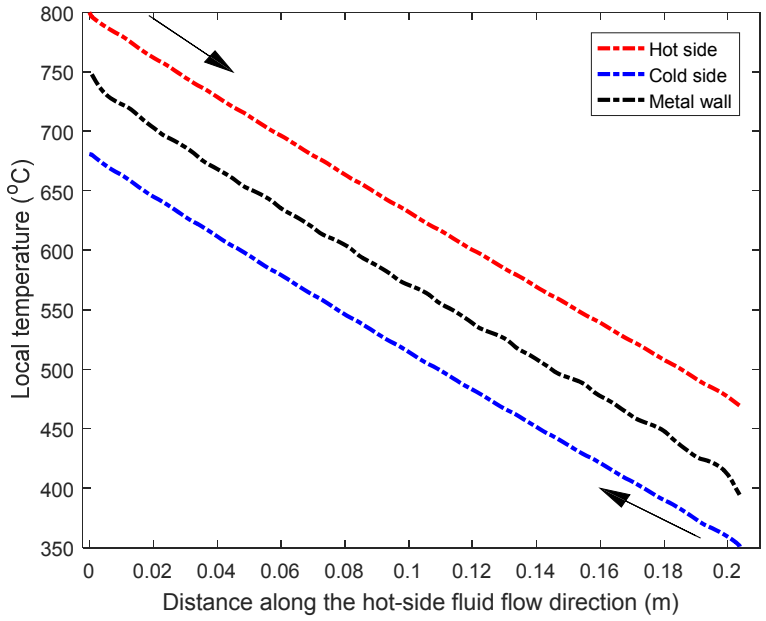

Figure 4-6. Local temperature distributions along the fluid flow directions from the STAR-CCM+ simulations.

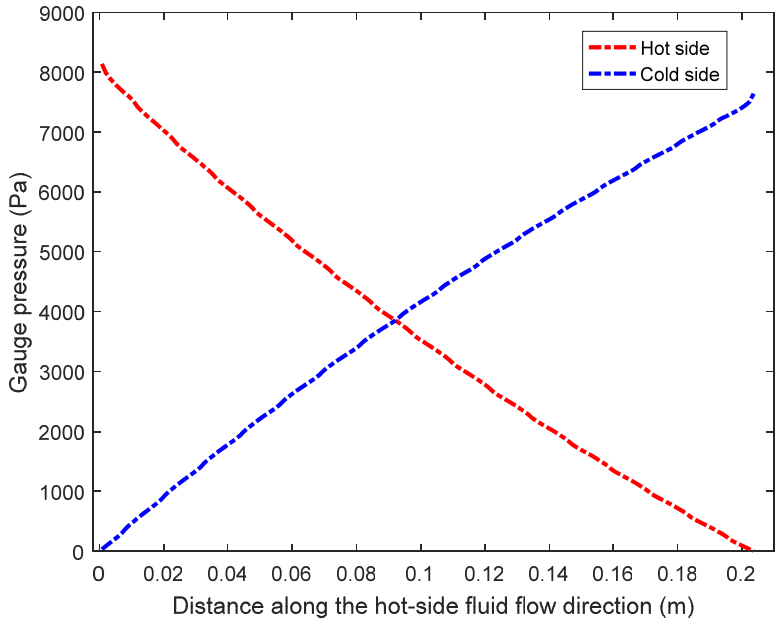

Figure 4-7. Gauge pressure inside the heat exchanger from the STAR-CCM+ simulations.

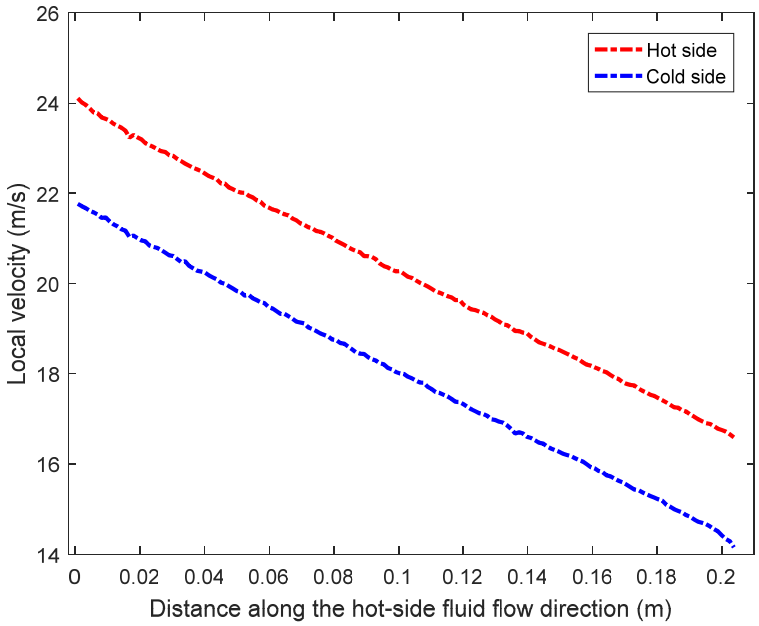

Figure 4-8. Velocity distributions inside the heat exchanger from the STAR-CCM+ simulations.

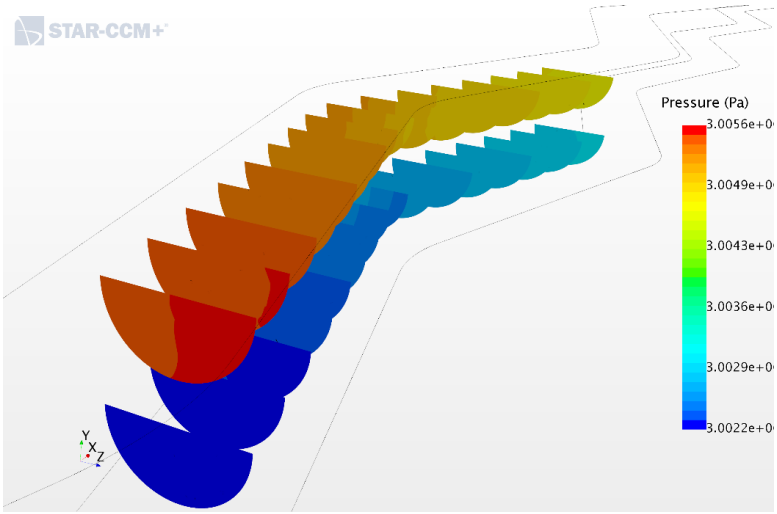

(a)

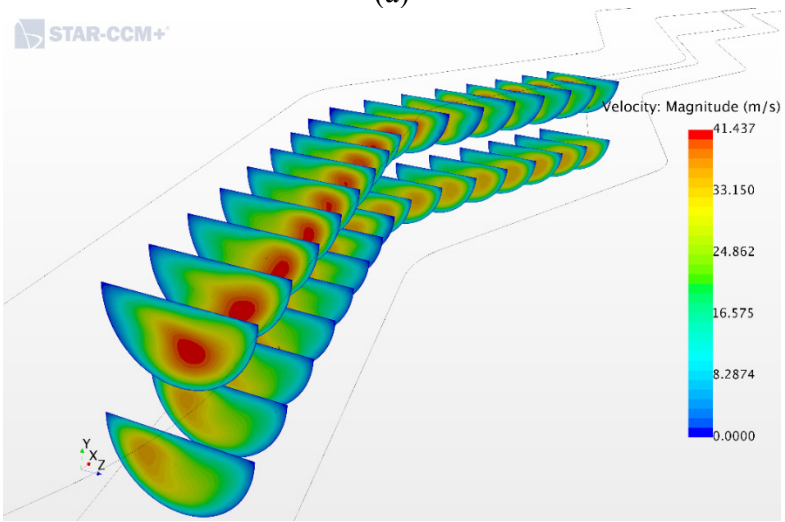

(b)

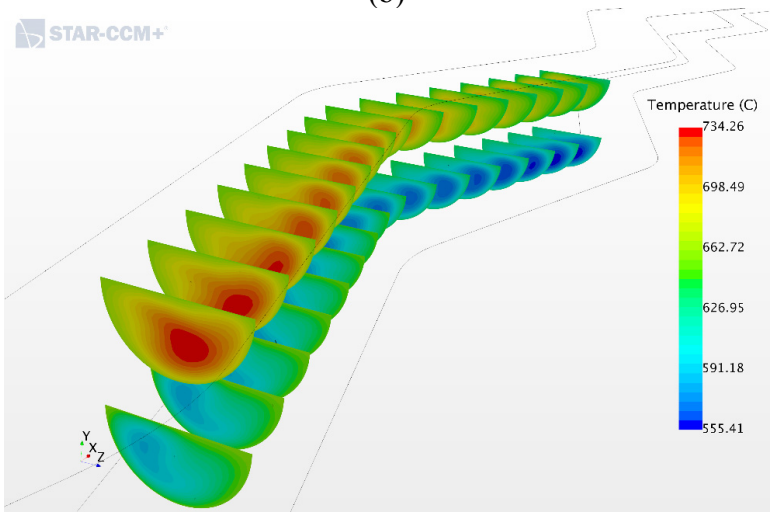

(c)

Figure 4-9. Contours of (a) pressure, (b) velocity magnitude, and (c) temperature.

Figure 4-10 shows the heat transfer coefficients on both the hot and cold sides. Compared to the cold side, higher velocities with larger thermal conductivities led to a higher average heat transfer coefficient on the hot side. The helium flow was interrupted from becoming fully-developed at each zigzag bend and thereby restarting the boundary layers, which increased the heat transfer coefficient. As shown in Figure 4-10, a peak in the heat transfer coefficient was presented in each zigzag bend unit that had a higher heat transfer coefficient than the other locations. This may result in a slightly wavy temperature distribution in the solid plate along the heat exchanger. It was observed that the highest heat transfer coefficients were at the inlets on both the hot and cold sides of the heat exchanger. This reflected, as also shown in Figure 4-6, that a smaller temperature difference between the fluid and metal wall presented near the inlet section of each side of the heat exchanger.

As the helium temperature decreased along the hot-side fluid flow direction, the overall trend of the heat flux decreased, except for the hot-side outlet due to the entrance effect of the cold-side inlet. It can be seen from Figure 4-11 that the heat fluxes on both heat exchanger terminals had large values since the thickness of boundary layers in the entrance regions was small. The effect of the bends on the heat flux was also displayed. It was shown that the heat flux had a substantially larger value in one bend unit while the smallest value also presented in the same unit. The change in the helium flow direction, as well as the local flow separation and enhanced flow mixing, resulting in higher heat transfer rate. The peak was not necessary right after a zigzag bend. In this flow condition and geometry, it presented near the center of the straight section.

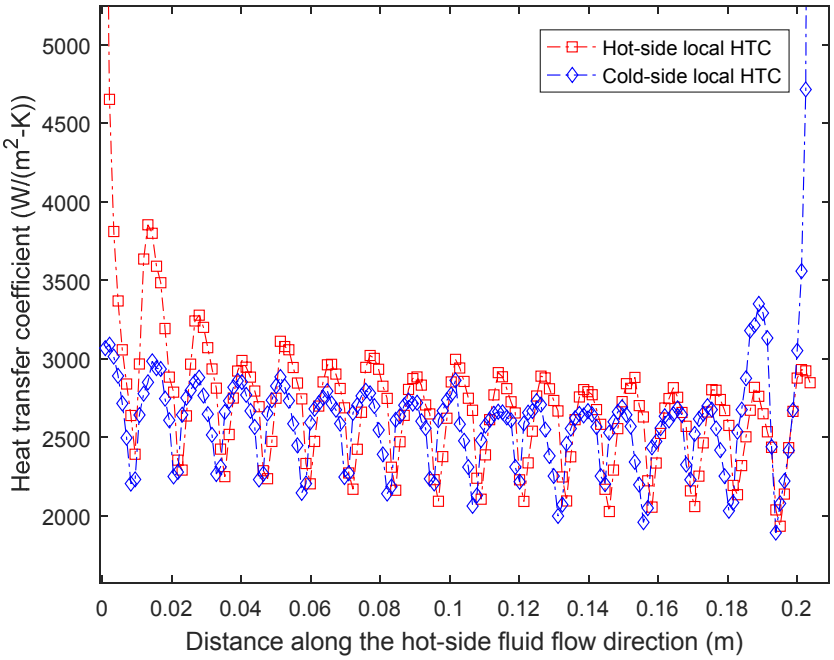

Figure 4-10. Local heat transfer coefficient distributions inside the heat exchanger from the STAR-CCM+ simulations.

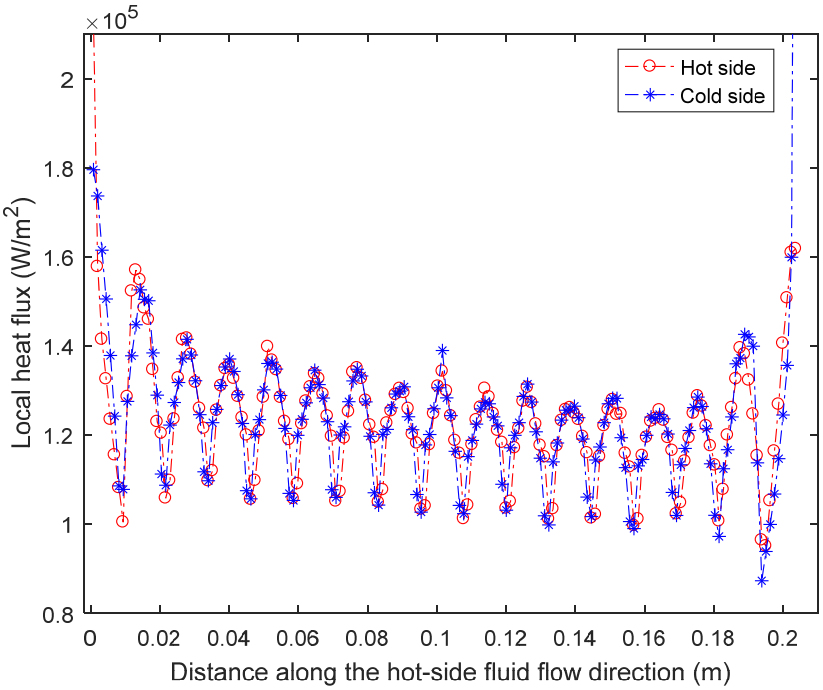

Figure 4-11. Local heat flux distributions inside the heat exchanger from the STAR-CCM+ simulations.

Figure 4-12 and Figure 4-13 present the local pressure loss factors and local Nusselt numbers inside the heat exchanger. The global pressure loss factors calculated by Equation (4.7) were 0.03696 and 0.03531 on the hot side and cold side, respectively. The mean pressure loss factors calculated by Equation (4.10) were 0.03581 and 0.03665 on the hot side and cold side, respectively. The pressure loss factor on the hot side was slightly greater than that on the cold side by approximately 3%. The global value could predict the mean value over the entire channel since the discrepancies between the mean and global values were about 3.5%. As can be seen from Figure 4-12, the peaks on both the hot and cold sides were shifted, which can be attributed to the location difference of the entrance region for a countercurrent flow heat exchanger configuration.

Similarly, the mean Nusselt numbers calculated from the heat transfer coefficients by Equation (4.13) were 11.66 and 12.34 for the hot side and cold side, respectively. The global Nusselt numbers obtained from the heat transfer coefficients by Equation (4.14) were 9.18 and 9.94 on the hot side and cold side, respectively. The mean Nusselt number on the hot side was greater than that on the cold side by approximately 6%. However, the Nusselt numbers obtained from the global heat transfer coefficients underestimated the mean values by 21.3 and 19.4% for the hot side and cold side, respectively. For laminar flows in a heat exchanger, the heat transfer correlation is a strong function of not only the flow passage geometry but also the thermal boundary condition. Also, different reference temperatures would give completely different Nusselt number values. Therefore, it should be cautious about the definition of heat transfer coefficient as well as the operation conditions when it comes to use the heat transfer correlations for the heat exchanger thermal design.

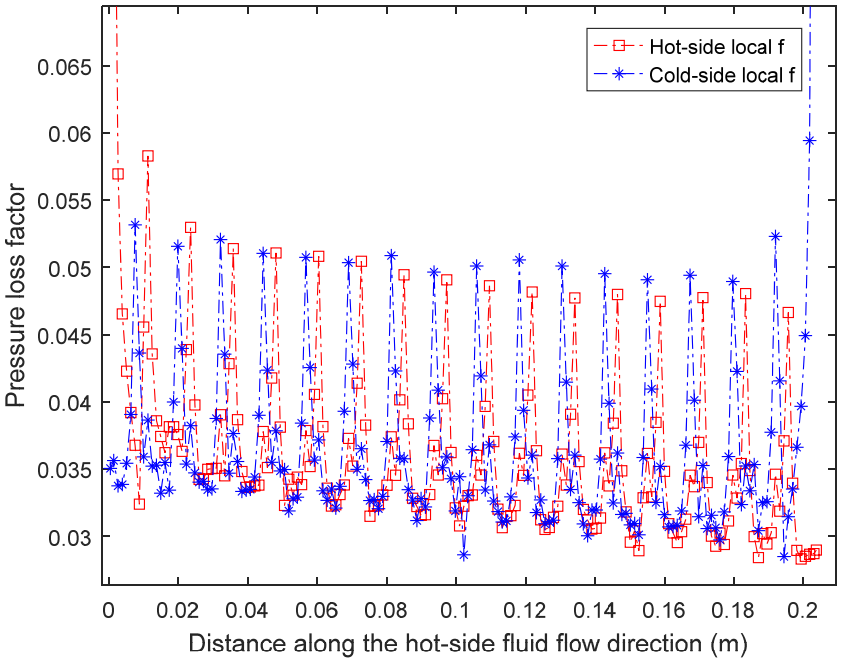

Figure 4-12. Local pressure loss factor inside the heat exchanger from the STAR-CCM+ simulations.

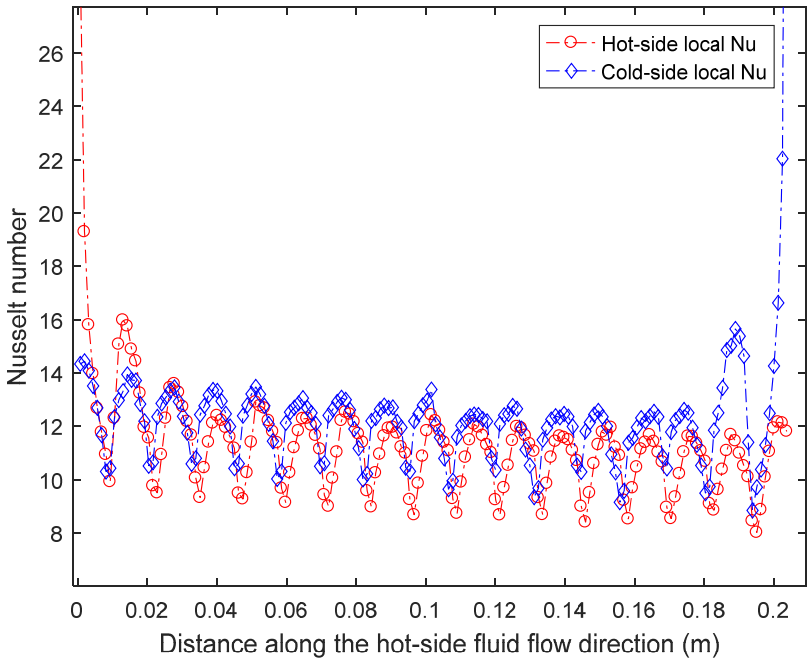

Figure 4-13. Local Nusselt number inside the heat exchanger from the STAR-CCM+ simulations.

4.4.2 Thermal boundary conditions

The Nusselt number is strongly dependent on the thermal boundary condition and flow passage geometry for laminar flows (Shah and Sekulic, 2003). Therefore, it is essential to examine thermal boundary conditions when the fluid flow in a heat exchanger is in the laminar flow regime. Three important thermal boundary conditions for heat exchangers are: (1) constant wall temperature, both axially and peripherally throughout the passage length; (2) constant wall heat transfer rate in the axial direction and constant wall temperature at any axial location in the peripheral direction; and (3) constant wall heat transfer rate in the axial direction as well as in the peripheral direction. The simplified heat exchanger simulation model was divided into eight segments along the flow channels to identify the thermal boundary conditions for the zigzag-channel PCHE. The schematic of the divided model is shown in Figure 4-14. The temperature and heat flux distributions along the helium flow direction for each segment can be obtained. Since the geometry is symmetrical with respect to the vertical plane passing through the two circle centers, the results for only the first four segments (i.e., h1, h2, h3, h4, c1, c2, c3, and c4) are presented. It can be seen from Figure 4-15 and Figure 4-16, the temperature distribution was not constant in the peripheral direction of a channel cross section. The temperatures on the top flat wall were smaller than these on the bottom curved (circular) wall on the hot side. The temperatures on the top flat walls of the heat exchanger cold side are larger than those on the bottom curved wall on the cold side, opposite to the hot side.

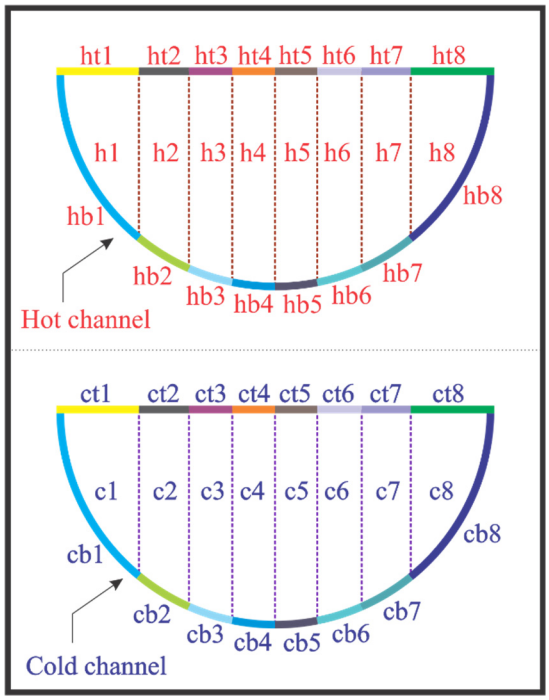

Figure 4-14. Schematic of the divided geometry model and the associated notations.

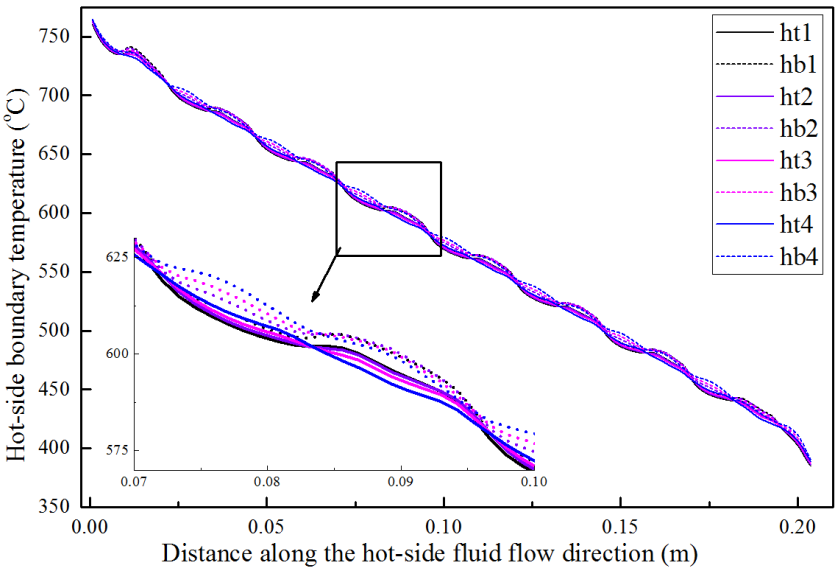

Figure 4-15. Hot-side boundary temperature distributions on the first four segment walls.

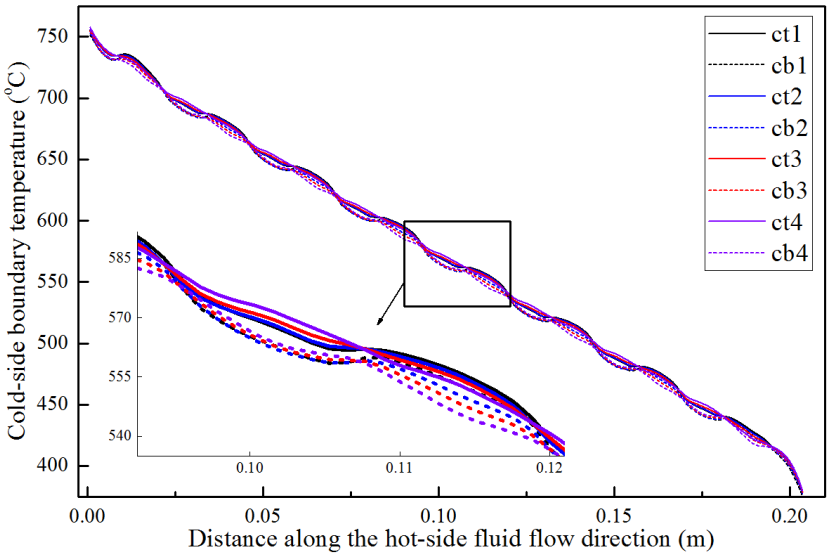

Figure 4-16. Cold-side boundary temperature distributions on the first four segment walls.

The heat flux boundary conditions are also shown in Figure 4-17 and Figure 4-18. The heat flux distributions on different segments were significantly different. However, the trend of heat flux for each segment along the helium flow direction was similar. The largest values were observed on every other bends for the first four segments while the smallest values on the straight parts of the zigzag bends. It will be expected that the largest values will also show on the other bends for the rest four heat exchanger segments, resulting in higher heat flux values right after each of the bends in the zigzag channels. The actual thermal boundary conditions did not correspond to any of the three idealized boundary conditions described above. Hence, the existing correlations in the literature may not reflect the actual heat transfer conditions in our experiments. Therefore, the discrepancies between the experimental data and the CFD simulation results may be caused by, in addition to the variations in the geometrical parameters due to chemically etching and diffusion bonding, the different thermal boundary conditions since the thermal boundary conditions of the zigzag channels in experiments are much more complex than these in the numerical simulations, considering the thermal insulation and flow fluctuations. Figure 4-19 and Figure 4-20 present the

helium temperature distributions for each segment on the hot side and cold side, respectively. As can be seen, the helium temperature distribution for each segment presented a wavy shape. However, the fluid bulk temperature distributions along the entire channel length were approximately linear.

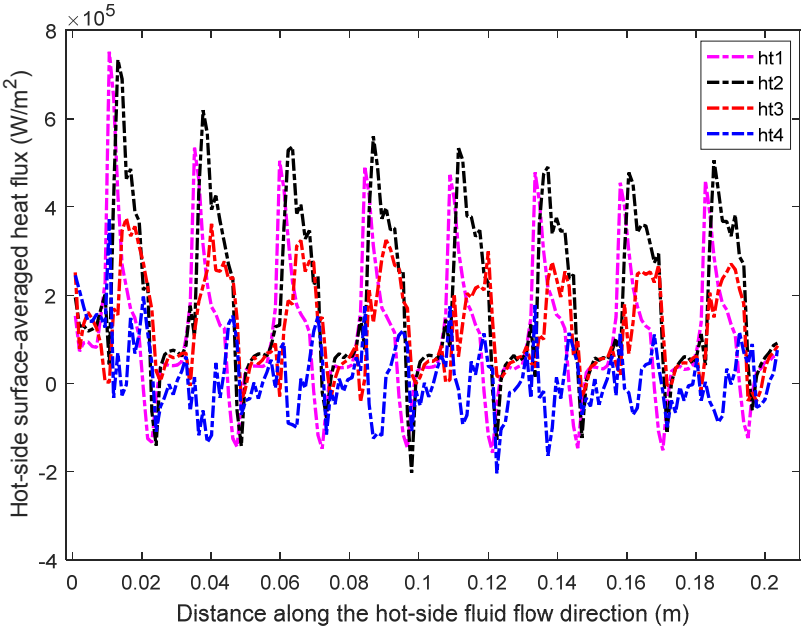

Figure 4-17. Hot-side surface-averaged heat flux distributions on the first four segment walls.

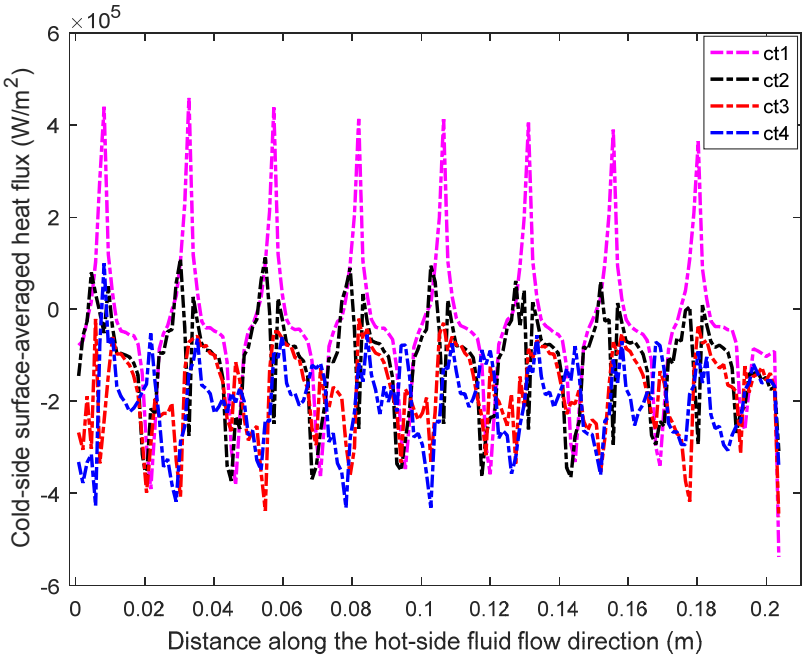

Figure 4-18. Cold-side surface-averaged heat flux distributions on the first four segment walls.

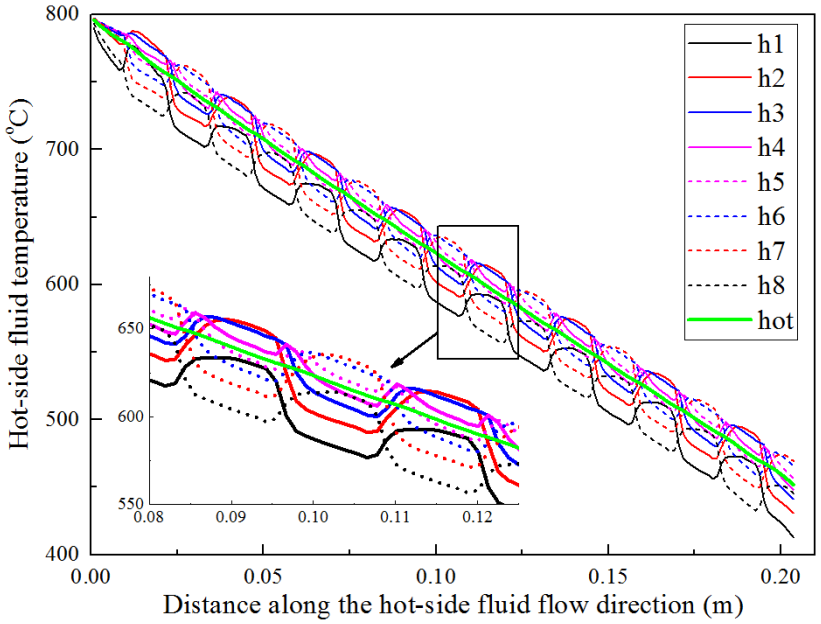

Figure 4-19. Hot-side helium temperature distributions on each heat exchanger segment along the PCHE length.

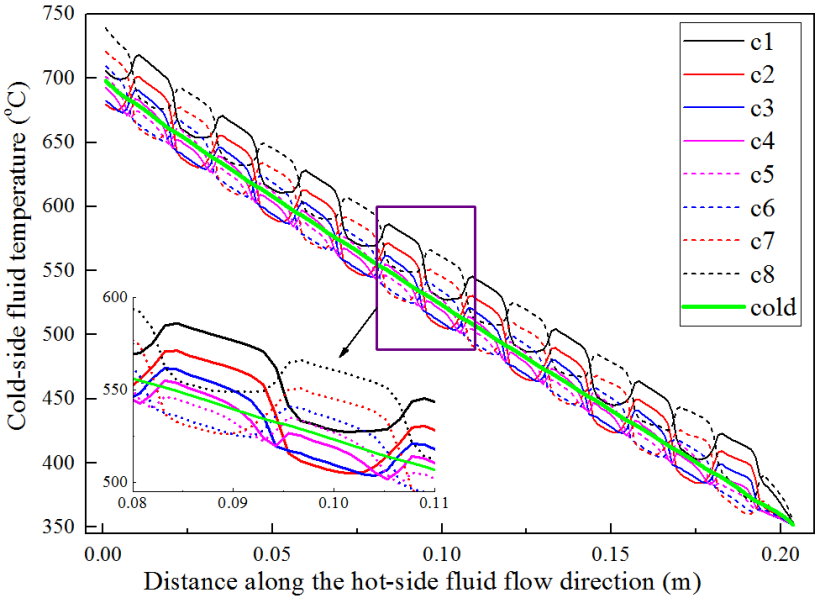

Figure 4-20. Cold-side helium temperature distributions on each heat exchanger segment along the PCHE length.

4.4.3 Effect of the variation of the fluid and solid thermophysical properties

The effect of the variation of the fluid and solid thermophysical properties was studied for a flow condition of the helium pressure of 3.0 MPa, hot-side helium inlet temperature of 800 °C, and cold-side helium inlet temperature of 350 °C. A simulation with constant fluid and solid properties was also carried out for this flow condition using the same mass flow rates as the previous simulation, i.e., 5.108×10^{-5} kg/s. Table 4-3 shows the result comparisons between these two simulation cases. As illustrated, the variation in the fluid properties could affect the pressure drop and heat transfer in a heat exchanger. Heat is transferred from hot helium to the metal wall on the hot side, which sets up a temperature gradient in the radial direction in the helium at a cross section. Helium has higher temperature near the channel centerline and lower temperature near the wall. Since the gas viscosity decreases with decreasing temperature, helium near the wall has a smaller

viscosity than that near the channel centerline. Compared to the simulation with constant properties, helium near the wall shall have a larger velocity to satisfy the mass conservation. The decrease in gas viscosity near the wall yields lower friction factor and lower pressure loss. The increased velocity near the wall may lead to a more efficient convection heat transfer process, resulting in higher heat transfer coefficient. Vice versa, a higher friction factor and lower heat transfer coefficient are expected on the cold side. However, it should be emphasized that the variation in viscosity for helium gas may also depend on the channel cross-sectional shape, surface interruptions, developing flows and thermal boundary conditions. As can be seen from Table 4-3, compared with the simulation with temperature-dependent fluid properties, the pressure drop factors in the simulation with constant fluid and solid properties were slightly lower on the cold side but higher on the hot side. However, the mean Nusselt numbers for the simulation with constant properties were about 23.60 and 25.93% lower on the hot side and cold side, respectively. This was mainly attributed to the complex thermal boundary conditions as described in the previous section and the channel shape that led to multiple developing flows inside the heat exchanger.

Table 4-3. Comparison of the simulation results between the temperature-dependent and constant fluid and solid properties.

	Temperature-dependent properties	Constant properties	Relative difference (%)
Mean Nu on hot side	11.66	8.908	-23.60
Mean Nu on cold side	12.34	9.142	-25.93
Mean pressure loss factor on hot side	0.0358	0.0373	4.2
Mean pressure loss factor on cold side	0.0366	0.0351	-4.0

The second case is to study the thermal-hydraulic performance with a different gas. The simulation was carried out using nitrogen gas with the same Reynolds number as the helium gas at both the hot-side and cold-side inlets. The result comparison is listed in Table 4-4 and the discrepancies between the two simulations were less than 1.5%. It was expected since the Prandtl numbers of both gases were similar.

Table 4-4. Comparison of the simulation results using helium and nitrogen gases.

	Helium gas	Nitrogen gas	Relative difference (%)
Mean Nu on hot side	11.66	11.70	0.36
Mean Nu on cold side	12.34	12.51	1.33
Mean pressure loss factor on hot side	0.0358	0.0360	0.50
Mean pressure loss factor on cold side	0.0366	0.0364	-0.68

4.4.4 Effect of the radiuses of curvature at zigzag bends

A roundness was introduced at the tip of each bend in the zigzag flow channels of the fabricated PCHE. Simulations were conducted to study the performance of a simplified PCHE model with sharp bends (i.e. with a zero radius of curvature for the sharp bends) as well as a radius of curvature of 8 mm in the flow channels. The base case is the simplified model with a radius of curvature of 4 mm. Table 4-5 shows comparisons of the mean pressure loss factor and the mean Nusselt number between the zigzag channels with the rounded and sharp bends. ε_1 and ε_2 indicated the deviation percentage from the base case. Both the mean pressure loss factors and mean Nusselt numbers in the zigzag channel with sharp bends were larger than those in the zigzag channels with rounded

bends. It was expected since the flow condition in the flow channels with sharp bends was more chaotic than that in the channels with rounded bends, resulting in enhancing the heat transfer but enlarging the pressure loss. Increasing the radius of curvature from 4 to 8 mm reduced the pressure loss factor by approximately 5.61 and 5.32% on the hot side and cold side, respectively. However, the Nusselt numbers on the hot side and cold side were also reduced by about 4.99 and 4.72%, respectively. Whether it is worth introducing a radius of curvature to the bends is based on multiple factors, such as the capital cost, heat exchanger effectiveness, entire system efficiency. For the case studied, the goodness of the heat exchanger was not varied considerably by increasing the radius of curvature from 4 to 8 mm.

Table 4-5. Comparison of simulation results with the different radiuses of curvature in zigzag-channel bends.

	Base case R = 4 (mm)	R = 8 (mm)	ε_1 (%)	R = 0 (mm)	ε_2 (%)
Mean Nu on hot side	11.66	11.08	-4.99	12.09	3.66
Mean Nu on cold side	12.34	11.76	-4.72	12.77	3.46
Mean pressure loss factor on hot side	0.0358	0.0338	-5.61	0.038	6.33
Mean pressure loss factor on cold side	0.0366	0.0347	-5.32	0.039	5.88

4.4.5 Effect of different channel configurations

The effect of different channel configurations was examined over five different channel arrangements that are shown in Figure 4-21. Type a is the base case that was used for the simulations in the previous sections while the heat exchanger flow length was reduced to half of

the previous simulation model. Simulations were conducted on three mass flow rates in the laminar flow regime with only effectiveness compared and the results are listed in Table 4-6. It was observed that types a and e had the two smallest effectiveness' when compared with the other three types.

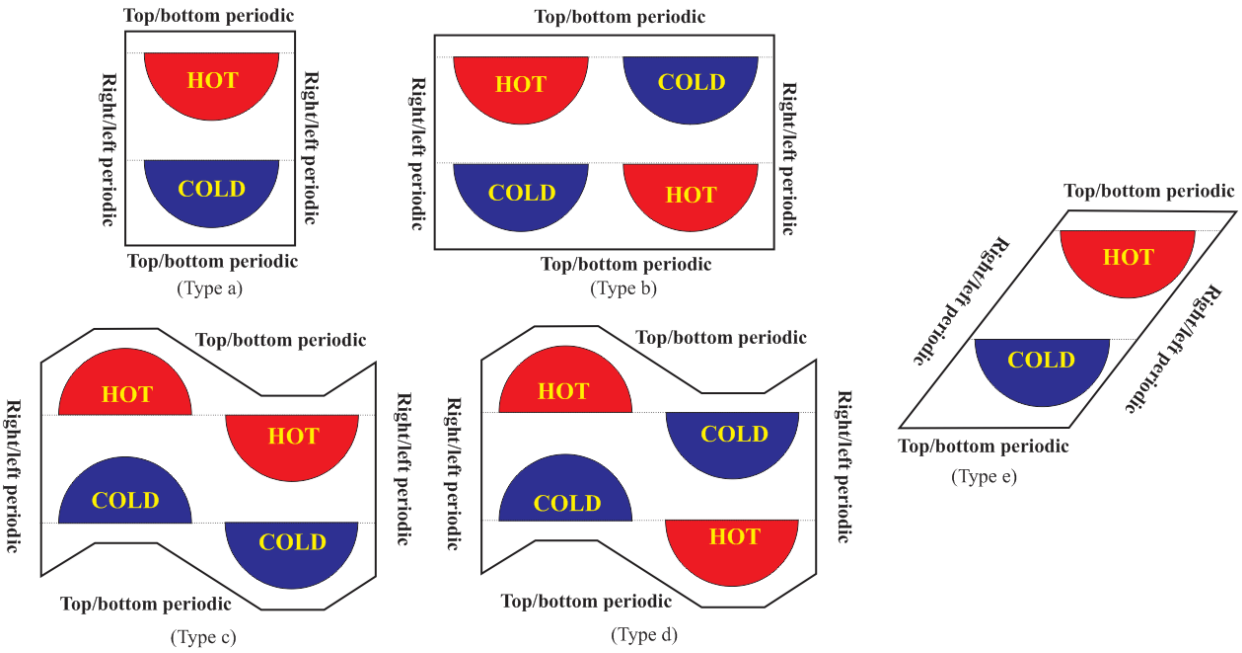

Figure 4-21. Schematic of the five different channel configurations.

Table 4-6. Comparison of heat exchanger effectiveness for the five different channel configurations.

Mass flow rate (kg/s)	Effectiveness (%)				
	Type a	Type b	Type c	Type d	Type e
4.00×10^{-5}	70.73	71.11	71.04	71.02	70.84
6.00×10^{-5}	65.08	65.84	66.09	66.04	65.80
8.00×10^{-5}	60.76	61.80	62.13	62.11	61.76

4.4.6 Effect of different channel pitch lengths and zigzag angles

The author participated in conducting a comprehensive numerical study on friction factor and heat transfer for zigzag-channel PCHEs with various geometric parameters at Idaho National Laboratory (Yoon et al., 2017). General explicit correlations, Equations (4.17), (4.18) and (4.19), for both friction factor and Nusselt number as a function of geometric parameters were developed from extensive CFD analysis database. These correlations allow for accurate determination of the thermal-hydraulic performance and effectiveness. The effects of channel pitch lengths and zigzag angles are analyzed based on the obtained numerical correlations. As shown in Figure 4-22, both friction factor and Nusselt number decreased as channel pitch lengths increased when the zigzag angle was fixed at 15°. It was expected since the extent of entrance effects per unit length was reduced as the channel pitch length was increased, resulting in smaller friction factors and Nusselt numbers. Also, as zigzag angles increased, both friction factors and Nusselt number increased. However, it can be seen from Figure 4-23 that there was not significant gain in the Nusselt numbers when the zigzag pitch angles were greater than 35 degrees. Therefore, further increasing the zigzag angle is not recommended.

$$f = \frac{15.78}{\mathrm{Re}} + \frac{6.7268}{1000}\exp\left(6.6705\alpha\right)\left(\frac{l_R}{D_h}\right)^{-2.3833\alpha+0.26648} + \frac{4.3551\alpha - 1.0814}{100} \tag{4.17}$$

$$\mathrm{Nu}_h = \left(0.71\alpha + 0.289\right)\left(\frac{l_R}{D_h}\right)^{-0.087} \mathrm{Re}^{-0.11\left(\alpha-0.55\right)^2-0.004\left(\frac{l_R}{D_h}\right)\alpha+0.54} \mathrm{Pr}^{0.56} \tag{4.18}$$

$$\mathrm{Nu}_c = \left(0.18\alpha + 0.457\right)\left(\frac{l_R}{D_h}\right)^{-0.038} \mathrm{Re}^{-0.23\left(\alpha-0.74\right)^2-0.004\left(\frac{l_R}{D_h}\right)\alpha+0.56} \mathrm{Pr}^{0.58} \tag{4.19}$$

The applicable range for the above correlations is:

$$200 \le \mathrm{Re} \le 2,000$$
$$5^{\circ} \le \alpha \le 45^{\circ} \quad .$$
$$4.09 \le \frac{l_R}{D_h} \le 12.27$$

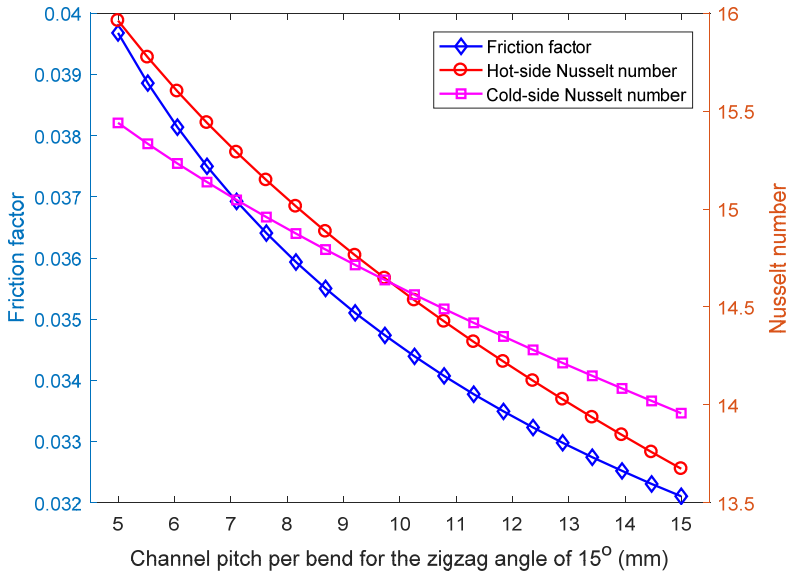

Figure 4-22. Effect of channel pitch lengths on friction factors and Nusselt numbers.

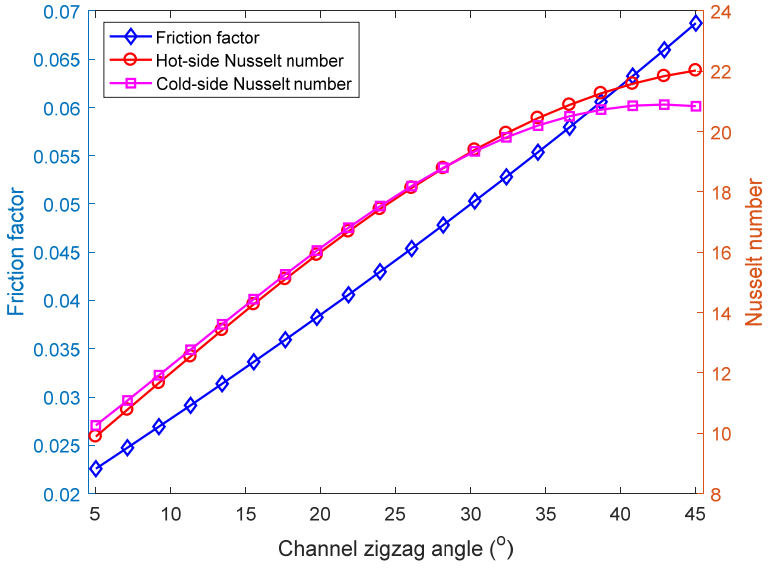

Figure 4-23. Effect of channel zigzag angles on friction factors and Nusselt numbers.

4.5 Optimization of the PCHE Channel Geometry

Optimization of PCHE channel geometry is generally based on the maximization of heat transfer and minimization of pressure drop. Pressure drop and heat transfer characteristics heavily depend on the PCHE flow channel geometry and operation condition. Increasing heat transfer could reduce the heat transfer area of the heat exchanger and hence the size of the heat exchanger. Decreasing pressure drop could reduce the required pump power for operation. Generally, reducing the size of a heat exchanger could increase the pressure drop. Therefore, the heat transfer and pressure drop are two conflicting objectives. An approach of multi-objective optimization was used to determine a Pareto optimal solution set that the solutions were non-dominated with respect to each other. Based on the Nusselt number and Fanning friction factor correlations, Equations (4.17) and (4.18), Non-dominated Sorting Genetic Algorithms (NSGA-II) was utilized to optimize the problem. NSGA-II was run for a population size of 6,000, where 20 in Reynolds numbers, 20 in zigzag angles, and 15 in aspect ratios. Note that calculations for all populations were within the applicable range of the correlations. The first generation and the Pareto front were obtained. The total number of the points on the Pareto front or the non-dominated solutions is 142 and all points are presented in Figure 4-24. The manufacturers and users can select the optimal geometrical parameters for the zigzag-channel PCHE designs per their considerations.

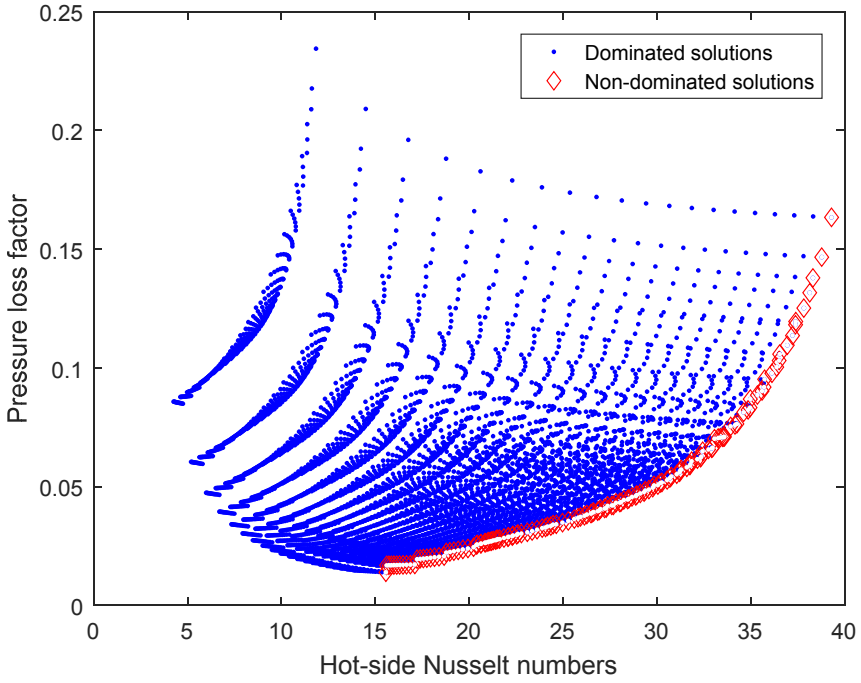

Figure 4-24. Pareto front for the pressure loss factor and hot-side Nusselt number.

4.6 Stress Field Simulation

Although PCHEs offer significant improvement in heat exchanger compactness, therefore size, and effectiveness, there are valid concerns regarding the integrity of PCHEs during their lifetime of service. Thermal stress simulations incorporated with conjugate heat transfer was performed using the one-way fluid-structure interaction models in STAR-CCM+. The thermal stress analysis was performed for a simplified 3-D model. Alloy 617 is one of the primary structural materials for PCHEs. The basic thermophysical and mechanical properties of Alloy 617 are shown in Table 4-1 and Table 4-7, respectively. The thermophysical properties were fitted into functions that were implemented into STAR-CCM+ and the mechanical properties were imported as field functions.

Table 4-7. Alloy 617 mechanical properties (ASME, 2015).

Temperature, K	Young's modulus, Pa	Thermal expansion coefficient, 1/K
298.15	2.01×10^{11}	1.09×10^{-5}
373.15	1.96×10^{11}	1.16×10^{-5}
423.15	1.93×10^{11}	1.21×10^{-5}
473.15	1.91×10^{11}	1.26×10^{-5}
523.15	1.89×10^{11}	1.30×10^{-5}
573.15	1.87×10^{11}	1.33×10^{-5}
623.15	1.84×10^{11}	1.35×10^{-5}
673.15	1.81×10^{11}	1.36×10^{-5}
723.15	1.78×10^{11}	1.37×10^{-5}
773.15	1.74×10^{11}	1.38×10^{-5}
823.15	1.71×10^{11}	1.38×10^{-5}
873.15	1.67×10^{11}	1.40×10^{-5}
923.15	1.64×10^{11}	1.42×10^{-5}
973.15	1.60×10^{11}	1.45×10^{-5}
1,023.15	1.56×10^{11}	1.49×10^{-5}
1,073.15	1.52×10^{11}	1.54×10^{-5}
1,123.15	1.46×10^{11}	1.59×10^{-5}

Simulating the entire channel length requires extreme computational resources. Therefore, the flow length was set to 10 mm, which is about the length of one zigzag bend. The hot-side and cold-side helium inlet temperatures were set to 800 and 780 °C, respectively, and the helium mass flow rate in each channel was 5.108×10^{-5} kg/s. The helium outlet pressures for both sides were 3.0 MPa. For solid displacement solution, it is required to limit the rigid body motion. Three fixed points were put on the back-wall corners to constrain the rigid body motion. The steady-state temperature distributions were obtained first by finite-volume conjugate heat transfer simulations. Figure 4-25 shows the solid temperature distributions of the simplified model. As can be seen, the temperature variations of the entire channel were less than 10 °C.

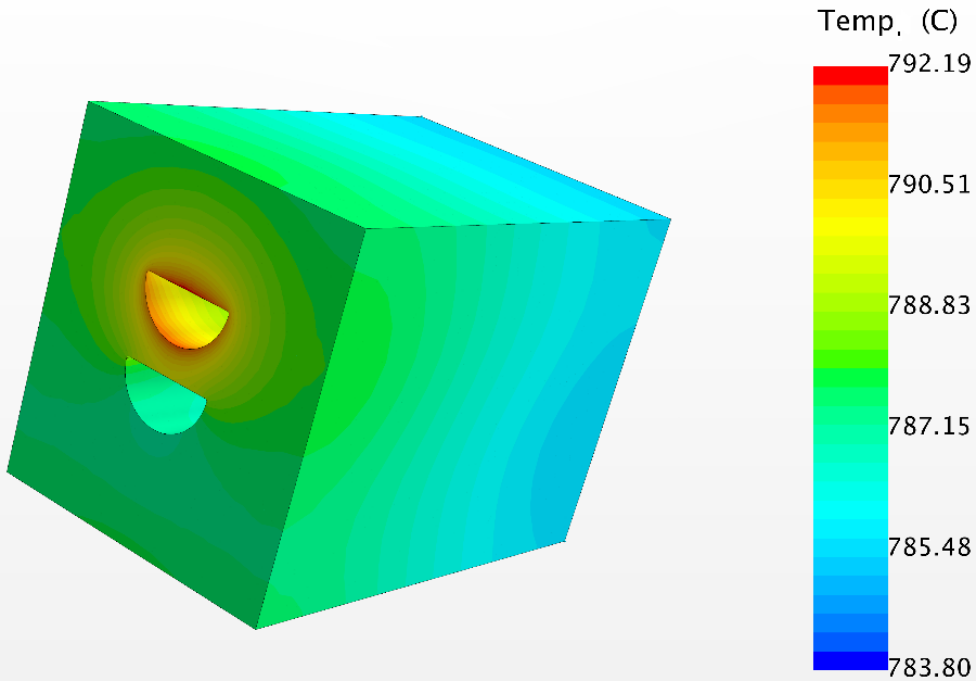

Figure 4-25. Temperature distributions in the solid of the simplified geometry.

The temperature data as well as the fluid pressures were mapped into a finite element model of the simulated model for the stress analysis. The channel's sharp corners need to be carefully considered when performing stress modeling since the maximum stress presents on the corner. It leads to infinite solution if the linear elastic model is used at the sharp corners, which does not reflect the reality. Therefore, a roundness of 0.02 mm in radius was introduced into all the corners to avoid diverging stress by the linear-elastic solver. This is reasonable since diffusion bonding could cause roundness at the corners. A local surface meshing scheme was used at all corners. The tetrahedral mesh and mesh refinement at corners are shown in Figure 4-26.

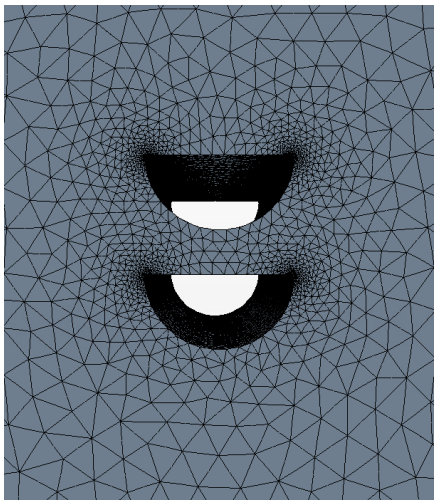

Figure 4-26. An image showing the tetrahedral mesh and mesh refinement at corners.

Three-dimensional solid stress with linear isotropic elastic model was used to obtain the stress field for the simplified geometry, which is shown in Figure 4-27. The largest stress is about 28.3 MPa, which is less than the allowable stress of Alloy 617 at 800 °C (i.e., 31.3 MPa). It was expected that the highest stress occurred at corners on both the hot and cold channels. Figure 4-28 shows an image of the stress concentration at the rounded corners. It was observed that the stress at the corners was much larger than that on other regions.

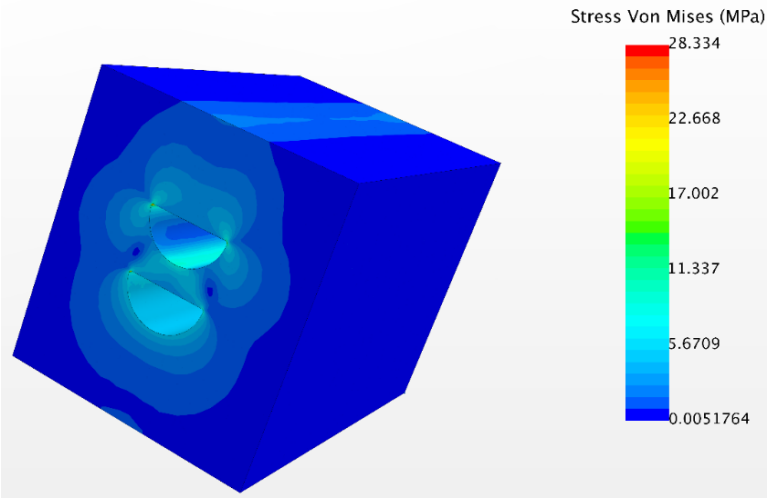

Figure 4-27. Stress field of the middle plane of the simplified geometry.

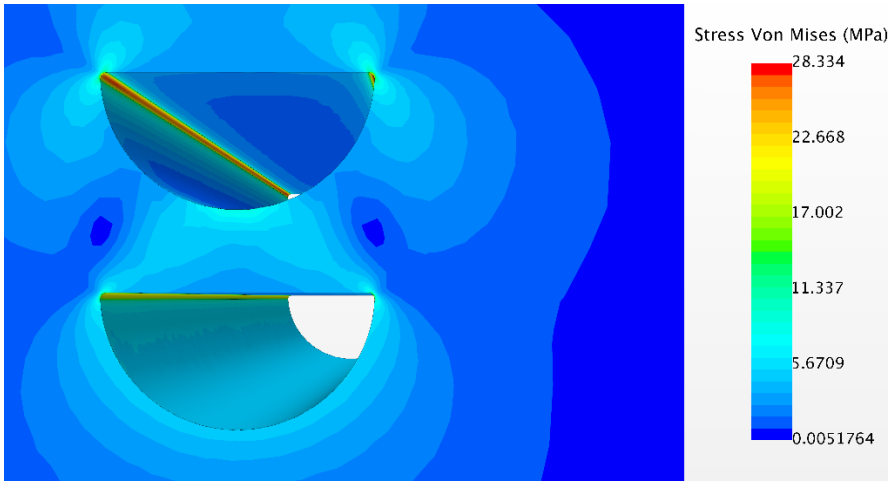

Figure 4-28. An image showing the stress concentration at the rounded corners.

4.7 Conclusion

In this chapter, a three-dimensional CFD study on a simplified geometry model for the fabricated zigzag-channel PCHE was carried out. Comparisons of the numerical results with experimental data showed some discrepancies in the channel Nusselt number and pressure loss factor, which could be attributed to the lack of the detailed geometrical measurements of the flow channels in the PCHE after the diffusion bonding process, the omission of the heat loss to the surroundings from the heat exchanger surfaces in the simulations, and different thermal boundary conditions used in the simulations. Local thermal-hydraulic performance analyses indicated that a fully-developed flow condition was never observed in the zigzag channels. This is mainly due to the nature of zigzag channel, leading to periodic flow disturbance at each bend. Several effects on the thermal-hydraulic performance of the PCHE were studied, including the fluid and solid thermophysical properties, radiuses of curvature at zigzag bends, channel configurations, and channel pitch lengths and zigzag angles. In addition, the simplified heat exchanger simulation model was divided into eight segments to identify the thermal boundary conditions for the zigzag-

channel PCHE. The wall temperature and heat flux distributions along the helium flow direction in the heat exchanger for each segment were obtained. It was observed that the wall temperatures were not constant along the azimuthal direction of a channel cross section. In addition, the helium temperature distribution for each segment presented a wavy shape. However, the global helium temperature distributions along the entire channels were approximately linear. For the heat flux distributions, although they were significantly different on different segment walls, the heat flux for each segment along the fluid flow direction was similar. Furthermore, a multi-objective optimization for the PCHE geometry was also performed based on the numerical correlations. A total number of 142 points on the Pareto front were obtained. The manufacturers and users can select the optimal geometrical parameters of the zigzag-channel PCHE designs from the obtained Pareto front per their considerations. Finally, the stress field of a simplified geometry was obtained. It was observed that the highest stress occurred at corners and that it was less than the maximum allowable stress of the structural material.

Chapter 5 Dynamic Behavior of PCHEs

5.1 Overview

Understanding dynamic behavior is of importance in IHX design for advanced nuclear reactors since some transients in the primary system may lead to accidents and the dynamic behavior of IHXs plays a key role in accident progression. It is therefore essential to understand how an IHX will dynamically respond to transients. In this chapter, dynamic behaviors introduced by variations of the fluid mass flow rate and temperature on both the hot and cold sides of straight-channel and zigzag-channel PCHEs are numerically investigated. The dynamic model used for both PCHEs is verified using a commercial software. Comparisons between the numerical results and the experimental data are carried out to assess feasibility of the dynamic model.

5.2 Steady-State Thermal Performance of the Straight-Channel PCHE

5.2.1 Straight-channel PCHE description

Two reduced-scale straight-channel PCHEs were fabricated using 1.6-mm thick Alloy 617 plates for the heat exchanger core. The headers of both PCHEs were made of Alloy 800H. For each of the PCHEs, a total of 10 hot plates and 10 cold plates were diffusion bonded together to form a metal block with 12 straight channels in each plate (Mylavarapu, 2011). Figure 5-1 shows one hot-

side plate and one cold-side plate and Table 5-1 lists the basic geometric parameters of the fabricated PCHEs. The cross-sectional shape of the straight flow channel is approximately semicircular with a nominal diameter of approximately 2.0 mm and a pitch of 2.54 mm in the span-wise direction. The PCHE was designed in the way that each side could withstand a maximum pressure of 3.0 MPa for use in the HTHF. One of the actual PCHE assemblies with four headers is shown in Figure 5-2. The dimensions of the PCHE block are 305 mm in length by 102 mm in width by 73 mm in height.

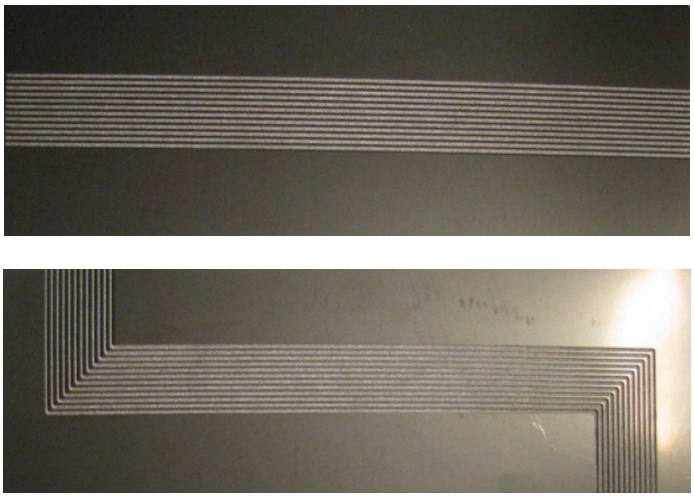

Figure 5-1. One cold-side plate (top) and one hot-side plate (bottom) (Mylavarapu, 2011).

Table 5-1. Summary of the straight-channel PCHE parameters (Mylavarapu, 2011).

Parameter	Hot side	Cold side
Channel pitch, mm	2.54	2.54
Channel width, mm	2.0	2.0
Plate thickness, mm	1.63	1.63
Channel travel length, mm	305	272
Number of plates	10	10
Number of channels in each plate	12	12

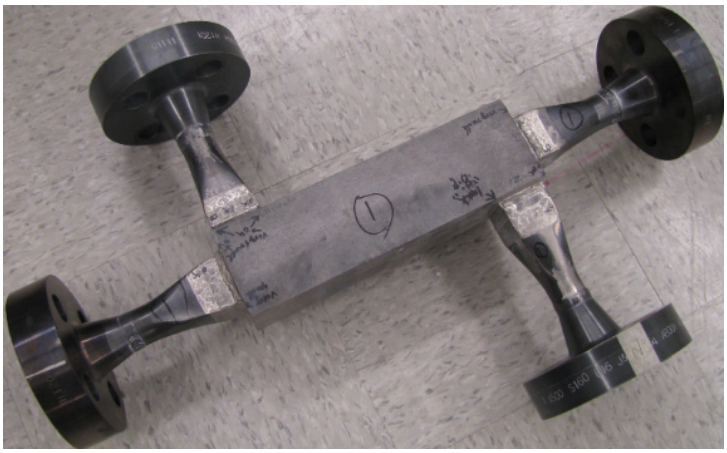

Figure 5-2. Straight-channel PCHE with four headers assembled (Mylavarapu, 2011).

5.2.2 Experimental procedures and test conditions

Thermal-hydraulic performance testing of the straight-channel PCHE was carried out. Figure 5-3 shows a total number of 91 experimental data points in terms of the helium mass flow rates, system pressures, and PCHE hot-side helium inlet temperatures. The helium mass flow rates were varied from 22 to 39 kg/h and the system pressures were raised to 2.7 MPa while the hot-side helium inlet temperatures were increased from 199 to 450 °C. The heat exchanger thermal duty at each steady state was calculated based on the average thermal duty on both the hot and cold sides, as shown in Figure 5-4 (a). The maximum heat exchanger thermal duty was about 8.5 kW among these test conditions. The heat loss from the heat exchanger surfaces is defined as the thermal duty difference between the hot side and cold side of the PCHE. It can be observed from Figure 5-4 (b) that the ratios of heat loss to the heat exchanger thermal duty were generally less than 15% except for about 10 runs.

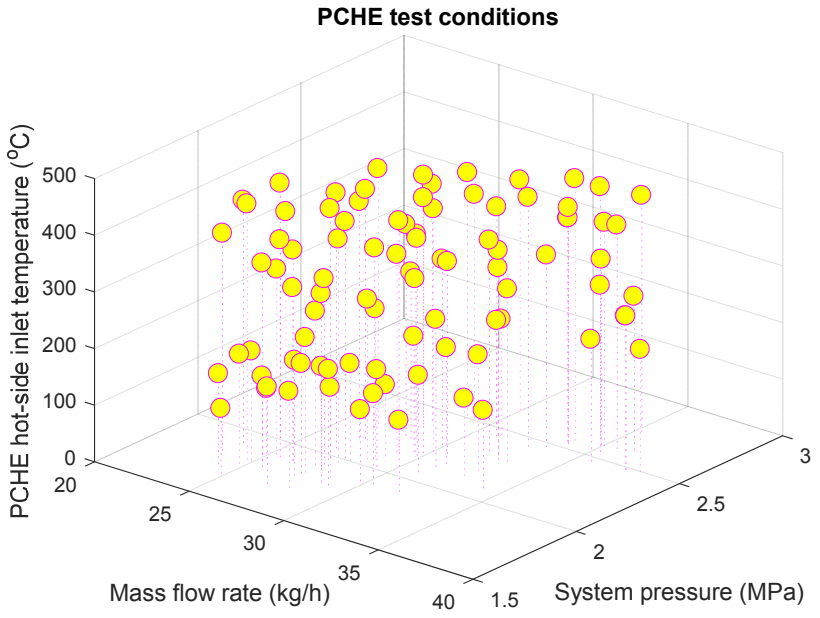

Figure 5-3. Test conditions for the straight-channel PCHE.

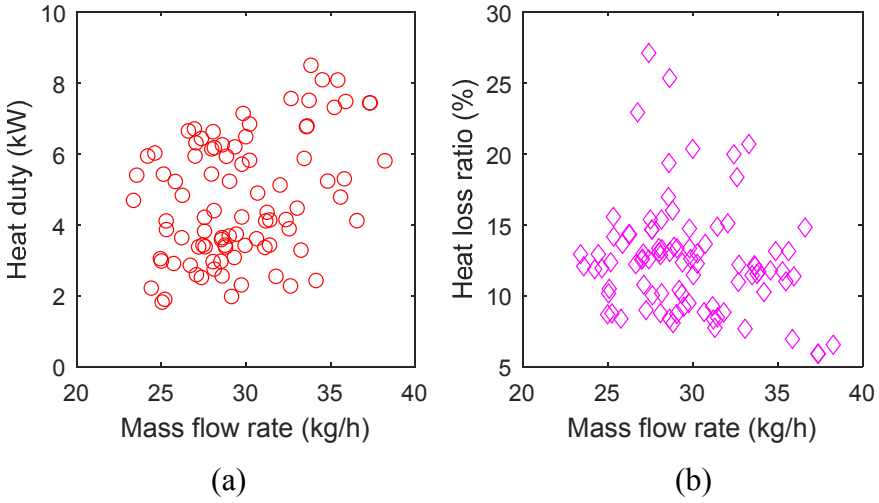

Figure 5-4. Straight-channel PCHE thermal duty and heat loss ratio.

5.2.3 Experimental data reduction method

As mentioned, no local internal fluid and wall temperature measurements were conducted in the present study. Therefore, the local and average convective heat transfer coefficients on both the hot and cold sides of the straight-channel PCHE cannot be obtained. However, with certain assumptions, the average heat transfer coefficients of the test heat exchanger can be estimated from the experimental data, including two helium inlet temperatures, two helium outlet temperatures, and two helium mass flow rates. Two typical methods, namely, a direct method and an indirect method, used to develop formulas for calculating the overall heat transfer coefficient of the PCHE, are discussed and compared in this section.

a. Direct method

To obtain the heat transfer coefficients of the test PCHE directly from the experimental data, four major assumptions were made: (1) Temperature distributions on both the hot and cold sides and solid plates were linear along the fluid flow direction inside the heat exchanger; (2) Heat transfer coefficients on both the hot and cold sides were the same for each steady-state condition (i.e., thermal resistances due to convection were approximately the same on both the hot and cold sides); (3) The effect of the flow and thermal entrance region was neglected; and (4) The thermal resistance due to the heat conduction in the solid plates was neglected.

The overall heat transfer coefficient is a function of the flow geometry, fluid properties, and solid plate material, which can be obtained from the experimental data. From the PCHE fabrication aspects, the hot-side heat transfer area, $A_{s,h}$, and the cold-side heat transfer area, $A_{s,c}$, are essentially the same (i.e., $A_{s,h} = A_{s,c} = A_s$). The overall thermal resistance can be expressed as,

$$\frac{1}{UA_s} = \frac{1}{h_h A_{s,h}} + \frac{1}{h_c A_{s,c}} + R_w \,. \tag{5.1}$$

Applying the aforementioned assumptions, the plate thermal resistance term R_w was neglected and the average convective heat transfer coefficient on either side can be estimated from experimental data as,

$$h_h = h_c = 2U \,. \tag{5.2}$$

b. Indirect method

The indirect method is same as the nonlinear regression method used to get the Nusselt number correlations for the zigzag-channel PCHE. Reader can refer to Chapter 3 for more detailed description.

5.2.4 Steady-state experimental data analysis and discussions

The Nusselt numbers for both the hot and cold sides using the direct method are plotted in Figure 5-5 with uncertainty bars representing the propagated errors. The largest uncertainty among all the data points was 13%. It was observed that the Nusselt numbers on the hot and cold sides follows the same trend well. There were some differences between the hot side and cold side, which can be attributed to the differences in the thermal conductivity of helium on both sides since the heat transfer coefficients were assumed the same for both sides.

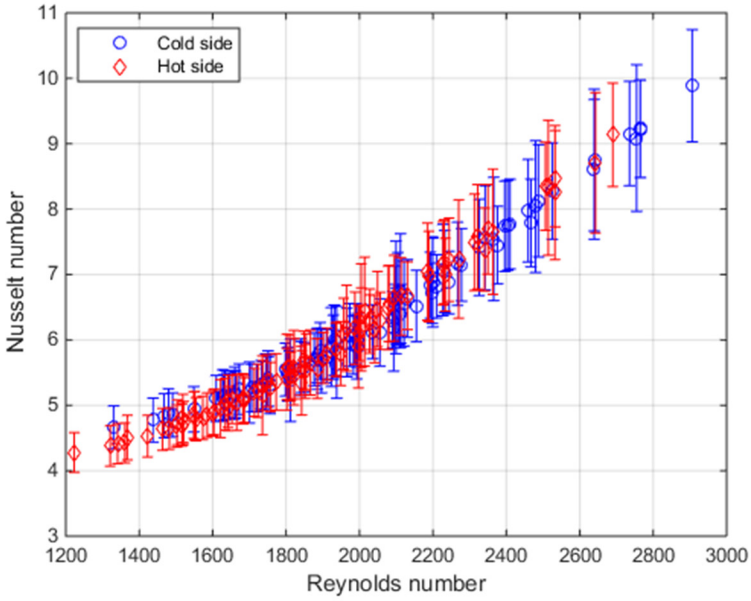

Figure 5-5. Nusselt numbers on both the hot and cold sides using the direct method.

It can be seen from Figure 5-5 that the Reynolds number were varied from 1,200 to 2,900, covering the laminar flow and laminar-to-turbulence flow transition regimes. The trend of the Nusselt number indicated that a change in the Reynold number between 1,800 and 2,000. To find the best fit correlations for the Nusselt numbers, two correlations were fit for the two regimes. Residuals of the correlations were calculated based on the root-sum-squared formula. Figure 5-6 shows the residuals plotted against the critical Reynolds numbers that presumably separate the two regimes. It was evident that the minimum residual occurred at the Reynolds number of about 1,850. Therefore, it appears reasonable to assume that the critical Reynold number was approximately 1,850. For the PCHE used in the helium-helium conditions, the Nusselt number is essentially a power function of the Reynolds number only. The best fit correlations for the total 182 data points on both the hot and cold sides with the critical Reynold number of 1,850 were proposed as,

$$\mathrm{Nu} = \begin{cases} \left(0.01352 \pm 0.0094\right)\mathrm{Re}^{\left(0.80058 \pm 0.0921\right)} & 1{,}200 \le \mathrm{Re} \le 1{,}850 \\ \left(3.6361 \times 10^{-4} \pm 7.855 \times 10^{-5}\right)\mathrm{Re}^{\left(1.2804 \pm 0.0273\right)} & 1{,}850 < \mathrm{Re} \le 2{,}900 \end{cases}. \quad (5.3)$$

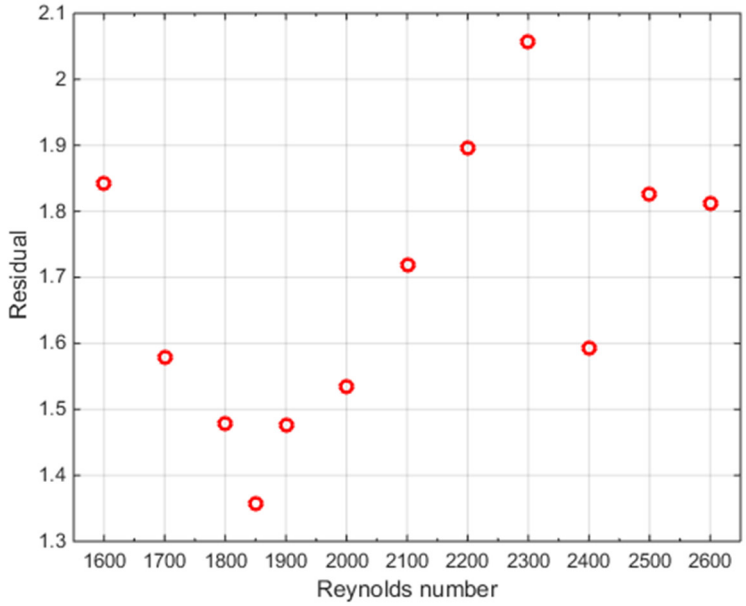

Figure 5-6. Residuals of fitted functions with different onset points.

Next, for the indirect method, validation for a fit correlation was considered in the data reduction process. The correlation was obtained via a nonlinear regression method using 76 data sets randomly selected from the total 91 data sets. The other 15 data sets were reserved for validating the fit correlation. Following the heat transfer data reduction method illustrated in Chapter 3, the fit correlation was obtained as,

$$\mathrm{Nu} = \begin{cases} \left(0.047516 \pm 0.015662\right)\mathrm{Re}^{\left(0.633151 \pm 0.044606\right)} & 1{,}200 \le \mathrm{Re} \le 1{,}850 \\ \left(3.680123 \times 10^{-4} \pm 1.184389 \times 10^{-4}\right)\mathrm{Re}^{\left(1.282182 \pm 0.042068\right)} & 1{,}850 < \mathrm{Re} \le 2{,}900 \end{cases}. \quad (5.4)$$

Both of the coefficients in Equations (5.3) and (5.4) included confidence intervals with a confidence level of 95%. A comparison of the results obtained from the direct and indirect methods is shown in Figure 5-7. The Nusselt numbers obtained from the nonlinear regression method were slightly larger than those obtained from the direct method. The largest deviation was 6.5% occurred at the lowest Reynolds number point.

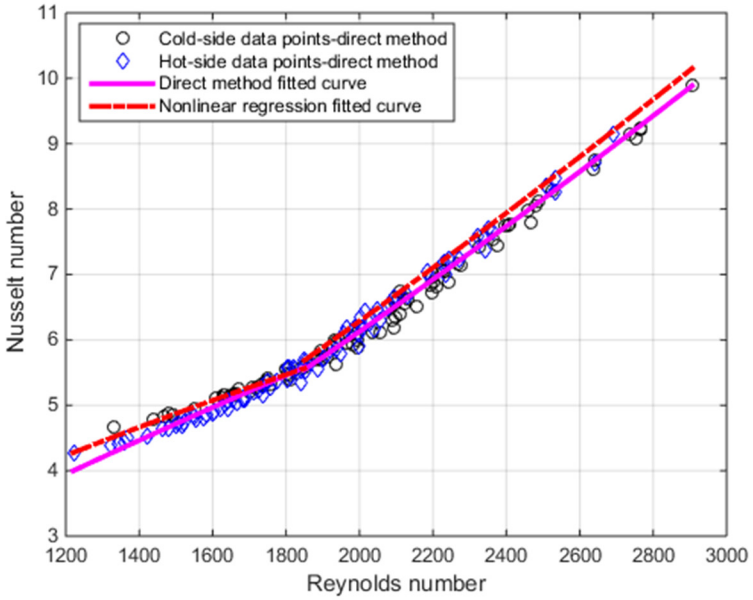

Figure 5-7. Comparison of the results obtained from the direct and indirect methods.

A comparison of the overall heat transfer coefficients obtained directly from the 15 reserved sets of the experimental data and the calculated overall heat transfer coefficients using Equations (5.3) and (5.4) is presented in Figure 5-8. The comparison showed that the calculated overall heat transfer coefficients were in good agreement with the experimental overall heat transfer coefficients. The differences between the calculated values and experimental data were within 5%. Although both the direct and indirect methods can predict the heat transfer coefficients for the tested PCHE well, only the correlation developed using the nonlinear regression method, i.e.,

Equation (5.4), was implemented in the dynamic code for the transient simulations to be discussed in the next section since it was the best fitted correlation with less assumptions from the experimental data.

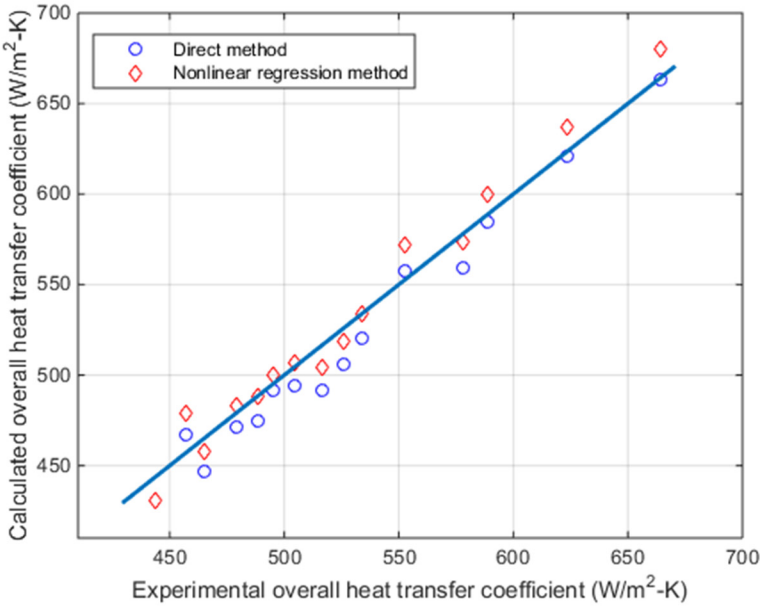

Figure 5-8. Comparison of the overall heat transfer coefficients obtained from fitted correlations and experiments.

5.3 Mathematical Models

The steady-state thermal performance of both the straight-channel and zigzag-channel PCHEs were discussed in the previous section and Chapter 3, respectively. For the dynamic study, the heat capacity of the heat exchanger plates was considered. The fluids on both sides were helium of the same mass flow rate under the initial stage. To develop the governing equations for transient analyses, the following assumptions were made:

(1) Negligible heat conduction in the solid plates and fluids along the flow direction;

(2) Negligible thermal resistance due to the heat conduction in the plate (Bi < 0.1);

(3) Negligible heat loss to the surroundings; and

(4) Uniform flow distribution into the flow channels on both sides.

It should be noted that some of these assumptions made for a reduced-scale PCHE might not be applicable to large-scale PCHEs. The test PCHEs are a two-stream countercurrent heat exchanger. Figure 5-9 shows two control volumes for the fluids inside two flow channels and a control volume in one of the non-etched portion on the plate. The following energy balance equations for the fluids and plate of both PCHEs can be obtained.

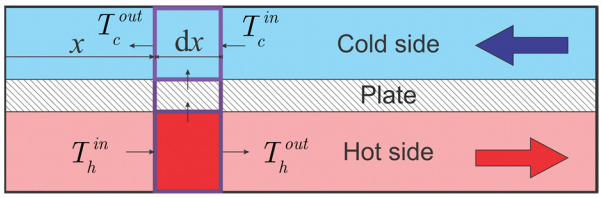

Figure 5-9. Control volumes for two fluids and solid plate.

5.3.1 Straight-channel PCHE

For the hot-side fluid:

$$m_h c_{p,h} \frac{\mathrm{d}T_h}{\mathrm{d}t} + \dot{m}_h c_{p,h} \left(T_h^{out} - T_h^{in}\right) = \left(hA\right)_h \left(T_P - T_h\right) \tag{5.5}$$

For the cold-side fluid:

$$m_c c_{p,c} \frac{\mathrm{d}T_c}{\mathrm{d}t} + \dot{m}_c c_{p,c} \left(T_c^{out} - T_c^{in}\right) = \left(hA\right)_c \left(T_P - T_c\right) \tag{5.6}$$

For the solid plate:

$$m_P c_{p,P} \frac{\mathrm{d}T_P}{\mathrm{d}t} = \left(hA\right)_h \left(T_h - T_P\right) - \left(hA\right)_c \left(T_P - T_c\right) \tag{5.7}$$

Here, the subscripts *h*, *c*, and *P* denote the PCHE hot-side fluid, cold-side fluid, and solid plate, respectively. A is the total heat transfer area in one specific control volume of the straight-channel PCHE. Superscripts *in* and *out* denote the fluid inlet and outlet temperatures for that control volume, respectively. It was also assumed that the hot and cold channel of interest were aligned on top of each other, and that that the heat transfer path is from the hot channel to the cold channel as shown in Figure 5-9.

5.3.2 Zigzag-channel PCHE

To account for the zigzag flow channels inside the heat exchanger, a parameter called surface area density, α, was introduced in the dynamic model.

For the hot-side fluid:

$$\rho_h c_{p,h} \frac{\partial T_h}{\partial t} + \rho_h c_{p,h} u_h \frac{\partial T_h}{\partial x} = \left(h\alpha\right)_h \left(T_P - T_h\right) \tag{5.8}$$

For the cold-side fluid:

$$\rho_c c_{p,c} \frac{\partial T_c}{\partial t} + \rho_c c_{p,c} u_c \frac{\partial T_c}{\partial x} = \left(h\alpha\right)_c \left(T_P - T_c\right) \tag{5.9}$$

For the solid plate:

$$\rho_P c_{p,P} \frac{\partial T_P}{\partial t} = h_h \alpha_P \left(T_h - T_P\right) - h_c \alpha_P (T_P - T_c) \tag{5.10}$$

where α is the surface area density [m^2/m^3]; and u is the flow velocity [m/s]. Heat conduction resistance of the ridges between channels could be neglected since the ridge width is small and the thermal conductivity of the plate material (Alloy 617) is relatively large. Therefore, the ridge efficiency η_f is assumed to be one. Then, the surface area density α can be expressed as

$$\alpha = \frac{A_f}{V}, \tag{5.11}$$

where A_f is the surface area that is in contact with the surrounding fluid [m^2] and V is the volume of a unit cell [m^3] for each fluid side or the solid plate. Note that the total fluid flow length is the actual fluid flow length, not the heat exchanger length.

5.4 Steady-State Numerical Simulations

In the current study, the flow path was divided into a number of small segments in the flow direction. A nodalization sensitivity study was performed for both the straight-channel and the zigzag-channel PCHEs. The helium inlet temperatures and mass flow rates on both sides of the PCHEs were obtained from steady-state calculations. The second terms on the left hand of Equations (5.5), (5.6), (5.8), and (5.9) for the fluid energy balance can be modified using a finite difference technique, converting all the partial differential equations (PDEs) to ordinary differential equations (ODEs). Transient scenarios were simulated using a MATLAB code that was developed in this study. Figure 5-10 presents the PCHE system nodal structure. Nodalization sensitivity study was performed to determine the effective number of segments used in the transient simulations based on the nominal operating conditions. The helium temperatures at the hot-side and cold-side outlets were recorded after the system reached a steady state in calculation.

These two helium outlet temperatures were compared to the nominal operation parameters that were used in the heat exchanger rating or sizing process.

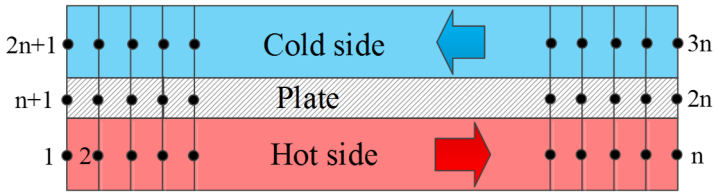

Figure 5-10. PCHE nodal structure.

5.4.1 Straight-channel PCHE

Five different numbers of segments were used in the nodalization sensitivity study. The helium inlet temperatures on both the hot and cold sides were kept at constants of 465.6 and 207.6 °C, respectively. The temperatures at the hot-side and cold-side outlets were recorded after the system reached a steady state in the calculations using the numerical model. These two helium outlet temperatures were compared to the values that were obtained from the heat exchanger rating process using the ε-NTU method. It can be seen from Table 5-2 that these five cases presented similar results without significant deviations for the straight-channel PCHE. The hot-side and cold-side temperature differences between the values using the $\varepsilon-\mathrm{NTU}$ method and the results obtained from the simulations for the five cases were mainly attributed to the fluid thermophysical properties. The fluid thermophysical properties were evaluated based on the average temperature for each helium stream in the heat exchanger rating process while the temperature-dependent properties were employed in each segment in the numerical simulations. Note that increasing the number of segments would considerably increase the computational time. It was observed from Table 5-2 that the helium outlet temperature differences on both sides tended to diminish when the

total number of segments were greater than 500. Therefore, a total of 500 segments were selected for the PCHE to simulate the transient scenarios in this study.

Table 5-2. Results of nodalization sensitivity study for the straight-channel PCHE.

	PCHE $\varepsilon - \mathrm{NTU}$ rating value	Number of segments				
		50	100	300	500	1,000
Hot-side helium outlet temperature (°C)	294	294	293.7	293.6	293.6	293.5
Cold-side helium outlet temperature (°C)	379.2	379.5	379.2	379.0	379.0	379.0

To predict the dynamic behavior of the straight-channel PCHE, steady-state operating parameters were first calculated by assuming constant helium fluid properties. The input parameters for the calculation included the helium inlet temperatures on both the hot and cold sides. The temperature distributions inside the PCHE, as shown in Figure 5-11, were obtained by dividing one hot helium stream, one cold helium stream, and one plate into 500 axial segments along the helium flow direction. The steady-state temperatures inside the PCHE and helium mass flow rates can serve as the initial condition for the transient simulations.

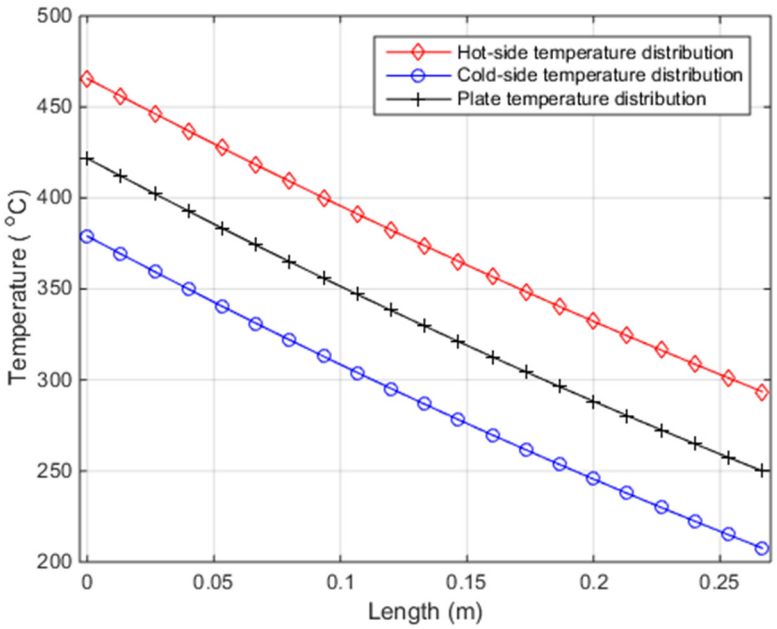

Figure 5-11. Temperature distributions inside the straight-channel PCHE.

5.4.2 Zigzag-channel PCHE

Similar to the straight-channel PCHE, five cases were carried out for the zigzag-channel PCHE and Table 5-3 presents the similar results without significant deviations for these five cases. The hot-side and cold-side temperature differences between the nominal values used in the heat exchanger sizing process (i.e., LMTD method) and the results obtained from the five cases with different segments were mainly attributed to the fluid thermophysical properties. A total of 500 segments of the PCHE were also selected to simulate the transient scenarios for the zigzag-channel PCHE. The steady-state temperature distributions inside the PCHE, as shown in Figure 5-12, were obtained by equally dividing each stream and plate into 500 segments along the helium flow direction. The temperature distributions inside the heat exchanger and helium mass flow rates can be used as the initial condition for the transient simulations.

Table 5-3. Results of nodalization sensitivity study for the zigzag-channel PCHE.

	Used in the LMTD method	Number of segments				
		50	100	300	500	1,000
Hot-side helium outlet temperature (°C)	462	463.7	463.1	462.7	462.6	462.6
Cold-side helium outlet temperature (°C)	688	687.3	686.5	686.0	685.9	685.8

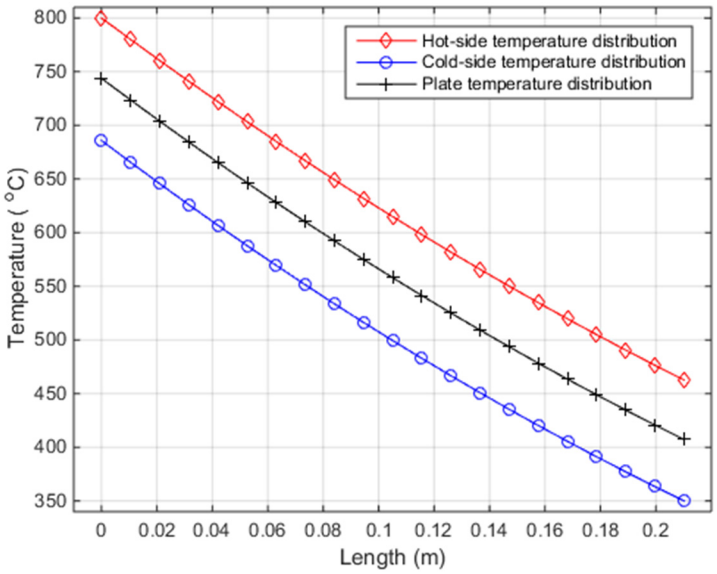

Figure 5-12. Temperature distributions inside the zigzag-channel PCHE.

5.4.3 Heat exchanger model verification

The dynamic model described above was verified in a previous study (Chen et al., 2015b) by comparing the numerical solution with the results obtained from a commercial software DYNSIM. A general countercurrent two-stream heat exchanger was adopted, and the parameters obtained from the thermal design of the heat exchanger under a steady-state condition were fed into

DYNSIM to simulate the dynamic behavior of the heat exchanger. Comparison of the results obtained from the dynamic model and DYNSIM simulations is shown in Figure 5-13. It was evident that the results obtained from the dynamic model and DYNSIM software presented a good agreement in depicting the dynamic behavior for a 10%-step increase in fluid mass flow rate on the cold side of the heat exchanger starting at 100 seconds.

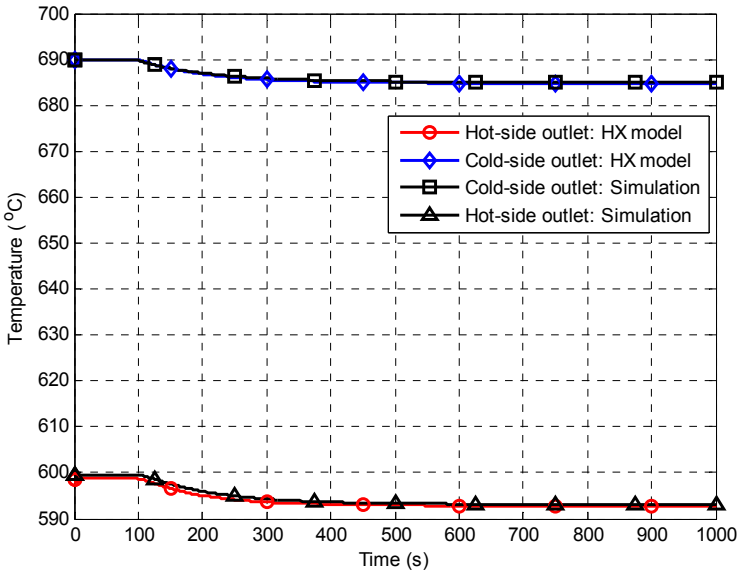

Figure 5-13. Heat exchanger model verification under flow step change condition (Chen et al., 2015b).

5.5 Transient Simulations

5.5.1 Straight-channel PCHE

A series of transient scenarios were performed to study the dynamic behavior of the straight-channel PCHE and also to assess the applicability of the dynamic model for use in the straight-channel PCHE under high-temperature helium-helium conditions. For helium inlet temperature

variations, the combinations of step change on one side and linear ramp change on the other side were performed. Similarly, the combinations of step change in helium mass flow rate on one side and linear ramp change on the other side were carried out. For the PCHE subject to combinations of the helium inlet temperature and mass flow rate variations, four cases in which the PCHE would experience the highest and lowest temperatures among the variation combinations were conducted. The detailed numerical simulation matrix is listed in Table 5-4.

The dynamic behavior of the PCHE subject to the helium inlet temperature variations was first studied. Figure 5-14 shows the hot-side and cold-side helium outlet temperature dynamic response due to the four cases of helium inlet temperature variation combinations initiated at 10 seconds. Note in this figure the solid and dotted lines represent the hot-side and cod-side helium outlet temperatures, respectively. For both the HSICRD and HRDCSI cases, the cold-side and hot-side helium outlet temperatures had an overshoot at the beginning of the transients. Conversely, undershoots were observed at the outlets on both sides for both the HRICSD and HSDCRI cases. This can be explained that the step changes dominated the transient scenarios during the initial stage. It took approximately 15 seconds for the temperatures to stabilize on both the hot and cold sides for all these temperature variation cases. It also can be seen from Figure 5-14 that the helium outlet temperatures for both the HSICRD and HRICSD cases were the same after the final steady states were reached in the calculations. Similar behavior was presented for the other two temperature variation transients. These results indicate that the final steady state is only determined by the degree of the temperature change at the beginning of the transient and is insusceptible to how the temperature change is initiated.

Table 5-4. Numerical simulation matrix for the straight-channel PCHE.

Case	Hot-side inlet	Cold-side inlet
a. Helium temperature variations		
HSICRD	50 °C step increase	50 °C linear ramp decrease within 10 seconds
HSDCRI	50 °C step decrease	50 °C linear ramp increase within 10 seconds
HRICSD	50 °C linear ramp increase within 10 seconds	50 °C step decrease
HRDCSI	50 °C linear ramp decrease within 10 seconds	50 °C step increase
b. Helium mass flow rate variations		
HSICRI	20% step increase	20% linear ramp increase within 10 seconds
HSDCRD	20% step decrease	20% linear ramp decrease within 10 seconds
HRICSI	20% linear ramp increase within 10 seconds	20% step increase
HRDCSD	20% linear ramp decrease within 10 seconds	20% step decrease
c. Helium inlet temperature combined with helium mass flow rate variations		
TSI-HSICSD	50 °C step increase	50 °C step increase
	20% flow rate step increase	20% flow rate step decrease
TRI-HRICRD	50 °C linear ramp increase within 10 seconds	50 °C linear ramp increase within 10 seconds
	20% flow rate linear ramp increase within 10 seconds	20% flow rate linear ramp decrease within 10 seconds
TSD-HSDCSI	50 °C step decrease	50 °C step decrease
	20% flow rate step decrease	20% flow rate step increase
TRD-HRDCRI	50 °C linear ramp decrease within 10 seconds	50 °C linear ramp decrease within 10 seconds
	20% flow rate linear ramp decrease within 10 seconds	20% flow rate linear ramp increase within 10 seconds

a. Helium inlet temperature variations

For the HSICRD and HRICSD cases, the hot-side helium outlet temperatures decreased from 293.6 to 271.2 °C and the helium cold-side outlet temperatures increased from 379 to 387 °C once new steady states were reached. The effectiveness of the reduced-scale PCHE under the initial steady state was 67%. The heat exchanger effectiveness was reduced to 64% after the temperature variation transients. However, the hot-side helium inlet temperature increase combined with the cold-side helium temperature decrease resulted in 38% more thermal energy transferring from the hot side to the cold side. The deviation of the energy transfer rate was about 6.14% between the hot side and the cold side in the final steady-state condition. For the HSDCRI and HRDCSI cases, the hot-side helium outlet temperature increased to 313.0 °C and the cold-side helium outlet temperature decreased to 365.8 °C. The combination of the hot-side helium temperature decrease and the cold-side helium temperature increase reduced 38.6% of the thermal energy transferring from the hot side to the cold side. The hot-side and cold-side energy transfer rate was within a deviation of 5.5%. Compared to the initial operation parameters, the heat exchanger effectiveness was slightly increased to 68%.

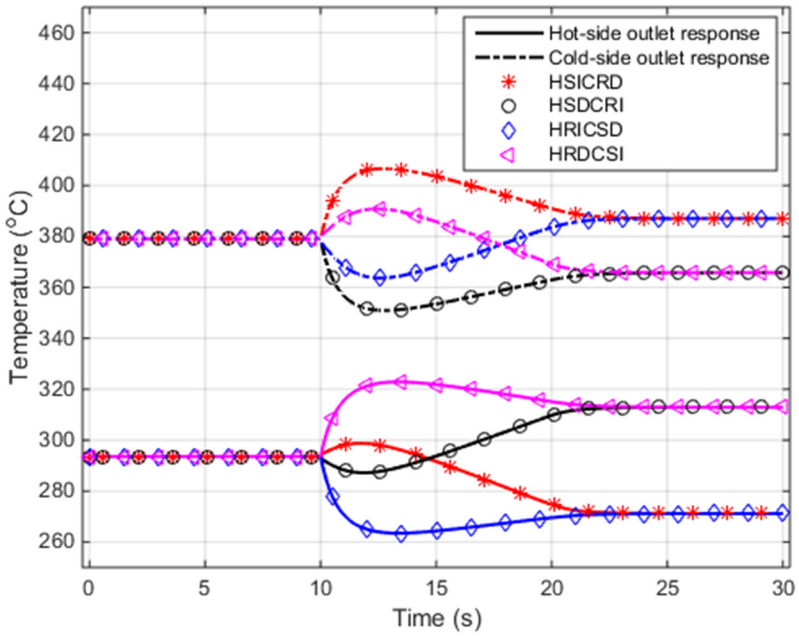

Figure 5-14. PCHE dynamic response to the helium inlet temperature variations.

b. Helium mass flow rate variations

In this section, dynamic response of the simulated PCHE subject to four cases of helium mass flow rate variation combinations was analyzed. The four scenarios for helium mass flow rate transient are listed in Table 5-4. Only changes in the helium mass flow rate were considered for each instance. That is, the helium inlet temperatures were kept constant on both sides for these simulations. Figure 5-15 shows the dynamic temperature response when the helium mass flow rates on both sides were changed at 10 seconds into the simulations. It can be seen that the helium outlet temperatures on both sides increased in the cases where the helium mass flow rates had a step increase on the hot side or a step decrease on the cold side at the beginning of the transients. The same final steady-state conditions were reached for either the helium mass flow rate increase or decrease on both sides in the calculations. The hot-side helium outlet temperatures decreased

from 293.6 to 290.9 °C and the cold-side helium outlet temperatures increased from 379 to 382.2 °C for the helium mass flow rate increase and decrease combinations, respectively. More thermal energy carried by the hot fluid would go into the heat exchanger due to the increase of the helium mass flow rate on the hot side while more thermal energy would be removed from the heat exchanger due to the increase of the cold-side helium mass flow rate. The hot-side heat transfer coefficients increased by 26.8% (i.e., from 1,167 to 1,480 W/(m^2-°C)) and decreased by 13.2% (i.e., from 1,167 to 1,013 W/(m^2-°C)) due to the hot-side helium mass flow rate increase and decrease, respectively. The cold-side heat transfer coefficients for the helium mass flow rate step increase and step decrease rose by 26.3% (i.e., from 1,201 to 1,517 W/(m^2-°C)) and reduced by 18.7% (i.e., from 1,201 to 976 W/(m^2-°C)), respectively. The increasing helium mass flow rates on both sides resulted in 1.8% more thermal energy transferring from the heat exchanger's hot side to the cold side. It also can be calculated that 1.7% more thermal energy was exchanged for the decreasing helium mass flow rate combinations. The deviations of the energy transfer rate were approximately 0.11 and 0.06% after the steady states were reached for the helium mass flow rate increase and decrease combinations, respectively.

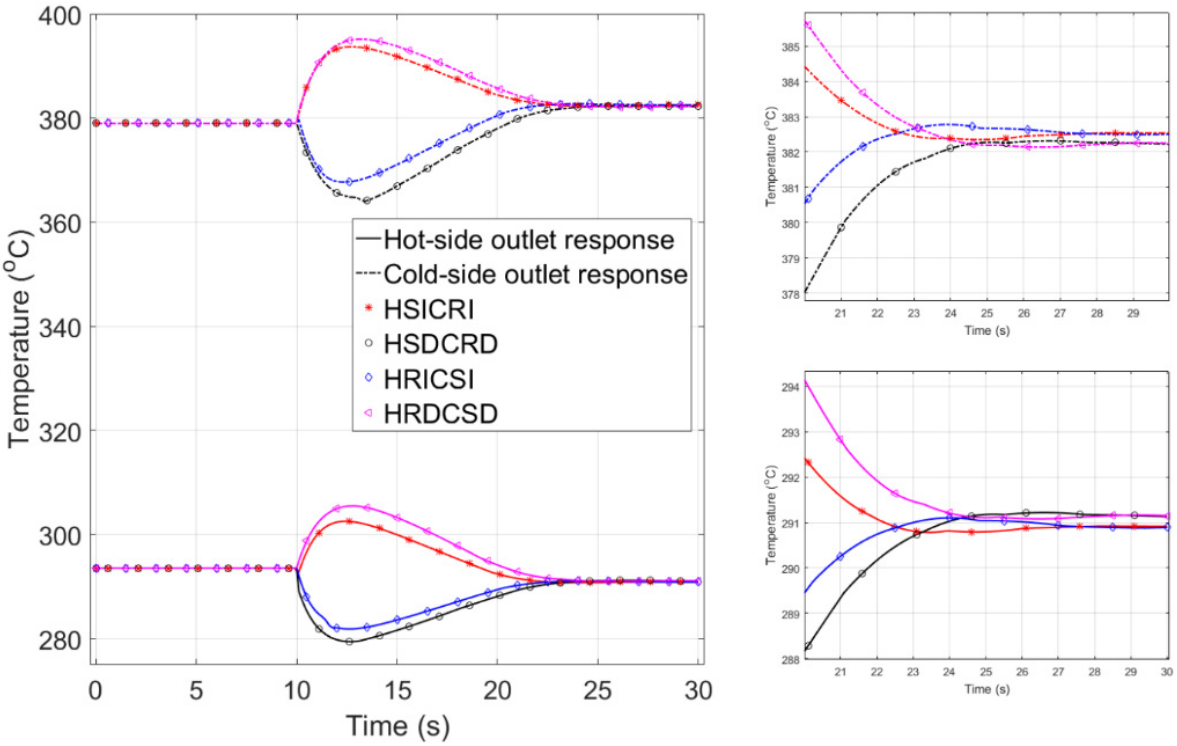

Figure 5-15. PCHE dynamic response to the helium mass flow rate variations.

c. Helium inlet temperature and helium mass flow rate variation combinations

The PCHE may experience a condition of the highest temperature when both of the helium inlets encounter a temperature increase, helium mass flow rate increases on the hot side but decreases on the cold side. On the contrary, the PCHE would undergo a condition of the lowest temperature. Both conditions were studied in this section with the same degrees of change as the helium inlet temperature and mass flow rate variations conducted in the previous sections (i.e., 50 °C step changes and helium mass flow rate 20%-step changes). The transient test matrix is listed in Table 5-4. Figure 5-16 presents the helium outlet temperature evolutions for these four transient scenarios. The highest helium outlet temperatures on the cold and hot sides were about 471.4 and

374.9 °C, respectively. The lowest helium outlet temperatures on the cold and hot side were 284.2 and 219.3 °C, respectively. The heat exchanger effectiveness was increased from 67 to 83% for the helium inlet temperature increasing cases while decreased to 49% for the helium inlet temperature decreasing scenarios. Compared to the initial operating condition, the thermal energy transferred from the heat exchanger's hot side to the cold side was reduced by 10% for the lowest temperature cases. This study provides useful information for the PCHE operation since the helium inlet temperature variations combined with its mass flow rate variations would potentially lead to an overheating or overcooling condition for the PCHE and therefore the reactor primary system.

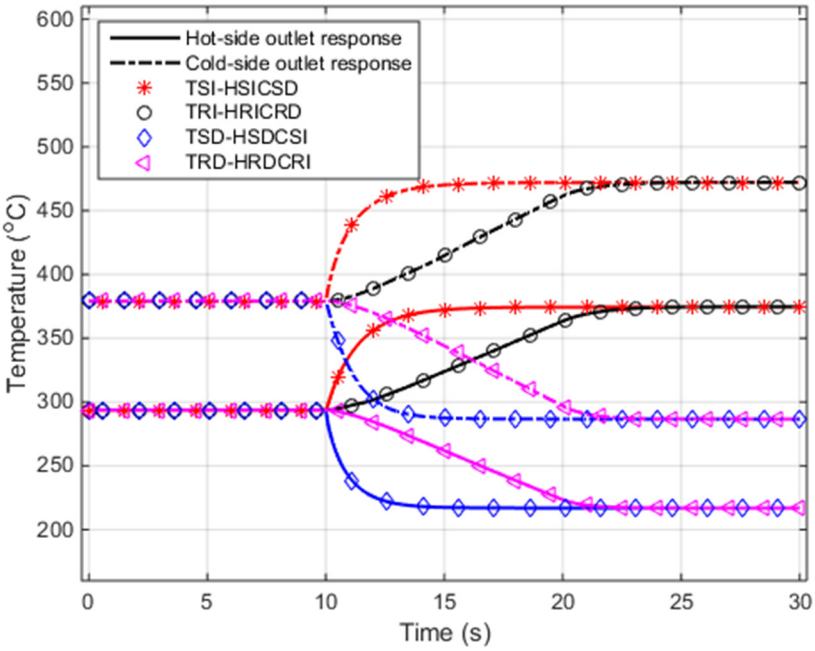

Figure 5-16. Temperature evolutions for the helium inlet temperature combined with helium mass flow rate variations.

In all the transients simulated, for the dynamic response to the 50 °C variation in the helium inlet temperatures of the test PCHE, the helium inlet temperature increase on the hot side combined with the temperature decrease on the cold side would enhance the heat transfer capability of the

heat exchanger while reduce the heat exchanger effectiveness. On the contrary, the helium inlet temperature decrease of 50 °C on the hot side combined with an helium inlet temperature increase of 50 °C on the cold side would increase the heat exchanger effectiveness but reduce the heat transfer capability. For the 20% of the helium mass flow rate variation combinations, both the heat exchanger effectiveness and heat transfer capability would increase. This dynamic study provides meaningful insight to improve the heat exchanger effectiveness and heat transfer capability when operating it under dynamic conditions. It also provides useful information for developing control strategies to effectively operate the PCHE as an IHX in VHTRs (Skavdahl et al., 2016a and 2016b).

5.5.2 Zigzag-channel PCHE

To test the developed dynamic model and examine the behaviors of the zigzag-channel PCHEs under various transient scenarios, a number of numerical simulations were conducted in this section. The numerical model for the zigzag-channel PCHE was tested using following transient scenarios: (1) 50 °C-step increase separately in the helium inlet temperatures on the PCHE hot and cold sides; (2) 50 °C-step decrease separately in the helium inlet temperatures on the PCHE hot and cold sides; (3) 20%-step increase separately in the helium mass flow rates on the PCHE hot and cold sides; and (4) 20%-step decrease separately in the helium mass flow rates on the PCHE hot and cold sides. The initial condition of the transient simulations was obtained from the steady-state calculations in Section 5.4.2. For these simulations, only one variation was introduced at one time for each instance. For example, the helium mass flow rates were kept constant on both sides when performing the simulations of the helium temperature variations and the helium inlet

temperatures on both sides were kept constant when conducting the simulations of the helium mass flow rate variations.

a. Dynamic response to helium temperature variations

Figure 5-17 and Figure 5-18 show the simulated PCHE dynamic response to the helium inlet temperature step changes. As noted, the helium mass flow rates on both sides were kept constant (26.45 kg/h) when simulating the helium temperature step-increase transient scenarios. Figure 5-17 shows the hot-side and cold-side helium outlet temperature dynamic response due to the 50 °C-step increase at the hot-side inlet that was initiated at 10 seconds. The cold-side helium outlet temperature increased from 685.9 to 724.0 °C after the helium temperature step increase at the hot-side inlet and the hot-side helium outlet temperature increased from 462.6 to 471.1 °C. The simulation shows that it took approximately five seconds for helium temperatures to stabilize on both the hot and cold sides. The hot-side temperature step increase resulted in 11.82% more thermal energy transferring from the heat exchanger's hot side to its cold side. After the new steady-state operation condition was reached, the deviation in the energy transfer rates was about 1.3% between the hot side and cold side. The effectiveness of the reduced-scale PCHE under the nominal operation condition was 75%. After the 50 °C-step increase in the helium temperature on the hot side, the heat exchanger effectiveness slightly increased to 75.8%.

Figure 5-17 also shows the hot-side and cold-side helium outlet temperature variations due to the 50 °C-step decrease at the hot-side inlet initiated at 10 seconds. The cold-side helium outlet temperature decreased from 685.9 to 648.0 °C after the temperature step decrease at the hot-side

inlet and the hot-side helium outlet temperature decreased from 462.6 to 453.5 °C. It also took approximately five seconds for the helium temperatures to stabilize on both sides. The step decrease in the helium inlet temperature at the hot-side reduced the thermal energy transfer from the hot side to cold side of the heat exchanger by 11.8%. After the steady-state operation condition was reached in the calculation, the hot-side and cold-side energy transfer rates were within a 0.5% deviation. Compared to the nominal operation parameters, the heat exchanger effectiveness decreased to 74.1%.

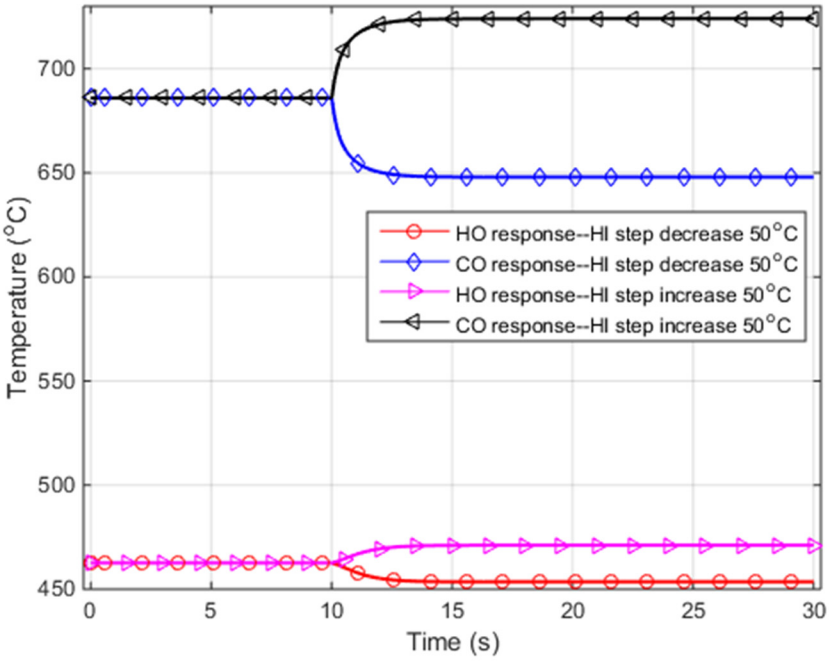

Figure 5-17. PCHE dynamic response to hot-side helium inlet temperature 50 °C-step changes.

Similarly, the hot-side and cold-side helium outlet temperature variations due to the 50 °C-step increase and decrease at the cold-side inlet initiated at 10 seconds are shown in Figure 5-18. During a steady-state operation, the lowest helium temperature position in the heat exchanger locates at the cold-side inlet. A helium temperature step increase or decrease at the cold-side inlet would lead

to the average temperature increase or decrease for the entire heat exchanger. For the temperature step increase at the cold-side inlet, the hot-side and cold-side helium outlet temperatures rose from 462.6 and 685.9 °C to 500.8 and 704.6 °C, respectively. Contrary to the helium temperature step increase at the hot-side inlet, 50 °C-step increase at the cold-side inlet reduced the heat transfer capability of the PCHE by approximately 10.3%, while the heat exchanger effectiveness decreased only by 0.2% relative to the original effectiveness. For the temperature step decrease at the cold-side inlet, the hot-side and cold-side helium outlet temperatures decreased from 462.6 and 685.9 °C to 424.2 and 664.8 °C, respectively. An increase of more than 9% of thermal energy transferred from the hot side to cold side was achieved due to the temperature step decrease. As can be observed from Figure 5-18, it also took about five seconds for both the hot-side and cold-side temperatures to stabilize. The heat exchanger effectiveness increased 0.2% relatively due to the cold-side helium inlet temperature step decrease. After the steady-state operations were reached in calculations, the deviations in the energy balance were within 1.8 and 2.9% for the cold-side helium inlet temperature step increase and step decrease, respectively.

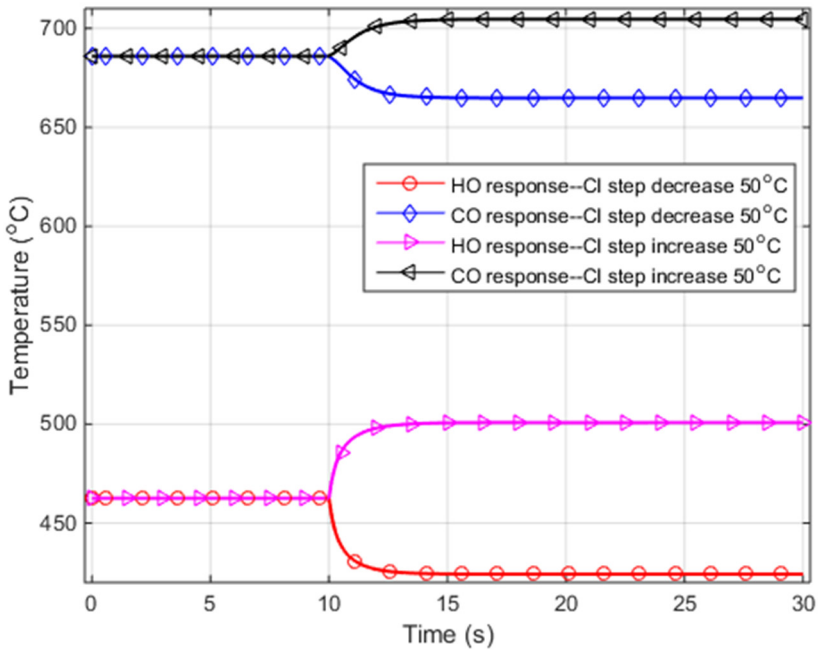

Figure 5-18. PCHE dynamic response to cold-side helium inlet temperature 50 °C-step changes.

Only 50 °C-step changes were presented in detail in this study for the helium inlet temperature variation transients. Different magnitudes of step changes would result in different behaviors for the effectiveness and heat transfer capability of the heat exchanger. Figure 5-19 and Figure 5-20 depict the heat exchanger effectiveness and heat transfer capability changes under different values of temperature changes. It can be observed from both figures that increasing the helium temperature increase at the hot-side inlet and decrease at the cold-side inlet would increase both the heat exchanger effectiveness and heat transfer capability. On the contrary, helium inlet temperature decreases on the hot side or increases on the cold side would reduce both the heat exchanger effectiveness and heat transfer capability. The larger the amount of the temperature change, the greater changes in the heat exchanger effectiveness and heat transfer capability. This study provided some information to effectively operate the PCHE under helium temperature variation conditions.

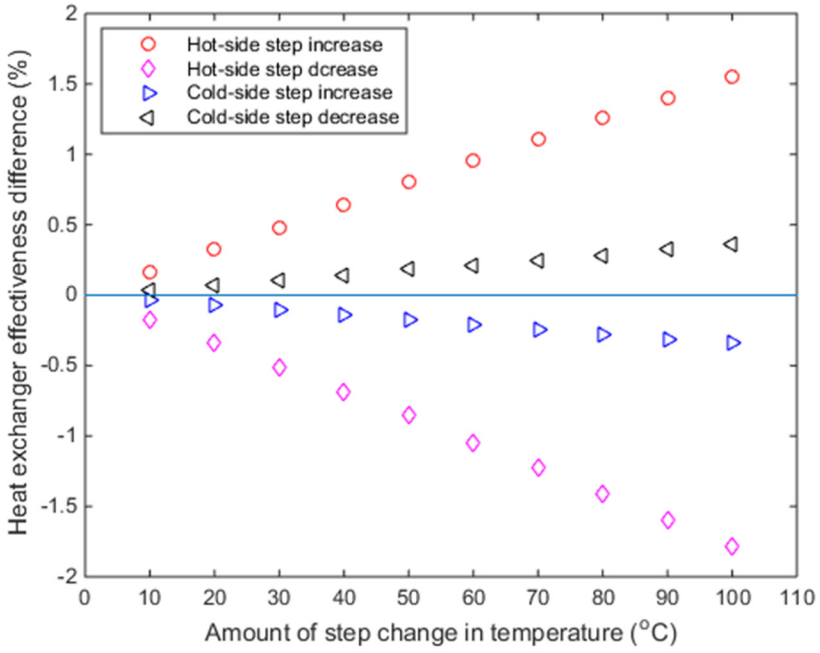

Figure 5-19. Heat exchanger effectiveness changes under different amounts of step change in helium temperature.

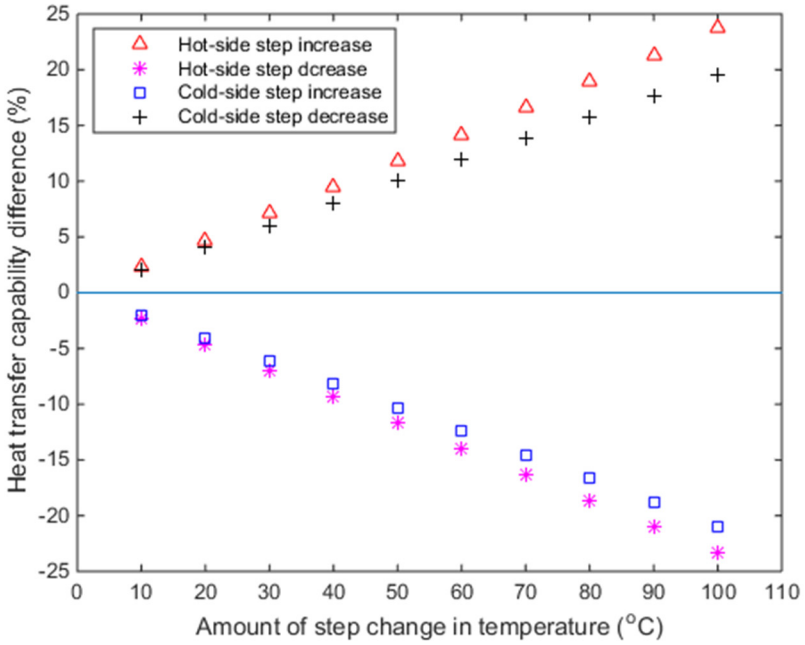

Figure 5-20. Heat transfer capability changes under different amounts of step change in helium temperature.

b. Dynamic response to flow rates variations

Figure 5-21 and Figure 5-22 show the simulated PCHE dynamic responses to the helium mass flow rate variations. The helium inlet temperatures were kept constant as their nominal values on both sides when simulating the helium flow rate variation scenarios. Figure 5-21 shows the dynamic helium temperature response when the hot-side helium mass flow rate was increased by 20% (i.e., from 26.45 to 31.74 kg/h) at 10 seconds, i.e., the transient is again initiated at 10 seconds. The cold-side helium inlet mass flow rate was maintained at 26.45 kg/h during the transient. It can be seen that the helium temperatures for both sides increased until a new steady state was reached in the calculation. More thermal energy carried by the hot-side helium went into the heat exchanger due to the helium mass flow rate increase on the hot side, which led to the helium temperature increase in the heat exchanger. The cold-side and hot-side helium outlet temperatures increased from 685.9 to 716.2 °C and from 462.6 to 492.6 °C within less than five seconds, respectively. The energy transfer rate deviation between the hot side and cold side was approximately 1.3% after the helium mass flow rate step change. Compared to the nominal operation condition, the helium temperature difference between the inlet and outlet on the hot side of the heat exchanger decreased by 9.1% while the difference increased by 9.0% on the cold side. The overall heat exchanger effectiveness increased from 75 to 81%. The increasing hot-side helium mass flow resulted in 9.2% more energy transfer from the hot side to cold side.

Figure 5-21 also presents the temperature response when the hot-side helium mass flow rate was decreased by 20% (i.e., from 26.45 to 21.16 kg/h) while the cold-side helium mass flow rate was fixed at 26.45 kg/h. It was observed that the hot-side and cold-side helium outlet temperatures

decreased from 462.6 and 685.9 °C to 430.8 and 643.5 °C, respectively. The heat exchanger effectiveness decreased from 75 to 65%. The deviation of the energy transfer rate balance between the two sides was approximately 0.5% after the new steady state was reached in the calculation. The helium temperature difference between the inlet and outlet on the hot side increased by 9.4% while that reduced by 12.6% on the cold side. The heat transfer capability was reduced by 12.5% due to the helium mass flow rate step decrease on the hot side. In addition, the hot-side heat transfer coefficients increased from 2,511 to 2,849 W/(m^2-°C) and decreased from 2,511 to 2,152 W/(m^2-°C) due to the hot-side helium mass flow rate increase and decrease, respectively.

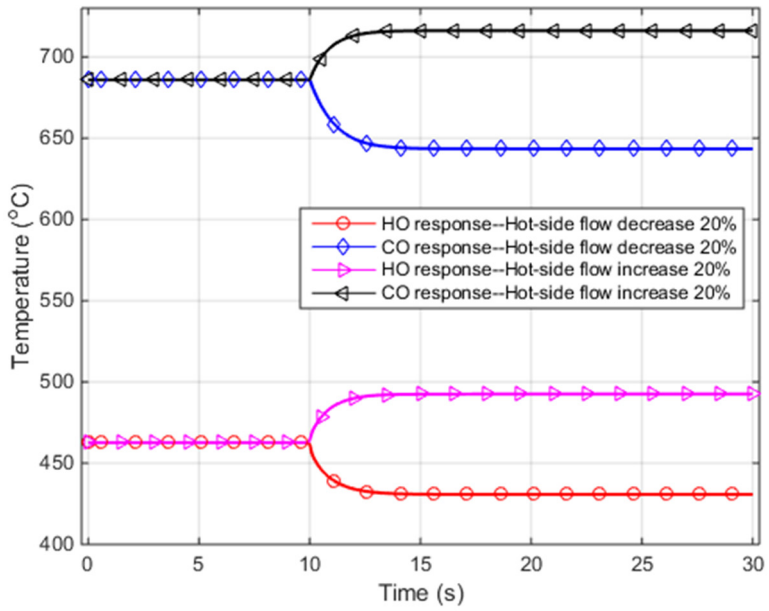

Figure 5-21. Temperature evolutions following the hot-side helium mass flow rate 20%-step changes.

Similar transient response analyses were also performed when the helium mass flow rate on the cold side experienced a step increase or decrease. Figure 5-22 shows the helium temperature response when the cold-side helium mass flow rate was increased by 20% at 10 seconds. More

thermal energy would be removed from the hot side than the initial steady state due to the increase of the cold-side helium mass flow rate, resulting in helium temperature decreases at the outlets of both sides. Figure 5-22 also depicts the temperature response when the cold-side helium mass flow rate was decreased by 20% at 10 seconds. Less energy would be removed from the hot side than the initial condition, which leads to helium temperature increases at the outlets on both sides. The cold-side heat transfer coefficients for the helium mass flow rate step increase and step decrease increased from 2,437 to 2,765 W/(m^2-°C) and reduced from 2,437 to 2,088 W/(m^2-°C), respectively. The heat exchanger effectiveness was increased by 9% due to the cold-side mass flow rate step decrease while decreased by 9% for the helium mass flow rate step increase on the cold side, primarily due to the changes of the residence time of the cold helium in the heat exchanger despite the cold-side heat transfer coefficient changes.

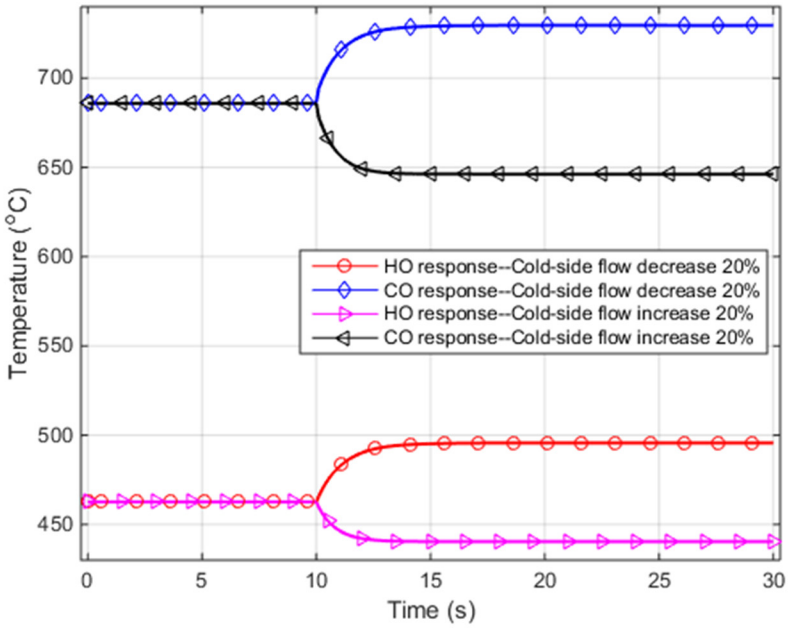

Figure 5-22. Temperature evolutions following the cold-side helium mass flow rate 20%-step changes.

For the dynamic responses to the helium mass flow rate variations, increasing mass flow rate on either side would enhance the heat transfer capability of the test PCHE while increasing helium mass flow rate by 20% on the cold side or decreasing helium mass flow rate by 20% on the hot side would reduce the test PCHE effectiveness. The simulated results could provide some insights for control strategy development for an integrated high-temperature reactor system with process heat applications, such as using the helium mass flow rate control to adjust the heat exchanger effectiveness and heat transfer rate.

5.6 Experimental Results and Discussions

5.6.1 Straight-channel PCHE

The dynamic model discussed was for the first time introduced for straight-channel PCHE transient analyses. Two sets of transient tests were experimentally carried out to assess the applicability of the dynamic model, which are the straight-channel PCHE subject to helium inlet temperature increase and decrease on the hot side. A temperature step change on the heat exchanger's inlets is not applicable in the current study due to the limited heater capability and the configuration of the HTHF. For experiments carried out in the HTHF, helium mass flow rates were controlled by a gas booster and helium temperatures by the two electric heaters. Although a temperature step increase or step decrease was not readily achievable, the helium temperatures after exiting the two electric heaters can be adjusted by changing the set points of the temperature controllers for the heaters and these temperature variations could be captured by the data acquisition system. The hot-side helium inlet temperature was increased in the first test and decreased in the second test. The cold-

side helium inlet temperature was maintained at a constant value for both tests. After the PCHE reached a steady state in both tests, temperature variations at the inlet of the hot side were introduced by adjusting the main-heater power via the temperature controller in the HTHF to initiate the transients.

For the transient test initiated by the hot-side helium inlet temperature increase, the cold-side helium inlet temperature and the helium mass flow rates on both sides were kept approximately constants at 49.9 °C and 31.7 kg/h, respectively. A polynomial function was used to fit the hot-side helium inlet temperature data, as shown in Figure 5-23, and was implemented in the dynamic model. The helium outlet temperatures for both the hot and cold sides obtained from the numerical simulation were compared to the experimental data, as shown in Figure 5-24. It was observed that the numerical results predicted the experimental trends well. There were some discrepancies for both the helium outlet temperatures at the initial steady-state condition, which is believed to be primarily attributed to the heat loss from the heat exchanger surfaces. The numerical results on both sides slightly over predicted the experimental values at the initial steady state, i.e., prior to the initiation of the transient around 1,000 seconds. At the end of the transient scenario around 7,200 seconds, the hot-side helium outlet temperatures obtained from the dynamic model and experiments were in good agreement. Compared to the experimental results, the outlet temperature differences had deviations of 0.8 °C and 4.2 °C for the initial and final steady states, respectively. The helium outlet temperature difference is the temperature difference between the hot-side and cold-side helium outlet temperatures. The heat loss ratio increased from 8.4 to 11.25% as the hot-side helium inlet temperature was increased.

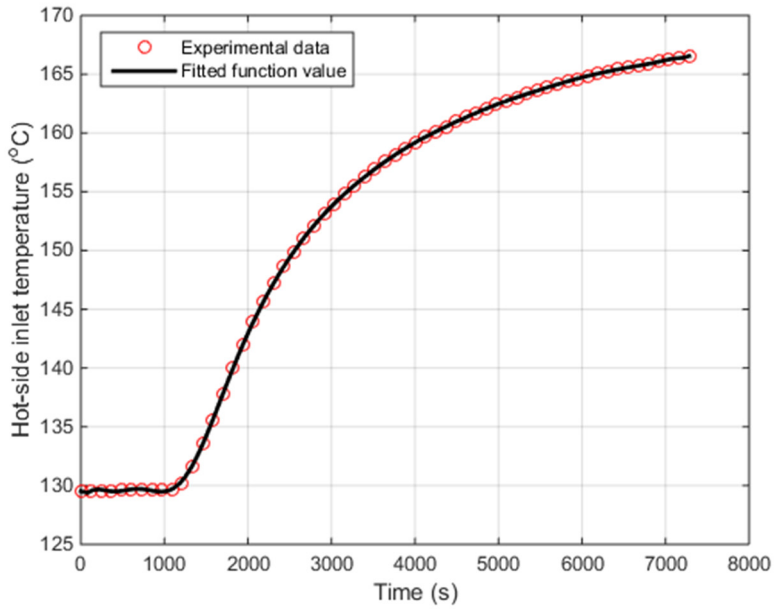

Figure 5-23. Curve fitting to the hot-side helium inlet temperature experimental data as a function of time.

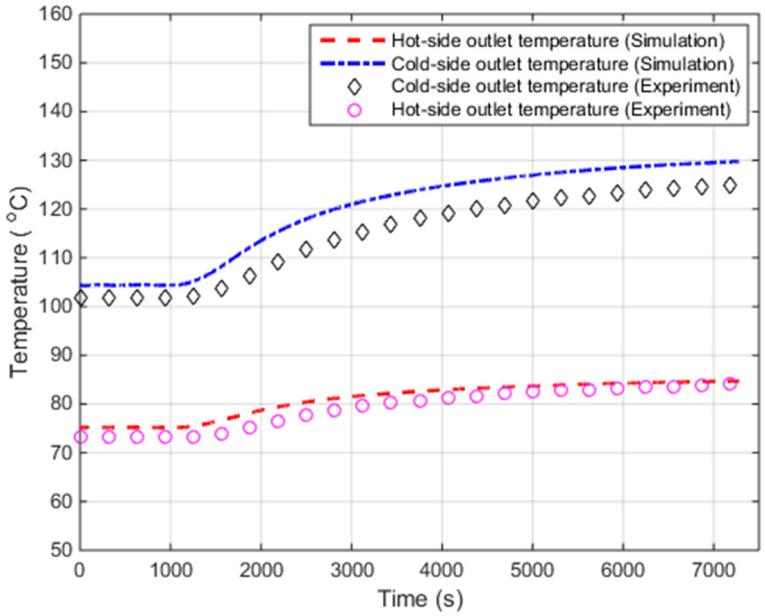

Figure 5-24. Helium outlet temperature profiles following the hot-side helium inlet temperature increase shown in Figure 5-23.

A similar analysis methodology was applied to the second transient test, in which the hot-side helium inlet temperature was decreased around 1,000 seconds into the test, as shown in Figure 5-25, where the experimental data were curve fitted. The helium outlet temperatures for both the hot and cold sides from the numerical simulation were compared to the experimental data, as shown in Figure 5-26. It was observed that the numerical results also predicted the experimental trends well. However, there were even larger discrepancies as compared to the first test, which was also mainly attributed to the heat loss from the heat exchanger surfaces. Compared to the experimental results, the helium outlet temperature differences had deviations of 3.9 °C and 2.0 °C for the initial and final steady states, respectively. The heat loss ratio decreased from 13.0 to 12.3% as the hot-side helium inlet temperature was decreased.

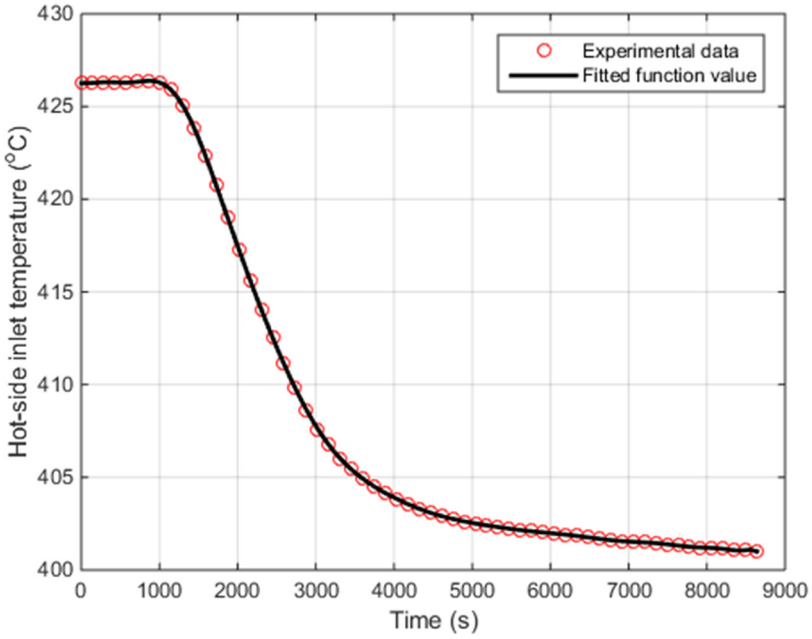

Figure 5-25. Curve fitting to the hot-side helium inlet temperature experimental data as a function of time.

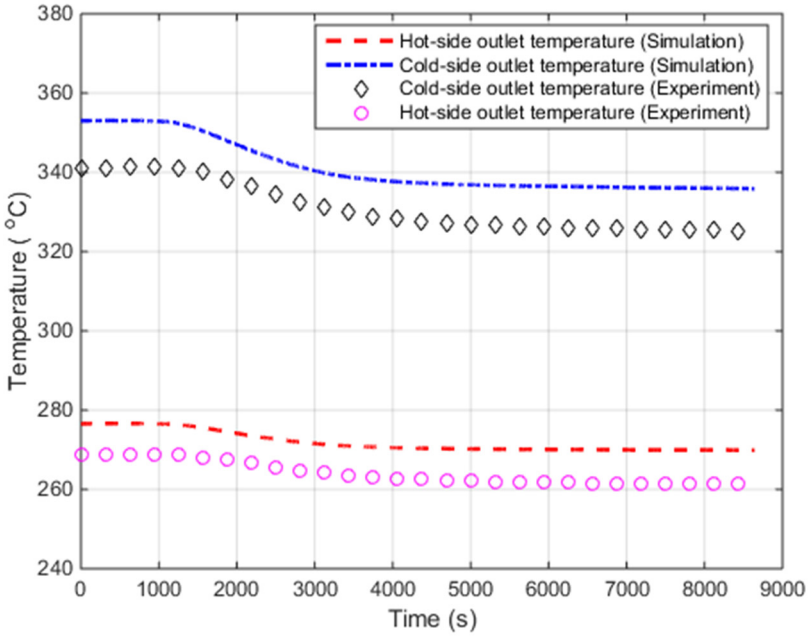

Figure 5-26. Helium outlet temperature profiles following the hot-side helium inlet temperature decrease shown in Figure 5-25.

5.6.2 Zigzag-channel PCHE

Three sets of transient tests were experimentally carried out to confirm feasibility of the dynamic model. The uncertainties of the temperature and mass flow rate measurements in experiments were within ±2 and ±6%, respectively, at 95% confidence level. For the first case, the only variation introduced was the hot-side helium inlet temperature. For the second case, both the hot-side and cold-side helium inlet temperatures were varied. Three variations were simultaneously applied in the third case, namely, the hot-side helium inlet temperature, the cold-side helium inlet temperature, and the helium mass flow rate step changes on both sides. To perform temperature transient tests in the HTHF, the helium temperatures at the two electric heaters' outlets can be alternated by changing the temperature controllers' setting points. Adjusting the flow rate or inlet

pressure of the driving air for the gas booster or both would result in changes of the helium flow rate in the HTHF. Both operations were simultaneously applied to the third transient test. Note that all the helium mass flow rates for transient simulations were within the range of the steady-state experimental conditions, which means that the application range of the obtained heat transfer correlations covers all the experimental conditions for both the steady states and transients in the current study.

a. Case 1: Change in the hot-side helium inlet temperature

Tests with the helium temperature step changes at the heat exchanger inlet could not be readily carried out in the HTHF due to the limited heater capability and the facility configuration. The helium mass flow rates were controlled by a gas booster and helium temperatures were governed by the two electric heaters. Although a helium temperature step increase or decrease was not readily achievable, certain helium temperature variations could still be introduced and captured during experiments via the data acquisition system. After the PCHE reached a steady-state condition, helium temperature variations at the inlet of the PCHE hot side were introduced at around 850 seconds by controlling the main-heater power via the temperature controller in the HTHF. During this transient test, the cold-side helium inlet temperature and mass flow rates on both sides were kept constant at about 94.5 °C and 30.5 kg/h, respectively. The fixed cold-side helium inlet temperature can be achieved by maintaining the pre-heater power while bypassing the straight-channel PCHE (upstream of the zigzag-channel test PCHE) in the HTHF as shown in Figure 3-2. Once the straight-channel PCHE was bypassed, the zigzag-channel PCHE cold-side helium inlet temperature was controlled by the pre-heater and the hot-side helium inlet temperature

by the main-heater. A polynomial function was used to fit the measured hot-side helium inlet temperature curve as shown in Figure 5-27 and severed as an input in the dynamic model. The helium outlet temperatures on both the hot and cold sides from the numerical simulation were compared to the experimental data, as shown in Figure 5-28. It was observed that the numerical results predicted the experimental results well. The numerical simulation on the cold side slightly under predicted the experimental value during the initial steady state. After having reached the next steady state, the hot-side numerical and experimental results gave good agreement. Compared to the experimental results, the PCHE helium outlet temperature differences for the initial and final steady state had deviations of 10.1 and 6.5%, respectively.

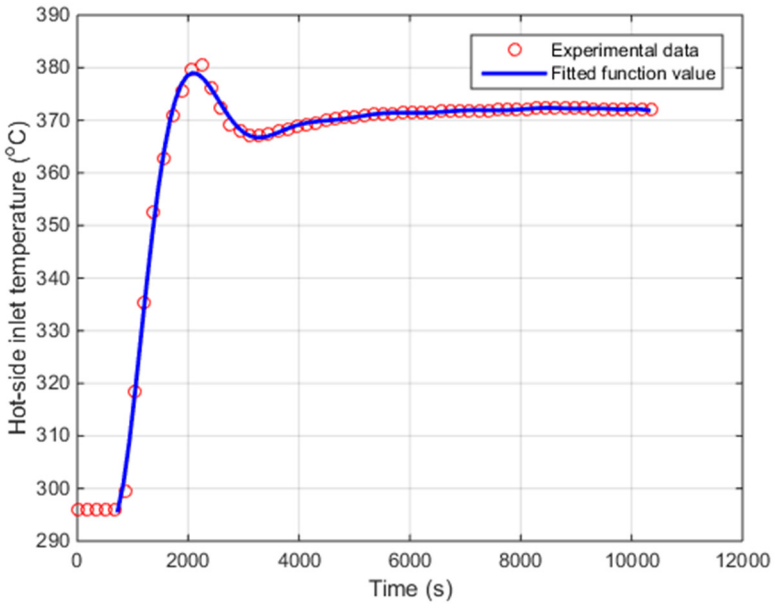

Figure 5-27. Measured Hot-side helium inlet temperature profile for Case 1 and the fitted curve.

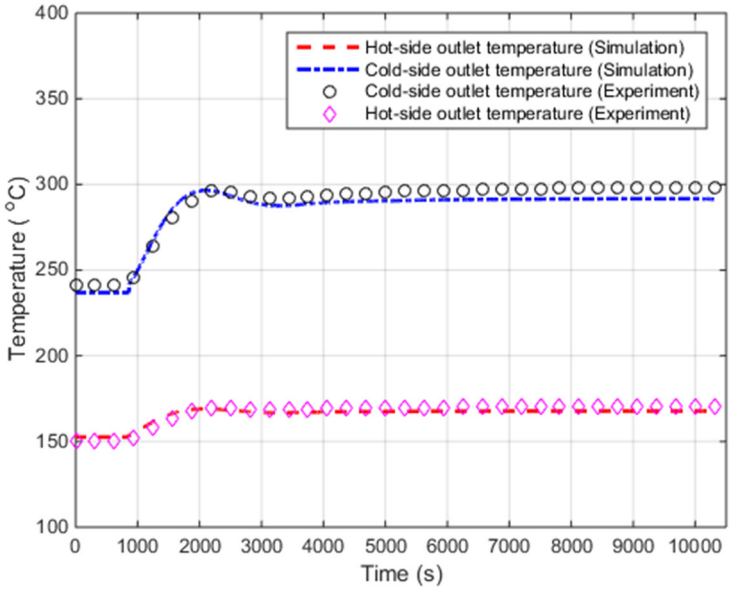

Figure 5-28. Comparisons of the helium outlet temperature profiles in Case 1: Measurements vs. predictions.

b. Case 2: Change in both the hot-side and cold-side helium inlet temperatures

In the second transient test, the straight-channel PCHE in the HTHF was not bypassed. Since the two PCHEs (i.e., the straight-channel PCHE and the zigzag-channel PCHE) were coupled in the HTHF, as shown in Figure 3-2, the cold-side helium inlet temperature for the zigzag-channel PCHE would increase if its hot-side helium inlet temperature is increased. Unlike the first case, two fitted functions for both helium inlet temperatures of the zigzag-channel PCHE monitored in the experiment were implemented in the dynamic model to simulate the PCHE response. The fitted polynomial curves followed the experimental data well for both the hot-side and cold-side helium inlet temperatures, as can be seen in Figure 5-29. From the figure, the hot-side helium inlet temperature increased from 767.0 to 802.0 °C and was maintained at 802.0 °C for more than an hour. Comparisons of the helium outlet temperatures obtained from experiments and numerical

simulations are shown in Figure 5-30. The cold-side outlet numerical results predicted the experimental data very well with an over-prediction of 0.2 °C for the final steady state. Due to the heat loss from the heat exchanger surfaces, the numerical model over predicted the hot-side experimental results by about 9.0 °C for the initial steady state and by 2.5 °C for the final steady state.

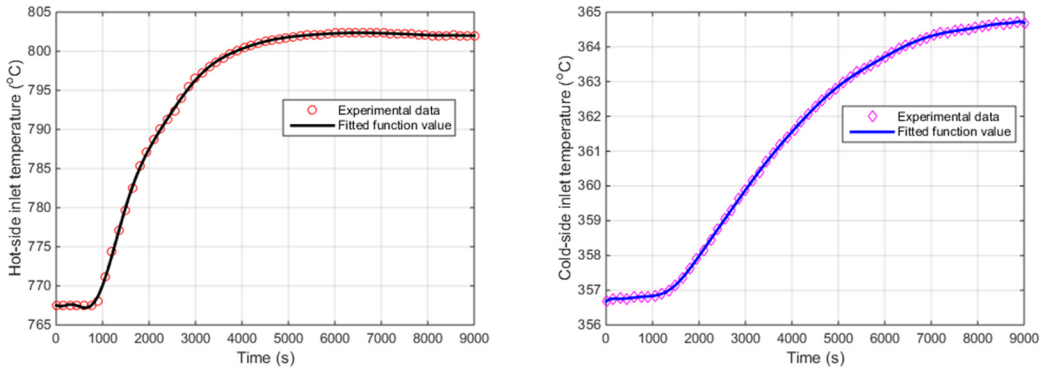

Figure 5-29. Measured hot-side (left) and cold-side (right) helium inlet temperature profiles for Case 2 and their fitted curves.

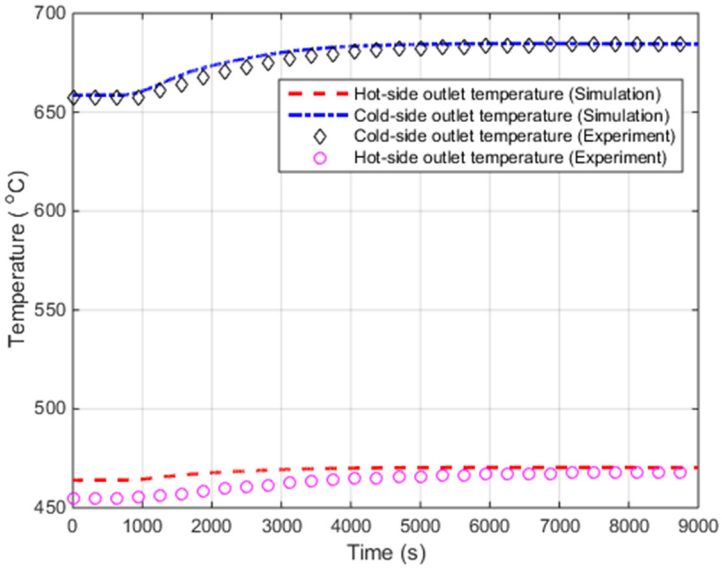

Figure 5-30. Comparisons of the helium outlet temperature profiles in Case 2: Measurements vs. predictions.

c. Case 3: Helium mass flow rate step change with helium inlet temperature variations

For the third transient test, three variations were simultaneously applied, namely, the hot-side helium inlet temperature, the cold-side helium inlet temperature, and the helium mass flow rate step changes on both sides of the heat exchanger. The hot-side helium inlet temperature was increased from 724.0 to 768.7 °C. As mentioned, the cold-side helium inlet temperature would change accordingly due to the two coupled PCHEs in the HTHF. Two fitted polynomial functions to the experimental data of both the hot-side and cold-side helium inlet temperatures are shown in Figure 5-31. Simultaneously, the helium mass flow rate was subjected to a step decrease from 35.3 to 31.8 kg/h at around 700 seconds and then a step increase from 31.8 to 34.7 kg/h at about 4,700 seconds, as shown in Figure 5-32. There are some oscillations in the helium mass flow rate measurements, but the standard deviation of each operated helium mass flow rate stage was less than 2%

As can be seen from Figure 5-31, the response of the cold-side helium inlet temperature is slower than that of the hot-side helium inlet temperature variations. This is mainly attributed to the thermal inertia of the test loop and the fluid flow lengths in the loop to reach the hot-side inlet and cold-side inlet locations. As can be seen from Figure 3-2, the helium gas was heated in both the pre- and main- heaters. The helium temperature variations in the zigzag-PCHE hot-side inlet were mainly caused by the main heater. The helium flow path is from the zigzag-PCHE cold-side outlet to its hot-side inlet through the main heater. The helium temperature variations in the zigzag-PCHE cold-side inlet are mainly caused by the pre-heater and the straight-channel PCHE at the low-temperature side of the HTHF. The helium gas travel path is from the zigzag-PCHE hot-side outlet,

cooler, and the gas booster, passing the pre-heater and straight-channel PCHE, to the zigzag-PCHE cold-side inlet, which is much longer than that from the zigzag-PCHE cold-side outlet to its hot-side inlet. Therefore, the helium gas travel path from the zigzag-PCHE hot-side outlet to its cold-side inlet has a significantly higher thermal inertia, which in turn results in a much slower transient response for the zigzag-channel PCHE cold-side inlet. The comparisons between the numerical results and experimental data indicated that there were some discrepancies at the initial steady state conditions, however, the numerical results followed the experimental trends well and the two were in good agreement for the final steady state, as shown in Figure 5-33. Compared to the experimental results, the PCHE helium outlet temperature differences for the initial and final steady state had deviations of 6.5 and 2.6%, respectively.

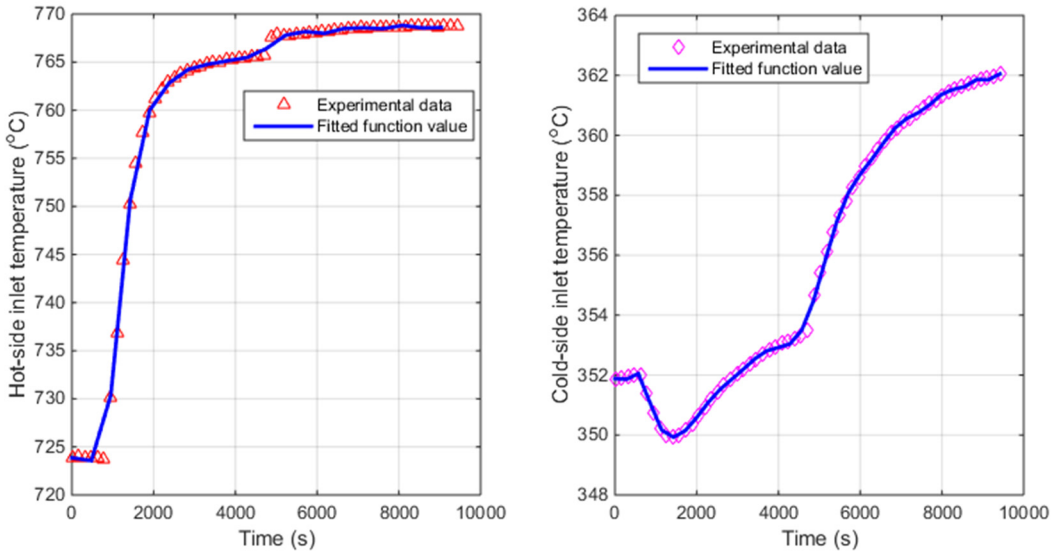

Figure 5-31. Measured hot-side and cold-side helium inlet temperature profiles for Case 3 and their fitted function curves.

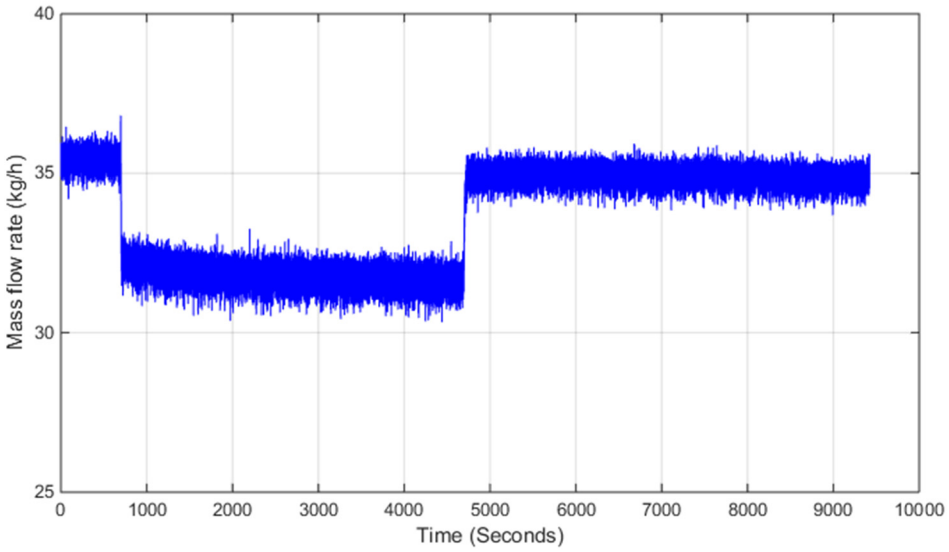

Figure 5-32. Measured helium mass flow rate step changes for Case 3.

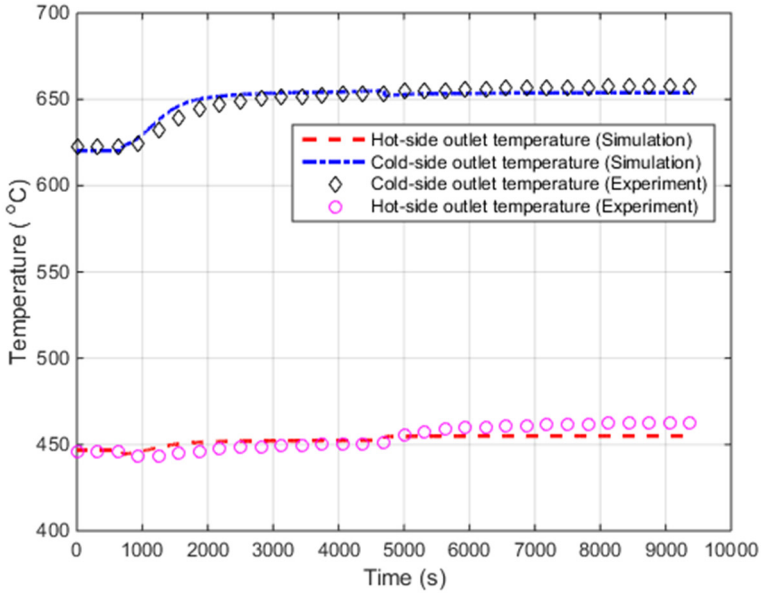

Figure 5-33. Comparisons of the helium outlet temperature profiles in Case 3: Measurements vs. predictions.

Based on the above three experimental transient tests, the close agreement of the numerical results with the experimental data was achieved. Although there were some discrepancies, it is seen that the numerical solutions are sufficiently accurate, and that feasibility of the dynamic model

developed for predicting the steady-state and transient performance of the reduced-scale zigzag PCHE is confirmed.

5.7 Conclusion

In the current study, a verified dynamic model was used to predict both the steady-state and transient behaviors of the reduced-scale straight-channel and zigzag-channel PCHEs with the prototypic designs intended for high-temperature gas-cooled nuclear reactor applications. Steady-state experimental testing of the straight-channel PCHE was conducted to obtain the heat transfer correlations using a direct method and an indirect method. Both heat transfer correlations could predict the overall heat transfer coefficients well for the straight-channel PCHE. The heat transfer correlations of the zigzag-channel PCHE used in the dynamic model were adopted from Chapter 3. The steady-state temperature profiles of the fluids on the hot and cold sides and in the solid plates of both PCHEs were first obtained, which then served as the initial condition for the transient simulations. The detailed dynamic responses of both PCHEs, subject to the helium inlet temperature and helium mass flow rate step variations on both the hot and cold sides, were simulated using the dynamic model. The simulation results appear reasonable. Two and three sets of transient tests were experimentally carried out in the HTHF to examine the dynamic performance of the straight-channel PCHE and the zigzag-channel PCHE, respectively, and to assess feasibility of the dynamic model for both PCHEs. Comparisons of the numerical solutions with the experimental results clearly indicated that the dynamic model did a reasonable job in predicting the experimental transient scenarios. Feasibility of the dynamic model for the straight-channel and zigzag-channel PCHE simulations was confirmed in this study. In addition, both the

numerical and experimental studies provided some insights into the dynamic performance of the PCHEs and could lead to the development of control strategies for PCHEs in an integrated high-temperature nuclear reactor system with both power conversion unit and process heat applications.

Chapter 6 A PCHE for FHR Applications

6.1 Overview

In this study, a dynamic system model is developed to simulate transient behavior of a prototypic 20-MW_{th} FHTR coupled with a fluted-tube heat exchanger as an IHX and a PCHE as an SHX. The model consists of a series of differential conservation equations that can be numerically solved using the MATLAB platform. Detailed geometrical designs of each component in the FHTR are determined based on the FHTR nominal operation conditions. Three initiating events are simulated in this study, including a positive reactivity insertion, a step increase in the helium mass flow rate to the SHX cold side, and a step increase in helium inlet temperature to the SHX cold side.

6.2 FHTR System Description

The Fluoride salt-cooled High-temperature Reactors (FHRs) combine the coated particle fuel and graphite moderator with a liquid fluoride salt as the coolant for electricity generation and process heat applications. The high volumetric heat capacity of these fluoride salts provides potential for a higher power density than the gas-cooled reactors and enables a compact reactor system. In addition, the FHR is designed to employ a fully passive decay heat removal system and a high-efficiency Brayton power cycle (MIT et al., 2013 and Lv, 2016). Figure 6-1 shows a schematic of an FHR that is coupled to a helium Brayton cycle system through an intermediate loop. In this

FHR design, it adopts a cylindrical core with uniformly distributed fuel pebbles. The intermediate loop draws an intermediate loop, consisting of an IHX and an SHX, to link the primary system with the power conversion unit. The working fluids used in the reactor primary system and intermediate loop are FLiBe and FLiNaK, respectively. Both salt mixtures have good heat transfer capability and a low melting point. The thermos-physical properties of FLiBe and FLiNaK are summarized in Table 6-1 (Williams et al., 2016).

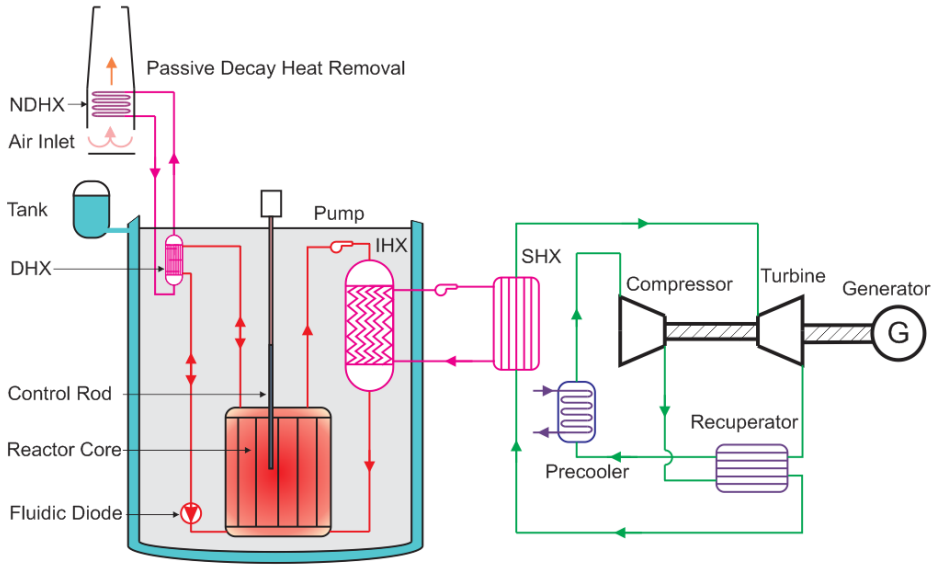

Figure 6-1. Schematic of an FHR coupled to a PCU through an intermediate loop.

Table 6-1. Thermo-physical properties of FLiBe and FLiNaK (T in Kelvin).

	FLiBe	FLiNaK
Melting point (°C)	458	454
Density (kg/m^3)	$2,280 - 0.4884\left(T - 273\right)$	$2,530 - 0.73\left(T - 273\right)$
Specific heat (J/kg-°C)	2,380	1,883
Viscosity (cP)	$0.116\exp\left(\frac{3,755}{T}\right)$	$0.04\exp\left(\frac{4,170}{T}\right)$
Thermal conductivity (W/m-°C)	$0.0005T + 0.6297$	$0.0005T + 0.4348$

Direct reactor auxiliary cooling system (DRACS) is a passive heat removal system that has been proposed for FHRs (Galvez, 2011 and Lv, 2016). The DRACS has two sets of heat exchangers, namely, DRACS heat exchanger (DHX) and natural draft heat exchanger (NDHX), as shown in Figure 6-1. The DHX is submerged in the primary coolant inside the reactor vessel and the NDHX is placed inside the air chimney. The DRACS consists of three coupled natural circulation (natural convection) loops relying completely on buoyancy as the driving force. The primary salt flow into the DRACS is restricted under reactor normal operations by means of a fluidic diode, which has large flow resistance in its reverse flow direction, i.e., the upward direction as shown in Figure 6-1. As a result, only a small amount of the liquid salt goes into the DRACS to prevent the DRACS secondary salt from overcooling, ensuring the DRACS can function promptly after reactor shutdown. The PCU is a closed-loop helium Brayton cycle that could provide a higher power conversion efficiency compared to a steam Rankine cycle. It should be noted that one of the FHTR design requirements is to deliver thermal power for a variety of applications, such as process heat for hydrogen generation and refineries. In that configuration, the process heat application plants are also coupled to the primary reactor system through an intermediate loop. Therefore, in modeling the behavior of an FHTR integral system, it becomes essential to consider the primary reactor system, DRACS, intermediate loops, PCU, and process heat application plants. In our current study, the main propose is to examine the behavior of the intermediate loop. The DRACS and process heat application plant were however not considered. To develop the dynamic system model for simulating the transient characteristics of a prototypic 20-MW_{th} FHTR, a point neutron kinetics model was adopted for the reactor. In addition, a fluted tube heat exchanger and a printed circuit heat exchanger with offset-strip fins were selected as the IHX and SHX for the FHTR, respectively.

6.3 Mathematical Modeling

6.3.1 Reactor core model

The FHTR has a cylindrical core with uniformly distributed pebble fuel (Zwaan et a., 2007). During the reactor normal operation, the primary coolant was assumed to flow from the bottom of the core to the top with a temperature rise from 600 to 704 °C through the reactor core. A simplified one-dimensional model was adopted to simulate the core, which was axially divided into a number of segments with a prescribed power distribution. It was assumed that the reactor was under perfect thermal insulation and that the heat loss to the surroundings was therefore neglected. The entire fuel was considered as a whole and hence the pebble fuel only transferred heat to the coolant by forced convection while the heat transfer between the fuel pebbles and from the pebbles to the coolant by radiation were neglected. The radial temperature distribution at each elevation in the core would be flattened during a small-time interval. The heat conduction from the core to the peripheral structural materials during a transient was also neglected. Therefore, the heat conduction in the radial direction was not considered. These assumptions were considered reasonable because the heat transfer from the pebble fuel to the coolant was dominated by forced convection. In addition, these were conservative assumptions, so the results that were obtained from the simplified calculations would give an underestimation of the heat transfer capacity of the coolant.

For energy conservation in the pebble fuel,

$$\rho_{pb} c_{p,pb} \frac{\partial T_{pb}\left(z,t\right)}{\partial t} = \frac{\partial}{\partial z}\left[k_{pb}\left(z,t\right)\frac{\partial T_{pb}\left(z,t\right)}{\partial z}\right] + \dot{q}_n^{'''}\left(z,t\right), \tag{6.1}$$

$$\dot{q}_c\left(z,t\right) = h_f A_R\left[T_{pb}\left(z,t\right) - T_f\left(z,t\right)\right], \tag{6.2}$$

where T_{pb} is the pebble fuel temperature; T_f is the primary coolant temperature; $\rho_{pb} c_{p,pb}$ is the volumetric heat capacity of the pebbles; k_{pb} is the pebble thermal conductivity; $\dot{q}_n^{'''}$ is the internal energy generation rate density due to fission; $\dot{q}_c$ is the heat transfer rate via convection; h_f is the heat transfer coefficient between the pebbles and primary coolant; and A_R is total heat transfer area in one computational segment in the reactor core. The subscripts *pb* and *f* denote the pebble fuel and primary coolant, respectively.

For energy conservation in the primary coolant,

$$m_f c_{p,f} \frac{\partial T_f\left(z,t\right)}{\partial t} + \dot{m}_f c_{p,f}\left[T_f^{out}\left(z,t\right) - T_f^{in}\left(z,t\right)\right] = \dot{q}_c\left(z,t\right), \tag{6.3}$$

where m_f is the coolant mass in one computational node; $c_{p,f}$ is the coolant specific heat; and $\dot{m}_f$ is the coolant mass flow rate. For fluoride salt flow into the pebble bed, the Wakao correlation (Wakao and Kaguei, 1982) was used to calculate the Nusselt number as,

$$\mathrm{Nu} = 2 + 1.1\,\mathrm{Re}^{0.62}\,\mathrm{Pr}^{0.33}, \tag{6.4}$$

where Nu, Re, and Pr are the Nusselt number, Reynolds number, and Prandtl number, respectively. This correlation is applicable for $15 \le \mathrm{Re} \le 8,500$.

The pressure drop across the pebble bed can be obtained by using the Ergun equation (Zwaan et a., 2007),

$$\Delta p = \frac{1-\varepsilon}{\varepsilon^3}\left(170\frac{\mu A_c}{\dot{m}_f d_p}(1-\varepsilon)+1.75\right)\frac{L}{d_p\rho}\left(\frac{\dot{m}_f}{A_c}\right)^2, \tag{6.5}$$

where ε, μ, ρ and $\dot{m}_f$ are the volume fraction, dynamic viscosity, density, and mass flow rate of the primary coolant, respectively, while L, A_c, and d_p denote the height of active region of the reactor core, the cross-sectional area of the reactor core, and the fuel pebble diameter, respectively.

The negative reactivity feedback to the reactor core caused by the fuel temperature was modeled using the one-group point kinetic equation (Duderstadt and Hamilton, 1976) as,

$$\frac{\mathrm{d}n(t)}{\mathrm{d}t} = \frac{\left[R(t)-\beta\right]}{\Lambda}n(t)+\lambda C, \tag{6.6}$$

$$\frac{\mathrm{d}C}{\mathrm{d}t} = \left(\frac{\beta}{\Lambda}\right)n(t)-\lambda C, \tag{6.7}$$

where n is the neutron density; C is the concentration of neutron precursor; β is the delayed neutron fraction; λ is the decay constant; and Λ is the mean neutron generation time. The total fission power of the reactor can be calculated from the neutron density.

The fuel Doppler effect and primary coolant temperature feedback were considered in this model. Neutron poisons that would provide a long-time burn-up reactivity control were neglected at this point. The total reactivity can be expressed as,

$$R(t) = R_0 + R_{CR} + F_{pb}\left[\bar{T}_{pb}(t)-\bar{T}_{pb}(0)\right]+F_f\left[\bar{T}_f(t)-\bar{T}_f(0)\right], \tag{6.8}$$

where R_0 is the initial reactivity; R_{CR} is the control rod reactivity; F is the negative feedback coefficient; $\bar{T}$ is the mass weighted temperature in the core, and $\bar{T}(0)$ is the reference temperature.

6.3.2 Heat exchanger model

a. Intermediate heat exchanger

Fluted tube heat exchanger (FTHX), a shell-and-tube type heat exchanger, was selected as the IHX for the FHTR due to its favorable heat transfer enhancement with good pressure drop characteristics. Instead of using plain tubes, FTHX uses spirally-fluted tubes to induce a swirling flow to increase the heat transfer rate. It also adopts a baffle-free design to reduce the vibration and fouling inside the heat exchanger. Figure 6-2 (a) and Figure 6-2 (b) show a side-view image and a cross-sectional schematic of a four-start spirally fluted tube, respectively. The swirling flow pattern on the shell and tube sides leaves no stagnant areas where the surface is vulnerable to fouling. This flow pattern would also help reduce the pressure drop and enhance the heat transfer in the heat exchanger. In the baffle-free design, each tube is firmly and frequently supported by its adjacent flutes. This design is protected against flow-induced vibrations (Dhahran, 2007). Since fouling could be a serious issue in FHRs due to the potentially highly corrosive fluoride salts under high temperatures, FTHX was therefore proposed as the IHX for the FHTR.

(a) Side-view image (b) Cross-section schematic

Figure 6-2. A four-start spirally fluted tube.

Extensive thermal hydraulic investigations of FTHXs were conducted by Christensen and Garimella (Garimella and Christensen, 1995). The IHX operates under a FLiBe-to-FLiNaK environment with the primary salt FLiBe on the tube side and FLiNaK on the shell side. The detailed design parameters of the IHX can be obtained by following a design procedure developed by Garimella (Garimella, 1990). The correlations that were used in this study are listed in the following.

For the shell side:

$$\mathrm{Nu} = \left[\frac{\left(f_f / 8 \right) \mathrm{Re}\,\mathrm{Pr}}{1 + 9.77\sqrt{f_f / 8}\left(\mathrm{Pr}^{2/3} - 1 \right)} \right] \left(\mathrm{Re}^{-0.20}\, e^{*-0.32}\, p^{*-0.28}\, r^{*-1.64} \right), \tag{6.9}$$

where the friction factor f_f is given as,

$$f_f = \frac{96 r^{*0.035}}{\mathrm{Re}} \left(1 + 101.7\,\mathrm{Re}^{0.52}\, e^{*1.65+2.00\theta^*} r^{*-5.77} \right). \tag{6.10}$$

For the tube side:

$$\mathrm{Nu} = 0.014\,\mathrm{Re}^{0.842}\, e^{*-0.067}\, p^{*-0.293}\, \theta^{*-0.705}\, \mathrm{Pr}^{0.4}, \tag{6.11}$$

where e^* and p^* are the dimensionless flute depth and pitch obtained by using the volume-based fluted tube inner diameter, respectively. θ^* is the non-dimensional helix angle with respect to 90° and r^* is the ratio of the volume-based fluted tube outer diameter to the shell inner diameter. From the chart that was presented by Garimella (Garimella, 1990), these correlations were validated for $300 < \mathrm{Re} < 800$. The Reynolds number can be calculated as,

$$\mathrm{Re} = \frac{\rho v D_{\mathrm{FTHX}}}{\mu}, \tag{6.12}$$

where ρ, μ and v denote the fluid density, fluid dynamic viscosity and flow velocity. The hydraulic diameter D_{FTHX} is given by,

$$D_{\mathrm{FTHX}} = D_o - D_{vo}, \tag{6.13}$$

where D_o and D_{vo} are the inner diameter of the outer plain tube and the volume-based fluted tube outer diameter, respectively.

The dynamic model to evaluate the performance of the FTHX-type IHX design was developed based on the energy balance equations for the straight-channel PCHE described in Chapter 5. The following assumptions were made for FTHX: (1) The heat loss in the piping systems was assumed negligible; (2) The heat conductions in the fluted tubes and working fluids in the flow directions were assumed negligible; (3) Heat loss to the surroundings via the heat exchanger shell was neglected; (4) Constant specific heat was used; and (5) The heat conduction resistance due to the wall could be neglected because of the thin wall and large thermal conductivity of the wall material.

b. Secondary heat exchanger

A PCHE with offset-strip fins (OSFs) was selected as the SHX type in the system dynamic model. Flow channels with offset-strip fins help interrupt the flow from becoming fully developed and thereby restarting the boundary layers, which can significantly increase the heat transfer coefficient (Losier et al., 2007). Figure 6-3 shows a schematic of one geometric unit cell, illustrating the offset-strip-fin concept.

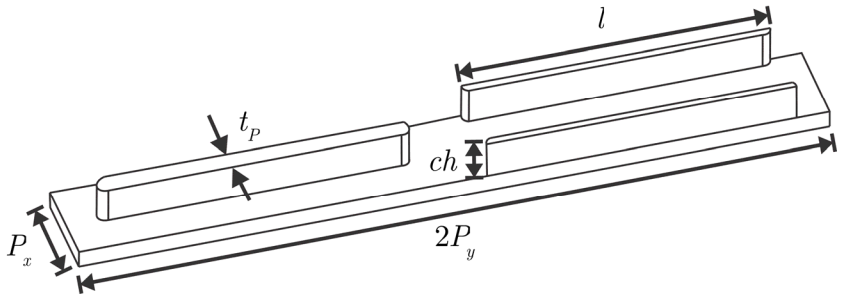

Figure 6-3. One geometric unit cell of the plate with the offset-strip fins.

The SHX operates under a FLiNaK-to-helium condition. FLiNaK is on the hot side and high-temperature, high-pressure helium is on the cold side. Correlations were developed in the literature to evaluate the heat transfer coefficient of offset-strip-fin heat exchangers. The correlation showed in Equation (6.14) is for calculating the Colburn factor, j, developed by Manglik and Bergels (Manglik and Bergels, 1995) for the offset-strip-fin heat exchangers, was used in the current study.

$$j = 0.6522\,\mathrm{Re}^{-0.5403}\,\alpha^{-0.1541}\delta^{0.1499}\gamma^{-0.0678}\left(1+5.269\times10^{-5}\,\mathrm{Re}^{1.34}\,\alpha^{0.504}\delta^{0.456}\gamma^{-1.055}\right)^{0.1}, \quad (6.14)$$

where $\alpha = \left(P_x - t_P\right)/ch$, $\delta = t_P / l$ and $\gamma = t_P / (P_x - t_P)$. As shown in Figure 6-3, ch is the fin height; t_P is the fin thickness; P_x and P_y are the pitch in the span-wise direction and stream-wise direction,

respectively; and l is the fin length. This correlation is valid for $120 < \mathrm{Re} < 10^4$ and $0.5 < \mathrm{Pr} < 15$. The heat transfer coefficient h can be obtained from the Colburn factor as,

$$h = \frac{\mathrm{Nu} k_f}{D_{\mathrm{OSF}}} = j\left(\mathrm{Re}\,\mathrm{Pr}^{1/3}\right)\frac{k_f}{D_{\mathrm{OSF}}}, \tag{6.15}$$

where k_f is the thermal conductivity of the fluid and D_{OSF} is the channel hydraulic diameter of the OSF.

The dynamic model of the SHX is the same model that was proposed for the zigzag-channel PCHEs as introduced in Chapter 5 since the SHX could be treated as a two-stream countercurrent heat exchanger as well. Similarly, to account for the complex fin geometry inside the heat exchanger, a parameter called surface area density was also introduced in the dynamic model. The fin efficiency η_f is a function of the convective heat transfer coefficient and is written as,

$$\eta_f = \frac{\tanh\left(\phi\frac{ch}{2}\right)}{\left(\phi\frac{ch}{2}\right)}, \phi \approx \left(\frac{2h}{k_P t_P}\right)^{\frac{1}{2}}, \tag{6.16}$$

where k_P is the thermal conductivity of the plate material.

6.4 Steady-State Design and Operation Parameters

To predict the dynamic behavior of the FHTR, steady-state operation parameters were calculated first by assuming constant fluid properties. The design parameters of the FHTR are summarized in Table 6-2. The active core height and radius were obtained from one of the FHTR reference designs (MIT et al., 2013). The required pumping power over the core was about 393.2 W, which

can be neglected compared with the total reactor thermal power. The primary coolant temperature profile from the bottom to the top along the axial direction in the reactor core was obtained by dividing the core into 50 segments, as shown in Figure 6-4.

Table 6-2. Reactor core steady-state operating parameters (MIT et al., 2013).

Parameter	Unit	Value
Total thermal power	MW	20
Primary coolant inlet temperature	°C	600
Primary coolant outlet temperature	°C	704
Primary nominal mass flow rate	kg/s	80.6
Fuel pebble diameter	mm	30
Bed packing fraction	-	0.61
Active core height	m	1.52
Active core radius	m	0.43
Reynolds number	-	600
Pressure drop across the reactor core	kPa	9.57
Pumping power over the reactor core	W	393.2
Convective heat transfer coefficient in the core	$W/(m^2\text{-}°C)$	9,309

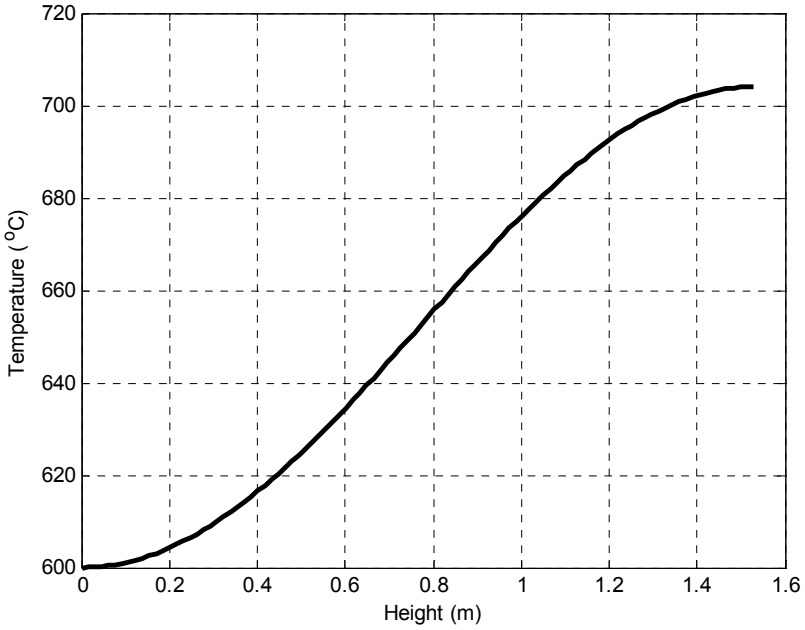

Figure 6-4. The coolant temperature profile along the axial direction in the core.

Table 6-3. Steady-state operation conditions of the IHX and SHX (Sabharwall et al., 2011).

Parameter	Unit	IHX value	SHX value
Nominal thermal duty	MW_{th}	10	
Hot-side fluid inlet temperature	°C	704	690
Hot-side fluid outlet temperature	°C	600	545
Cold-side fluid inlet temperature	°C	545	498.9
Cold-side fluid outlet temperature	°C	690	651.2

Preliminary thermal designs of both the IHX and SHX were carried out by using the conventional LMTD method. The operation conditions of the IHX and SHX are shown in Table 6-3 (Sabharwall et al., 2011). Each PCU loop was designed for a nominal thermal power of 10.0 MW. Both the IHX and SHX had a nominal thermal duty equal to the PCU power. It should be noted that these

heat exchanger designs were not necessarily optimized. Table 6-4 summarizes the IHX steady-state design parameters under plant normal operation.

Table 6-4. IHX steady-state design parameters.

Parameter	Unit	Value
Fluted tube inner bore diameter	mm	9.3
Fluted tube outside envelope diameter	mm	16.2
Fluted tube wall thickness	mm	1.0
Flute pitch	mm	6.6
Number of fluted starts	-	4
Nominal shell diameter	m	0.838
Total number of fluted tubes	-	2,332
Total heat transfer area (O.D.)	m^2	471
Tube-side Reynolds number	-	317
Shell-side Reynolds number	-	395
Tube-side fluid velocity	m/s	0.11
Shell-side fluid velocity	m/s	0.056
Tube-side heat transfer coefficient	$W/(m^2\text{-}°C)$	992
Shell-side heat transfer coefficient	$W/(m^2\text{-}°C)$	3,541
Overall heat transfer coefficient	$W/(m^2\text{-}°C)$	707
Tube length	m	5.7
Pressure drop on the tube side	kPa	2.5
Pressure drop on the shell side	kPa	6.5
Total heat exchanger volume	m^3	3.1

The fluted tube geometry was chosen in the way that these fluted tubes can actually be fabricated by a commercial vendor. The heat transfer coefficient of the shell side was much larger than that of the tube side due to the baffle-free design and relative large fluted tube diameter. Smaller tubes were not considered due to the potential fouling caused by the potentially corrosive fluoride salt. The overall power density of the IHX was approximately 3.0 MW/m^3.

Table 6-5. SHX steady-state design parameters.

Parameter	Unit	Value
Hot-side hydraulic diameter	mm	1.2
Cold-side hydraulic diameter	mm	2.2
Plate width	m	0.6
Hot-side Reynolds number	-	149
Cold-side Reynolds number	-	4,433
Hot-side fluid velocity	m/s	0.26
Cold-side fluid velocity	m/s	18.6
Hot-side Nusselt number	-	9
Cold-side Nusselt number	-	22
Hot-side heat transfer coefficient	W/(m^2-°C)	6,776
Cold-side heat transfer coefficient	W/(m^2-°C)	3,217
Overall heat transfer coefficient (based on the hot-side area)	W/(m^2-°C)	2,295
SHX flow length	m	0.5
SHX total height	m	0.97
Total number of plates	-	386
SHX volume	m^3	0.29
Pressure drop on the hot side	kPa	13.7
Pressure drop on the cold side	kPa	18.3

Table 6-5 summarizes the SHX steady-state design parameters under plant normal operation. It can be seen that the cold-side (i.e., the helium side) hydraulic diameter was about twice that of the hot side (i.e., FLiNaK side) and the cold side had a lower heat transfer coefficient than that on the hot side. The overall power density of the proposed SHX design was approximately 34.0 MW/m^3. The temperature distributions inside the heat exchangers were obtained by dividing the IHX and SHX into 100 segments along their flow lengths, as shown in Figure 6-5 and Figure 6-6. The temperatures inside the heat exchangers can serve as the initial values when starting the transient simulations.

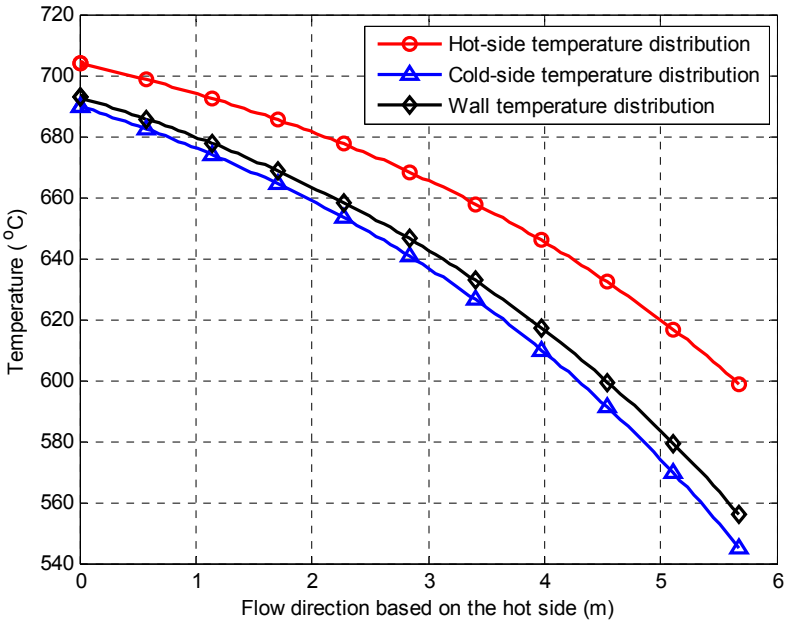

Figure 6-5. Temperature distribution inside the FTHX-type IHX.

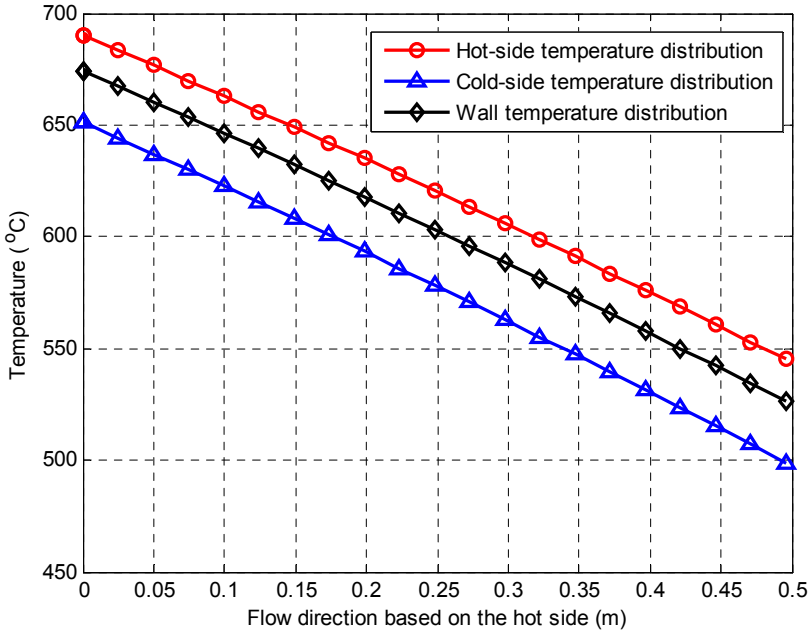

Figure 6-6. Temperature distribution inside the PCHE-type SHX.

6.5 Reactor Model Verification

For the one-group point kinetic equation, the analytical solution can be determined (Duderstadt and Hamilton, 1976). The normalized power $\dot{Q}_{Nor}$ can be written as,

$$\dot{Q}_{Nor} \cong \left(\frac{\beta}{\beta - R_0}\right)\exp\left(\frac{\lambda R_0}{\beta - R_0}t\right) - \frac{R_0}{\beta - R_0}\exp\left(-\frac{\beta - R_0}{\Lambda}t\right). \tag{6.17}$$

The numerical and analytical results were obtained for both a positive and a negative step reactivity insertion of an amount $|R_0 = 0.0025|$ into the reactor. In the numerical calculation, the time step was 0.001 second. It can be seen from Figure 6-7 and Figure 6-8, both the numerical and analytical results matched well. However, the numerical result for the positive reactivity insertion was

smaller than the analytical solution due to the truncation error from large time step in the numerical calculation.

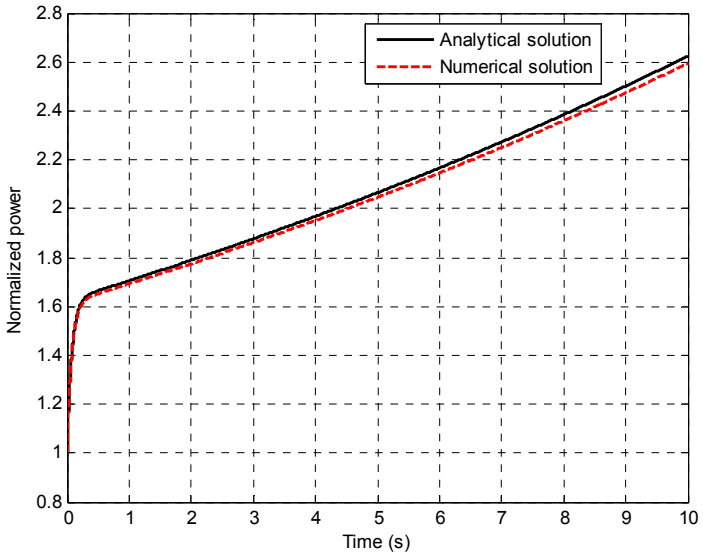

Figure 6-7. Reactor power level following a positive step reactivity insertion based on analytical and numerical results.

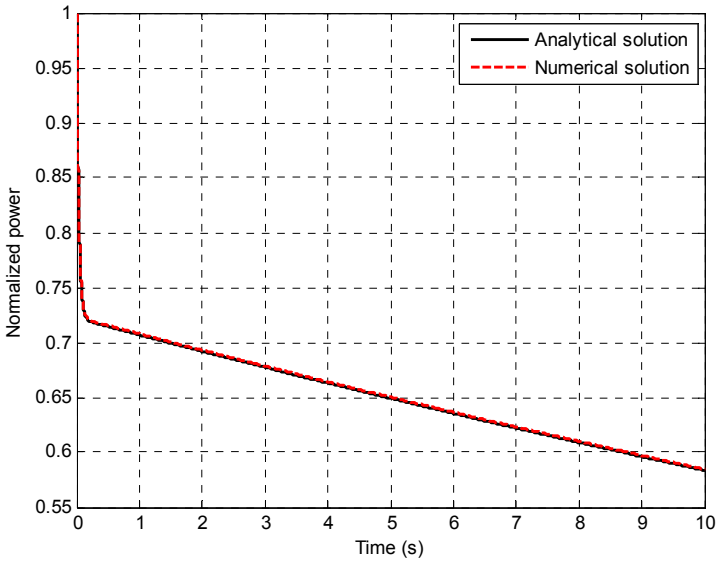

Figure 6-8. Reactor power level behavior following a negative step reactivity insertion based on analytical and numerical results.

6.6 Transient Simulations

As noted, the FHTR investigated in the current study had two identical PCUs. It was assumed that these two loops had identical thermal performance. The dynamic system model developed in the previous section was tested in this section using three transient scenarios: (1) \$0.05 reactivity step insertion; (2) 50 °C-step increase in the helium inlet temperature on the SHX cold side, and (3) 8%-step increase in the helium mass flow rate on the SHX cold side. It was also assumed that all the control and protection systems in the FHTR will not participate during these transients. The effects of these three transient scenarios were based on the temperatures at different locations in the FHTR system.

The FHTR system nodal structure used in this study is presented in Figure 6-9. Nodalization sensitivity studies were performed to determine the effective number of nodes used in this dynamic system based on a Reactivity Insertion Accident (RIA) transient. Four different numbers of nodes were used in the mesh sensitivity study. The fluid temperatures at five locations in the FHTR system were monitored after the system reached a steady-state condition following the RIA. It can be seen from Table 6-6 that these four cases presented similar results without significant deviations. In this study, the meshes with a total number of 948 nodes were selected to simulate the three transient scenarios.

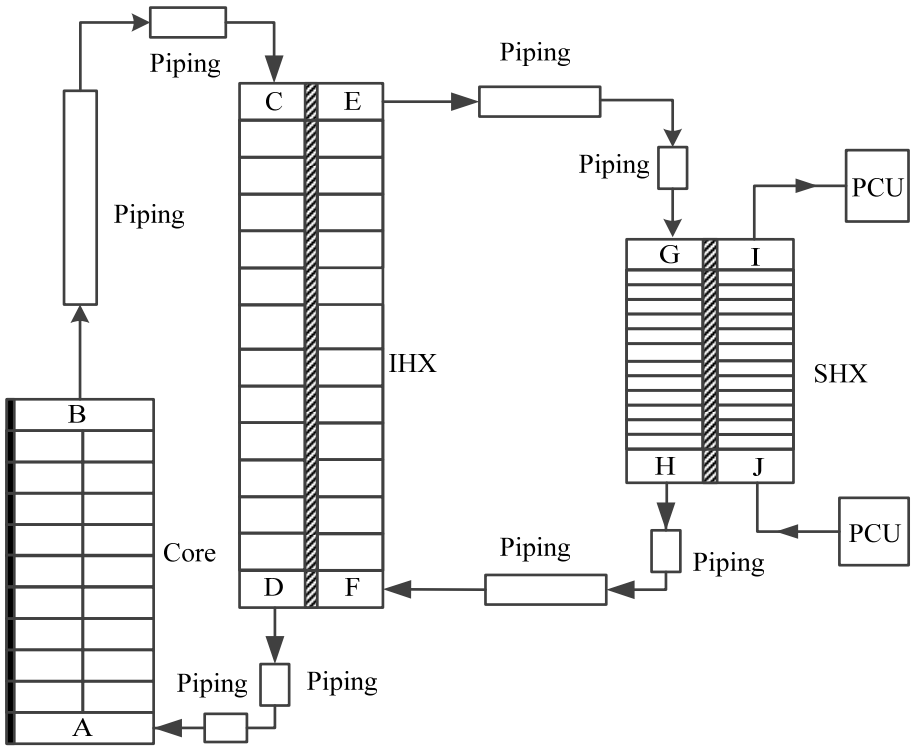

Figure 6-9. FHTR nodal structure.

Table 6-6. Results of node sensitivity study.

Type	Total number of nodes	Temperature (°C)				
		A	B	F	E	I
RIA	788	601.2	711.5	548.0	559.3	658.2
	948	601.9	711.1	547.8	559.3	658.3
	1,348	602.5	710.9	547.7	559.3	658.3
	1,748	602.7	710.8	547.7	559.4	658.3

*: A, B, F, E, & I refer to the nodes shown in Figure 6-9.

6.6.1 0.05$ reactivity step insertion

A positive reactivity insertion could be caused by lifting a control rod or a control rod ejection accident. The insertion of a positive reactivity causes an increase of the reactor power, which leads to temperature increases in the fuel and primary coolant. The negative temperature feedback brings a negative reactivity into the core, resulting in a power decrease and therefore a temperature decrease in the fuel to compensate for the temperature increase in the core. In this exercise, a positive reactivity of 0.05$ was inserted into the core at 100 seconds after the reactor operates under its full nominal power condition. Figure 6-10 shows the reactor power evolution before and after the reactivity insertion. The reactor reached the maximum power at about 190 seconds, and then started to decrease. After about 770 seconds, the reactor power reached a stable value with approximately 1 MW additional power. Figure 6-11 shows the temperature transients after the reactivity insertion. The temperature of the primary coolant at the core outlet increased after the reactivity insertion. Fluid temperatures at the IHX hot-side inlet and cold-side outlet increased fairly quickly, while the temperatures at the SHX both sides had a time delay in responding, starting to increase at around 240 seconds. This is because the piping distance between the IHX and SHX introduced a time delay into the system. Therefore, the delay time can be estimated by dividing the flow length by the flow velocity.

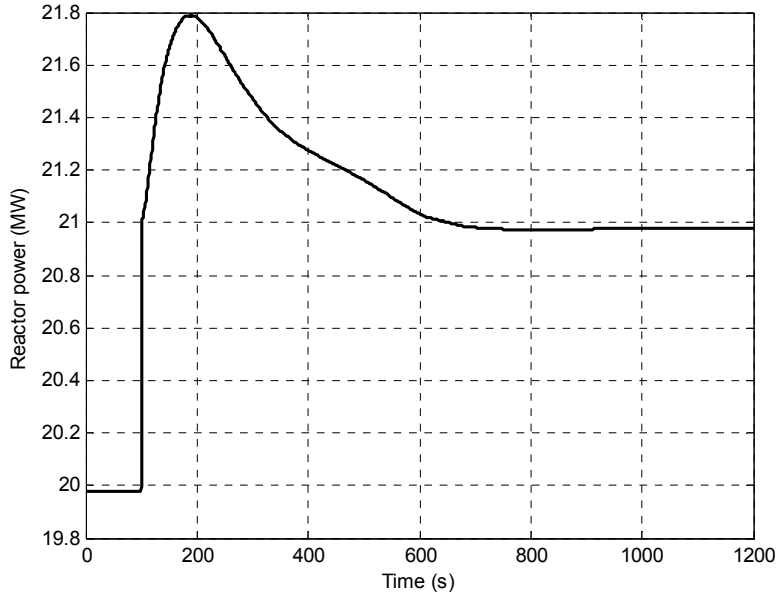

Figure 6-10. Reactor power variation after the 0.05$ reactivity insertion.

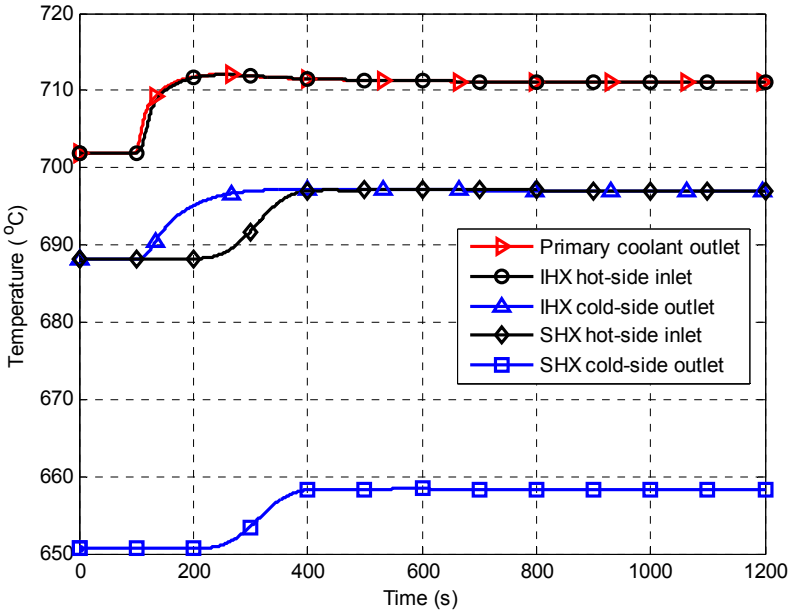

Figure 6-11. Fluid temperature variations after the reactivity insertion.

6.6.2 50 °C-step increase in the helium inlet temperature on the SHX cold side

A step increase of the helium inlet temperature on the SHX cold side at 100 seconds after the system reached its nominal steady-state condition was initiated. The increase of the helium inlet temperature caused the liquid salt temperatures in the intermediate loop to increase, as shown in Figure 6-12 and Figure 6-13. The connecting pipe between the IHX and SHX led to a delayed transient response from 100 to about 240 seconds. The reactor did not receive any disturbances within this time delay. The fluid temperature increased in the intermediate loop propagated to the reactor primary loop, increasing the reactor core coolant inlet temperature. The primary coolant temperature rose by about 22 °C at the hot side of the IHX. The increasing fluid inlet temperature rose the average temperatures of the fuel and primary coolant in the reactor core. Due to the negative feedback of the fuel and primary coolant, the power decreased because the negative reactivity was introduced into the core. It can be seen from Figure 6-14 that the nuclear reactor core responded to the increased fuel and coolant temperatures by decreasing its power and the primary coolant outlet temperature actually dropped, as shown in Figure 6-12, because of the lower power in the core. Vice versa, a positive feedback was then introduced into the core, leading to a small increase of reactor power from 540 to 1,000 seconds. It can be seen from Figure 6-14 that the reactor power finally reached a stable value with approximately a 5-MW power decrease due to the temperature step increase in helium at the SHX cold-side inlet. The decreasing fluid inlet temperature on the hot side of the IHX and the increased fluid outlet temperature on the hot side of the SHX led to temperature oscillations on the cold-side fluid inlet temperature of the IHX, as shown in Figure 6-13.

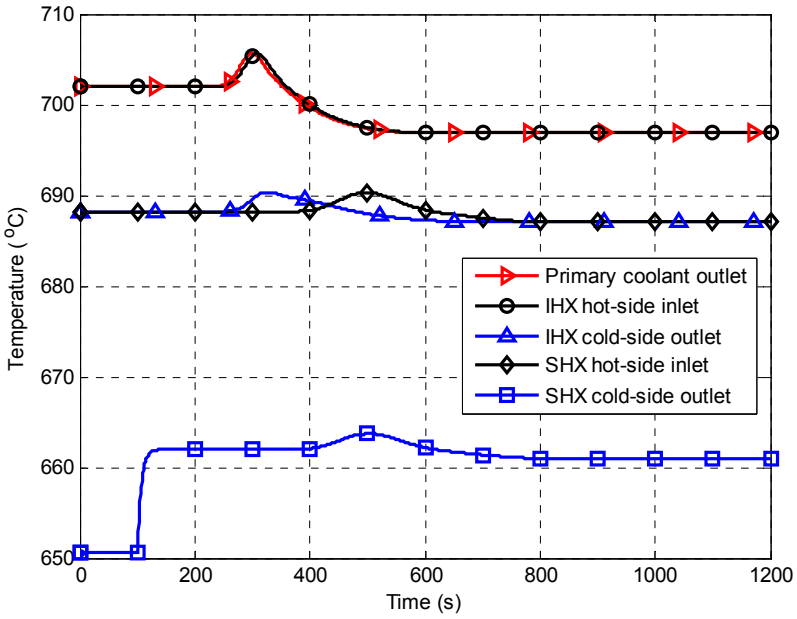

Figure 6-12. Temperature variations after a 10 °C-step increase for the helium inlet temperature on the SHX cold side.

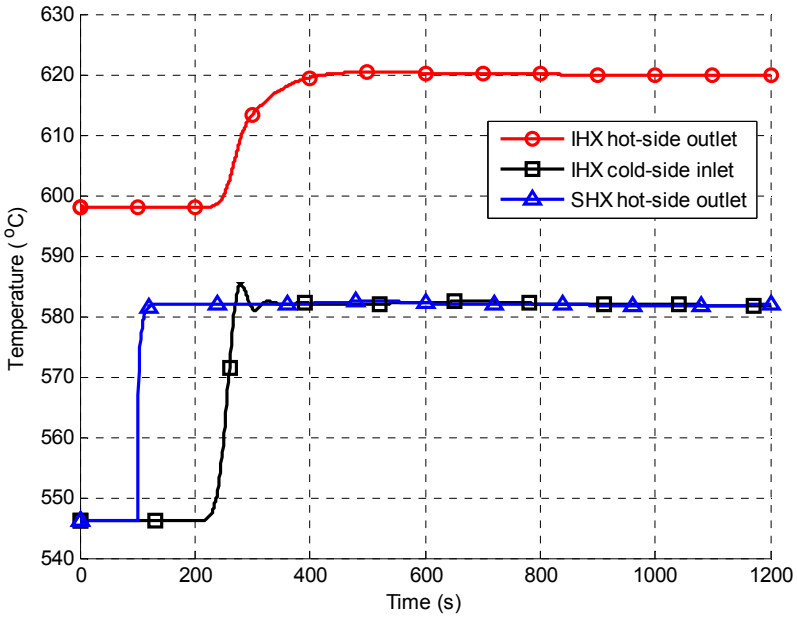

Figure 6-13. Temperature variations after a 10 °C-step increase for the helium inlet temperature on the SHX cold side.

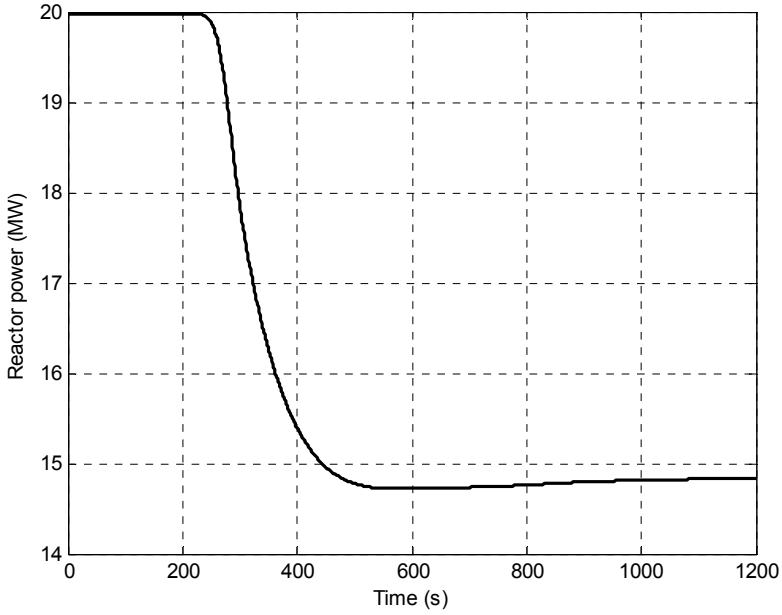

Figure 6-14. Reactor power variation after a helium temperature step increase at the SHX inlet.

6.6.3 8% helium mass flow rate step increase on the SHX cold side

When the PCU operates at its nominal condition, the helium mass flow rate is kept at a constant value. Figure 6-15 and Figure 6-16 depict the temperature variations at different locations in the FHTR following an 8%-helium mass flow rate step increase after 100-second nominal steady-state operation. The increase of the helium mass flow rate caused a reduction in the outlet temperature on the helium side. The initiating event at the inlet of the SHX cold side quickly propagated to the cold-side outlet and the hot-side outlet locations because of the high helium velocity and small helium traveling distance. The connecting pipe between the IHX and SHX introduced a delayed transient response from 100 to about 240 seconds. It can be seen from Figure 6-17 that the reactor power experienced a rapid increase starting at 240 seconds because a positive reactivity was

introduced into the reactor core by the negative temperature feedback from the fuel and primary coolant.

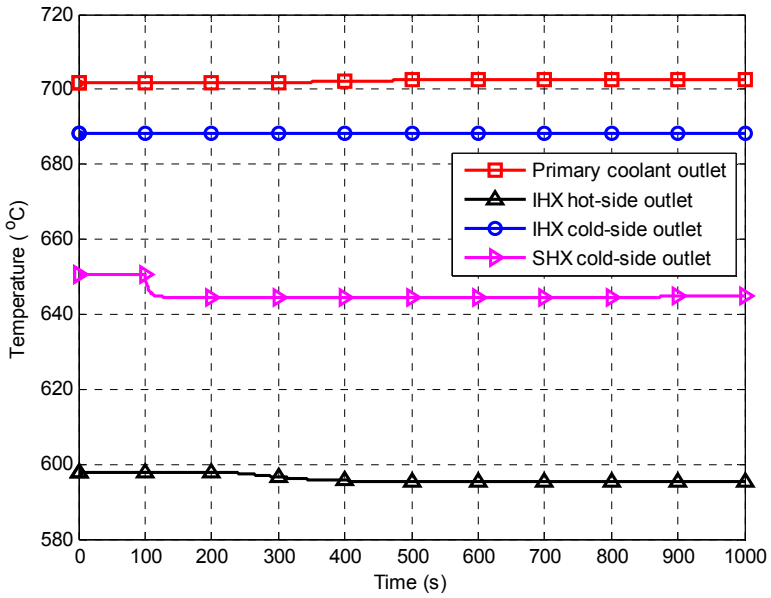

Figure 6-15. Temperature evolutions at different locations following an 8%-helium mass flow rate step increase.

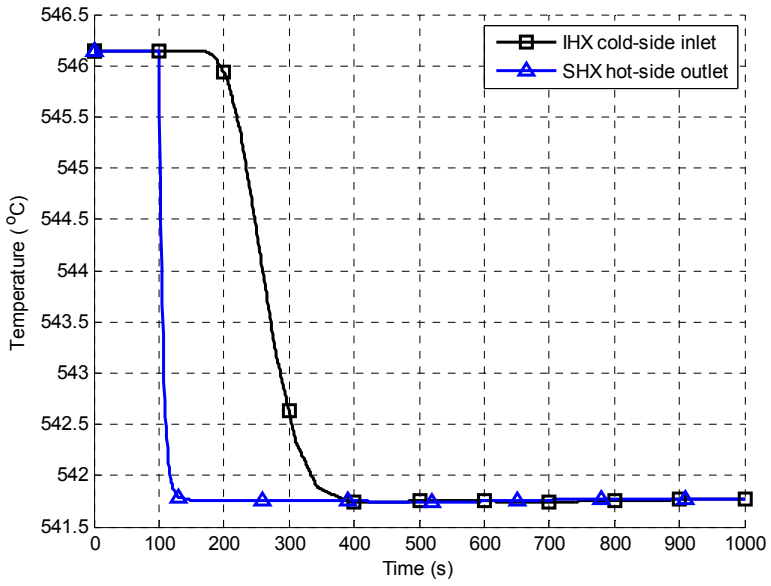

Figure 6-16. Temperature evolutions at different locations following an 8%-helium mass flow rate step increase.

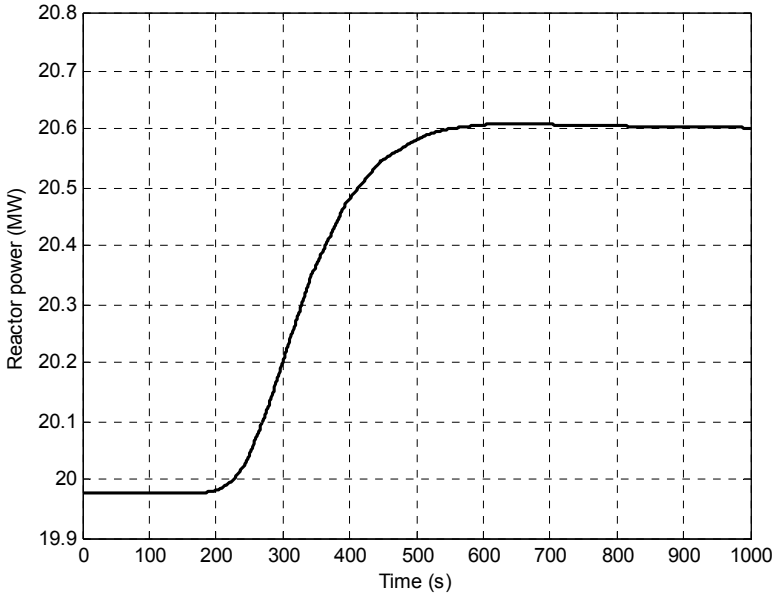

Figure 6-17. Reactor power following the helium flow rate change.

6.7 Conclusion

The design of the IHX and SHX for a two-loop, 20-MW_{th} FHTR with a helium Brayton power cycle was performed based on a thermal hydraulic analysis. The geometric parameters of each component under the nominal operation were obtained for steady-state operation. The simulation results of three initiating events, a positive reactivity insertion, a step increase of helium flow rate, and a step increase of helium inlet temperature to the SHX in the PCU, were obtained. The results demonstrated that the reactor, for the three transient scenarios analyzed, has inherent safety features. The increase of the temperatures of the pebble fuel and primary coolant was mitigated by the decrease of the reactor power due to the negative temperature feedbacks. The results also indicated the intermediate loop consisting of the IHX and SHX played an important role in the transient progression of the integral system. The traveling distance between the IHX and SHX for

the intermediate working fluid introduced some extra time for the control system to respond to the initiating events from the PCU side.

Chapter 7 Summary and Conclusions

7.1 Summary and Conclusions

The principal objectives of the current research were to investigate, both experimentally and numerically, the pressure drop and heat transfer characteristics of high-temperature diffusion-bonded compact heat exchangers for use in advanced nuclear reactor systems, and to model both the steady-state and dynamic behaviors of compact heat exchangers using the developed heat exchanger models. In the current study, a reduced-scale PCHE was fabricated using Alloy 617 plates and Alloy 800H headers. The PCHE has eight hot and eight cold plates with 11 semicircular zigzag channels with a nominal diameter of 2.0 mm in each plate. The pressure drop and heat transfer characteristics of the PCHE were investigated experimentally in a high-temperature helium test facility. The PCHE helium inlet temperatures and pressures varied up to 464 °C/2.7 MPa for the cold side and 802 °C/2.7 MPa for the hot side, respectively, while the maximum helium mass flow rates on both sides of the PCHE reached 39 kg/h. The corresponding maximum channel Reynolds number was approximately 3,558 covering the laminar flow and laminar-to-turbulent transitional flow regimes. Both steady-state and transient tests were conducted. In addition, transient analyses of an FHTR coupled with a helium Brayton cycle via an FTHX-type IHX and a PCHE-type SHX were performed. The summary and major conclusions arrived at in the current research are listed as follows:

(1) A one-dimensional code for the heat exchanger thermal design was developed. The fluid's thermophysical properties changed along the fluid flow direction, resulting in a non-uniform heat transfer coefficient. The conventional LMTD method did not account well for the variations of fluid's thermophysical properties, which could potentially lead to large discrepancies in the heat exchanger thermal design. The developed one-dimensional code could capture the fluid and solid properties at any specified location. Compared to the LMTD method, the developed one-dimensional code showed higher heat exchanger thermal design and rating accuracy.

(2) One reduced-scale zigzag-channel PCHE was fabricated using Alloy 617 plates for the heat exchanger core and Alloy 800H pipes for the heat exchanger headers. The fabrication techniques and fabrication aspects of the PCHE were described.

(3) Thermal-hydraulic performance of the reduced-scale zigzag-channel PCHE was investigated experimentally in a high-temperature helium test facility. The maximum PCHE test temperature reached was 802 °C. The zigzag-channel Fanning friction factors were two to three times those found in straight circular pipes in the laminar flow regime and about two times greater than those found in the transitional flow regime. New pressure drop and heat transfer correlations for the zigzag-channel PCHE were developed based on the experimental data. A comparison between the available correlations with the proposed correlations showed that the available correlations underpredicted heat transfer performance of the current PCHE. When compared to the performance of straight circular pipes, PCHEs with zigzag channels showed superior heat transfer performance.

(4) A CFD software package, STAR-CCM+, was used to simulate the thermal-hydraulic performance of the fabricated PCHE with a simplified geometry model. Comparisons between the experimental data and the CFD simulation results showed some discrepancies between the obtained experimental data and numerical results, which may have been caused by the different thermal boundary conditions, as well as potential distortion of flow channels due to diffusion bonding. Local thermal-hydraulic performance analyses indicated that fully-developed flow and thermal boundary conditions were not observed, which was attributed to the wavy nature of the zigzag flow channels as well as the temperature variations along the flow channels, resulting in large fluid property variations.

(5) A number of effects on the PCHE's thermal-hydraulic performance were studied, including the fluid and solid thermophysical properties, radius of the curvature at zigzag bends, channel configuration, channel pitch length, and zigzag angle. In addition, in the simplified heat exchanger simulation model, the cross section of the flow channel was divided into eight segments to identify the thermal boundary conditions for the zigzag-channel PCHE. The temperature and heat flux distributions along the fluid flow direction for all segments were obtained. It was observed that the temperatures were not constant along the azimuthal direction of a channel cross section. Also, the temperature distribution for each segment along the flow direction presented a wavy shape. However, global temperature distributions along the entire channels were approximately linear. As for the heat flux distributions, although they varied significantly from segment to segment, the heat flux trend for each segment along the helium flow direction was similar.

(6) Based on the developed Nusselt number and Fanning friction factor correlations in this study, NSGA-II was utilized to optimize the PCHE's geometry. A population size of 6,000 was run and a total number of 142 points on the Pareto front were obtained. The manufacturers and users could select the optimal geometrical parameters for zigzag-channel PCHEs from the obtained Pareto front based on their considerations.

(7) A dynamic model verified using a commercial software tool was proposed to predict both the steady-state and transient behaviors of the reduced-scale straight-channel and zigzag-channel PCHEs. Steady-state experimental testing was conducted to obtain the heat transfer correlations for the straight-channel PCHE using a direct method and an indirect method. The detailed dynamic responses of both PCHEs, subject to the helium inlet temperature and mass flow rate variations on both the hot and cold sides, were simulated and analyzed using the dynamic model, and the simulation results appeared reasonable. Two and three sets of transient tests were experimentally carried out to examine the dynamic performance of the straight-channel PCHE and the zigzag-channel PCHE, respectively, and to assess feasibility of the dynamic model. Comparisons of the numerical solutions and experimental results clearly indicated that the dynamic model did a reasonable job in predicting the experimental transient scenarios.

(8) A PCHE with offset-strip fins and a fluted-tube heat exchanger were used to couple a 20-MW_{th} FHTR with a helium Brayton power cycle, which served as the SHX and IHX, respectively. The heat exchanger dynamic model was implemented into the developed system dynamic code. The simulation results of three initiating events, a positive reactivity insertion, a step increase of helium flow rate, and a step increase of helium inlet temperature to the SHX, were obtained. The results

demonstrated that the FHTR reactor, for the three transient scenarios analyzed, had inherent safety features. The increase of the temperatures of the pebble fuel and primary coolant was mitigated by decreased reactor power due to the negative temperature feedbacks. The results also indicated that the intermediate loop consisting of the IHX and SHX played a significant role in the transient progression of the integral system. The traveling distance between the IHX and SHX for the intermediate working fluid provided some extra time for the control system to respond to the initiating events from the power conversion unit side.

Upon the completion of this research work, many contributions have been obtained for PCHEs in advanced nuclear reactor applications. PCHEs are used for efficient transferring of heat from one side to another side. They can be used in other areas since they have high effectiveness, high-temperature and high-pressure application capability, and space and weight savings. PCHEs have been extensively used in offshore and chemical industries and have promising applications in nuclear power and solar thermal power plants. Other areas of application include but not limit to cooling of electronics, dual cycles for process heat industry, cooling for fuel cells, and mixer reactors. Both experimental and numerical investigations of PCHEs in the current study provide critical insights on performance of zigzag-channel PCHEs, which can be applied to the above-mentioned areas.

7.2 Future Work

Significant effort will still be required for PCHEs to be employed in advanced nuclear reactors in the near future. Some of the future work that needs to be accomplished on PCHEs are proposed as follows:

(1) In the present study, only four fluid temperatures, i.e., the cold-side inlet and outlet temperatures and the hot-side inlet and outlet temperatures, and one mass flow rate (equal mass flow rate for both the hot and cold sides) for the heat exchanger testing were obtained from the experiments. The heat transfer coefficients obtained based on the four fluid temperatures and flow rate were the overall heat transfer coefficients. Local heat transfer coefficients were not obtainable due to a lack of internal temperature measurements. Also, the differential pressure measurements included pressure losses in the headers and flow distribution channels, which could lead to large uncertainties during experimental data reduction to obtain pressure loss for flow channels. Therefore, internal temperature and pressure measurements are recommended in future heat exchanger testing.

(2) Header design is an intractable issue in terms of fabrication and flow distribution. During the header fabrication process, it is essential to consider channel blockage and channel crosstalk. On the other hand, the flow to be directed into the channels should not experience a large pressure loss between the headers and channel inlets. A more effective way of fabricating the headers needs to be further developed.

(3) The stress analysis for PCHEs is an important aspect for determining the lifetime of PCHEs for use in advanced nuclear reactors. Experimental studies and validation of the full inelastic finite

element analysis for diffusion-bonded compact heat exchangers are required. Tensile, creep, fatigue, and creep-fatigue tests need to be conducted to determine the mechanical properties of the diffusion bonds. Advanced models that test the qualifications of PCHEs for nuclear applications must also be developed.

(4) Although a comprehensive CFD study was conducted, it only tested PCHEs with zigzag flow channels under high-temperature helium fluid conditions. For other channel shapes, such as S-shape fins, offset-strip fins, and airfoil fins, each with different configurations and fluid combinations, a similar methodology should be applied to improve the existing and/or develop new correlations for innovative PCHE designs.

(5) A PCHE could have many channel shapes and channel configurations for various fluid combinations. It would be beneficial to utilize the high-temperature helium test facility, supercritical carbon dioxide loop, and high-temperature fluoride salt test facilities available in the author's laboratory to test prototypical PCHEs with different geometries under different fluid combinations, such as helium to molten salt and molten salt to sCO_2. In addition to thermal-hydraulic testing, the effects of fouling in PCHEs must also be studied.

(6) For the transient analysis of an FHR coupled with a helium Brayton cycle via an FTHX and a PCHE, more transient scenarios could be investigated, including a loss-of-coolant accident and those due to failure in the PCU and/or process heat application plants, to better understand the integral behaviors of the coupled reactor, power conversion system, and process heat application

plants. Similar methodology could also be applied to an FHR coupled with an sCO_2 Brayton power cycle.

Bibliography

Abrams, B., Levy, S., and Chapin, D., "A Technology Roadmap for Generation IV Nuclear Energy Systems," In U.S. DOE Nuclear Energy Research Advisory Committee and the Generation IV International Forum, 2002.

Allen, D.M., "Photochemical Machining: from 'Manufacturing's Best Kept Secret' to a $6 Billion per Annum, Rapid Manufacturing Process," CIRP Annals-Manufacturing Technology, 53, pp. 559-572, 2004.

Aneesh, A.M., Sharma, A., Srivastava, A., Vyas, K.N., and Chaudhuri, P., "Thermal-Hydraulic Characteristics and Performance of 3-D Straight Channel Based Printed Circuit Heat Exchanger," Applied Thermal Engineering, 98, pp. 474-482, 2016.

ASME Boiler and Pressure Vessel Committee on Materials, "2015 ASME Boiler & Pressure Vessel Code," Section II Materials, Part A, 2015.

Baik, S., Kim, S.G., Lee, J., and Lee, J.I., "Study on CO_2-Water Printed Circuit Heat Exchanger Performance Operating under Various CO_2 Phases for SCO_2 Power Cycle Application," Applied Thermal Engineering,113, pp. 1536-1546, 2017.

Bartel, N., Chen, M., Utgikar, V.P., Sun, X., Kim, I.H., Christensen, R.N., and Sabharwall, P., "Comparative Analysis of Compact Heat Exchangers for Application as the Intermediate Heat Exchanger for Advanced Nuclear Reactors," Annals of Nuclear Engineering, 81, pp. 143-149, 2015.

Bartel, N., Utgikar, V., Sabharwall P., Chen, M., Sun, X., Christensen, R.N., and Kim I.H., "Thermal-Hydraulic Design of Wavy-Channel Printed Circuit Heat Exchanger for Advanced Reactors," Transactions of the American Nuclear Society, 108, pp. 1086-1089, 2013a.

Bartel, N., Utgikar, V., Sabharwall P., Chen, M., Sun, X., Christensen, R.N., and Kim I.H., "Transient Model of Wavy-Channel Printed Circuit Heat Exchangers," Transactions of the American Nuclear Society, 109, pp. 291-294, 2013b.

Bartle, P.M., "Diffusion Bonding: As a Production Process," Welding Institute, Chapter 1, 1979.

Carstens, N., "Control Strategies for Supercritical Carbon Dioxide Power Conversion Systems," Massachusetts Institute of Technology, Ph.D. Dissertation, 2007.

Celik, I., "Procedure for Estimation and Reporting of Discretization Error in CFD Applications," West Virginia University, 2000.

Celik, I. and Karatekin, O., "Numerical Experiments on Application of Richardson Extrapolation with Nonuniform Grids," ASME Journal of Fluid Engineering, 119, pp. 584-590, 1997.

Chen, M., "Design, Fabrication, Testing, and Modeling of a High-Temperature Printed Circuit Heat Exchanger," The Ohio State University, Master Thesis, 2015a.

Chen, M, Kim, I.H., Sun, X., Christensen, R.N., Bartel, N., Utgikar, V., and Sabharwall, P., "Design of Printed Circuit Heat Exchanger for Very High Temperature Reactors," Transactions of the American Nuclear Society, 108, pp. 1090-1093, 2013a.

Chen, M, Kim, I.H., Sun, X., Christensen, R.N., Bartel, N., Utgikar, V., and Sabharwall, P., "Dynamic Response Analysis of a Scaled-Down Offset Strip-Fin Intermediate Heat Exchanger," Transactions of the American Nuclear Society, 109, pp. 270-273, 2013b.

Chen, M., Kim, I.H., Sun, X., Christensen, R.N., Utgikar, V., and Sabharwall, P., "Transient Analysis of an FHR Coupled to a Helium Brayton Power Cycle," Progress in Nuclear Energy, 83, pp. 283-293, 2015b.

Chen, M., Sun, X., and Christensen, R.N., "Numerical Investigation of Thermal Boundary Conditions of a High-Temperature PCHE with Zigzag Flow Channels," 2018 International Congress on Advances in Nuclear Power Plants (ICAPP 18), Charlotte, NC, April 8-11, 2018a.

Chen, M., Sun, X., Christensen, R.N., Shi, S., Skavdahl, I., Utgikar, V., and Sabharwall, P., "Experimental and Numerical Study of a Printed Circuit Heat Exchanger," Annals of Nuclear Energy, 97, pp. 221-231, 2016b.

Chen, M., Sun, X., Christensen, R.N., Skavdahl, I., Utgikar, V., and Sabharwall, P., "Dynamic Behavior of a High-Temperature Printed Circuit Heat Exchanger," Applied Thermal Engineering, 135, pp. 246-256, 2018b.

Chen, M., Sun, X., Christensen, R.N., Skavdahl, I., Utgikar, V., and Sabharwall, P., "Fabrication and Testing of a High-Temperature Printed Circuit Heat Exchanger," Proceedings of the 16th International Topical Meeting on Nuclear Reactor Thermal Hydraulics (NURETH-16), Chicago, IL, August 30 - September 4, 2015c.

Chen, M., Sun, X., Christensen, R.N., Skavdahl, I., Utgikar, V., and Sabharwall, P., "Pressure Drop and Heat Transfer Characteristics of a High-Temperature Printed Circuit Heat Exchanger," Applied Thermal Engineering, 108, pp. 1409-1417, 2016a.

Derby, B. and Wallach, E.R., "Theoretical Model for Diffusion Bonding," Metal Science, 16, pp. 49-56, 1982.

Dhahran, S.A., "Design and Operate a Fouling Monitoring Device to Study Fouling at Twisted Tube," King Fahd University of Petroleum & Minerals, Master Thesis, 2007.

Dostal, V., "A Supercritical Carbon Dioxide Cycle for Next Generation Nuclear Reactors," Massachusetts Institute of Technology, Ph.D. Dissertation, 2004.

Duderstadt, J.J. and Hamilton, L.J., "Nuclear Reactor Analysis," John Wiley & Sons, Inc, 1976.

Figley, J., Sun, X., Mylavarapu, S.K., and Hajek, B., "Numerical Study on Thermal Hydraulic Performance of a Printed Circuit Heat Exchanger," Progress in Nuclear Energy, 68, pp. 89-96, 2013.

Galvez, C., "Design and Transient Analysis of Passive Safety Cooling Systems for Advanced Nuclear Reactors," University of California, Berkeley, Ph.D. Dissertation, 2011.

Garimella, S. and Christensen, R.N., "Heat Transfer and Pressure Drop Characteristics of Spirally Fluted Annuli: Part I: Hydrodynamics," Journal of Heat Transfer, 117, pp. 54-60, 1995.

Garimella, S. and Christensen, R.N., "Heat Transfer and Pressure Drop Characteristics of Spirally Fluted Annuli: Part II: Heat Transfer," Journal of Heat Transfer, 117, pp. 61-68, 1995.

Garimella, S., "Experimental Investigation of Heat Transfer and Pressure Drop Characteristics of Annuli with Spirally-fluted Inner Tubes," The Ohio State University, Ph.D. Dissertation, 1990.

Gezelius, K., "Design of Compact Intermediate Heat Exchangers for Gas Cooled Fast Reactors," Massachusetts Institute of Technology, Master Thesis, 2004.

Heatric, https://www.heatric.com/about.html, Accessed September 2017.

Hesselgreaves, J.E., "Compact Heat Exchangers: Selection, Design and Operation," Gulf Professional Publishing, 2001.

Incropera, F.P., Dewitt, D.P., Bergma, T.L., and Lavine, A.S., "Introduction to Heat Transfer," John Wiley & Sons, 2007.

Khan, H.H., Sharma, A.M., Srivastava, A., and Chaudhuri, P., "Thermal-Hydraulic Characteristics and Performance of 3-D Wavy Channel Based Printed Circuit Heat Exchanger," Applied Thermal Engineering, 87, pp. 519-528, 2015.

Khartabil, H.F. and Christensen, R.N., "An Improved Scheme for Determining Heat Transfer Correlations from Heat Exchanger Regression Models with Three Unknowns," Experimental Thermal and Fluid Science, 6, pp. 808-819, 1992.

Kim, D.E., Kim, M.H., Cha, J.E., and Kim, S.O., "Numerical Investigation on Thermal-Hydraulic Performance of New Printed Circuit Heat Exchanger Model," Nuclear Engineering and Design, 238, pp. 3269-3276, 2008.

Kim, I.H., "Experimental and Numerical Investigations of Thermal-Hydraulic Characteristics for the Design of a Printed Circuit Heat Exchanger (PCHE) in HTGRs," Korea Advanced Institute of Science and Technology, Ph.D. Dissertation, 2012.

Kim, W., Baik, Y.J., Jeon, S., Jeon, D., and Byon, C., "A Mathematical Correlation for Predicting the Thermal Performance of Cross, Parallel, and Counterflow PCHEs," International Journal of Heat and Mass Transfer, 106, pp. 1294-1302, 2017.

Kwon, J.G., Kim, T.H., Park, H.S., Cha, J.E., and Kim, M.H., "Optimization of Airfoil-Type PCHE for the Recuperator of Small Scale Brayton Cycle by Cost-Based Objective Function," Nuclear Engineering and Design, 298, pp. 192-200, 2017.

Lakshmanan, C.C. and Potter, O.E., "Dynamic Simulation of Plate Heat Exchangers," International Journal of Heat and Mass Transfer, 33, pp. 995-1002, 1990.

Lee, S.M. and Kim, K.Y., "Optimization of Zigzag Flow Channels of a Printed Circuit Heat Exchanger for Nuclear Power Plant Application," Journal of Nuclear Science and Technology, 49, pp. 343-351, 2012.

Lee, S.M., Kim, K.Y., and Kim, S.W., "Multi-Objective Optimization of a Double-Faced Type Printed Circuit Heat Exchanger," Applied Thermal Engineering, 60, pp. 44-50, 2013.

Lee, Y. and Lee, J.I., "Structural Assessment of Intermediate Printed Circuit Heat Exchanger for Sodium-Cooled Fast Reactor with Supercritical CO_2 Cycle," Annals of Nuclear Energy, 73, pp. 84-95, 2014.

Losier, C.R.D., Subramanian, S., Ponyavin, V., Chen, Y., Hechanova, A.E., and Peterson, P.F., "The Parametric Study of an Innovative Offset-Strip-Fin Heat Exchanger," Journal of Heat Transfer, 129, pp. 1453-1458, 2007.

Lv, Q., "Design, Testing and Modeling of the Direct Reactor Auxiliary Cooling System for FHRs," The Ohio State University, Ph.D. Dissertation, 2016.

Ma, T., Li, L., Xu, X.Y., Chen, Y.T., and Wang, Q.W., "Study on Local Thermal-Hydraulic Performance and Optimization of Zigzag Type Printed Circuit Heat Exchanger at High Temperature," Energy Conversion and Management, 104, pp. 55-66, 2015.

Manglik, R.M. and Bergles, A.E., "Heat Transfer and Pressure Drop Correlations for the Rectangular Offset Strip Fin Compact Heat Exchanger," Experimental Thermal Fluid Science, 10, pp. 171-180, 1995.

Meshram, A., Jaiswal, A.K., Khivsara, S.D., Ortega, J.D., Ho, C., Bapat, R., and Dutta, P., "Modeling and Analysis of a Printed Circuit Heat Exchanger for Supercritical CO_2 Power Cycle Applications," Applied Thermal Engineering, 109, pp. 861-870, 2016.

MIT, UW Madison, and UC Berkeley Facilitators, "Fluoride-Salt-Cooled, High-Temperature Reactor (FHR) Development Roadmap and Test Reactor Performance Requirements White Paper," Massachusetts Institute of Technology: UCBTH-12-004, 2013.

Mylavarapu, S.K., "Design, Fabrication, Performance Testing, and Modeling of Diffusion Bonded Compact Heat Exchangers in a High-Temperature Helium Test Facility," The Ohio State University, Ph.D. Dissertation, 2011.

Mylavarapu, S.K., Sun, X., and Christensen, R.N., "Hydrodynamically Developing and Fully-Developed Laminar Flows in a Semicircular Duct: Analytical and Computational Analyses," Nuclear Science and Engineering, 182, pp. 319-331, 2016.

Mylavarapu, S.K., Sun, X., Christensen, R.N., Unocic, R.R., Glosup, R.E., and Patterson, M.W., "Fabrication and Design Aspects of High-Temperature Diffusion Bonded Compact Heat Exchangers," Nuclear Engineering and Design, 249, pp. 49-56, 2012.

Mylavarapu, S.K., Sun, X., Figley, J., Needler, N.J., and Christensen, R.N., "Investigation of High-Temperature Printed Circuit Heat Exchangers for VHTRs," Journal of Engineering for Gas Turbines and Power, Transactions of the ASME, 131, pp. 062905-01-07, 2009.

Mylavarapu, S.K., Sun, X., Glosup, R.E., Christensen, R.N., and Patterson, M.W., "Thermal Hydraulic Performance Testing of Printed Circuit Heat Exchangers in a High-Temperature Helium Test Facility," Applied Thermal Engineering, 65, pp. 605-614, 2014.

Nestell, J. and Sam, S., "ASME Code Considerations for the Compact Heat Exchanger," Oak Ridge National Laboratory, ORNL/TM-2015/401, 2015.

Ngo, T.L., Kato, Y., Nikitin, K., and Ishizuka, T., "Heat Transfer and Pressure Drop Correlations of Microchannel Heat Exchanger with S-Shaped and Zigzag Fins for Carbon Dioxide Cycles," Experimental Thermal and Fluid Science, 32, pp. 560-570, 2007.

Nikitin, K., Kato, Y., and Ngo, L., "Printed Circuit Heat Exchanger Thermal-Hydraulic Performance in Supercritical CO_2 Experimental Loop," International Journal of Refrigeration, 29, pp. 807-814, 2006.

Oh, C.H. and Kim, E.S., "Heat Exchanger Design Options and Tritium Transport Study for the VHTR System," Idaho National Laboratory, INL/EXT-08-14799, 2008.

Operation Manual, "Wyko NT9100 Optical Profiler Setup and Operation Guide," Veeco Instruments Inc., 2007.

Pingaud, H., LeLann, J.M., Koehret, B., and Bardin, M.C., "Steady-State and Dynamic Simulation of Plate Fin Heat Exchanger," Computers & Chemical Engineering, 13, pp. 577-585, 1989.

Pra, F., Tochon, P., Mauget, C., Fokkens, J., and Willemsen, S., "Promising Designs of Compact Heat Exchangers for Modular HTRs Using the Brayton Cycle," Nuclear Engineering and Design, 238, pp. 3160-3173, 2008.

Ravindran, P., Sabharwall, P., and Anderson, M.A., "Modeling a Printed Circuit Heat Exchanger with RELAP5-3D for the Next Generation Nuclear Plant," Idaho National Laboratory, INL/EXT-10-20619, 2010.

Roetzel, W. and Xuan, Y., "Dynamic Behavior of Heat Exchangers," WIT Press, 1999.

Sabharwall, P., Clark, D.E., Mizia, R.E., Glazoff, M.V., and McKellar, M.G., "Diffusion-Welded Microchannel Heat Exchanger for Industrial Processes," Journal of Thermal Science and Engineering Applications, 5, 2013.

Sabharwall, P., Kim, E.S., McKellar, M., and Anderson, N., "Process Heat Exchanger Options for Fluoride Salt High Temperature Reactor," Idaho National Laboratory, INL/EXT-11-21584, 2011.

Shah, R.K. and Sekulic, D.P., "Fundamentals of Heat Exchanger Design," John Wiley & Sons, 2003.

Sharifi, F., Narandji, M.R., and Mehravaran, K., "Dynamic Simulation of Plate Heat Exchangers," International Communications in Heat and Mass Transfer, 22, pp. 213-225, 1995.

Skavdahl, I., Utgikar, V.P., Christensen, R., Chen, M., Sun, X., and Sabharwall, P., "Control of Advanced Reactor-Coupled Heat Exchanger System: Incorporation of Reactor Dynamics in System Response to Load Disturbances," Nuclear Engineering and Technology, 48, pp. 1349-1359, 2016a.

Skavdahl, I., Utgikar, V.P., Christensen, R., Sabharwall, P., Chen, M., and Sun, X., "Modeling and Simulation of Control System Response to Temperature Disturbances in a Coupled Heat Exchangers-AHTR System," Nuclear Engineering and Design, 300, pp. 161-172, 2016b.

Song, K.N., "Structural Behavior Analysis on a Small-Scale PCHE Prototype under High-Temperature Gas Loop Conditions," Tech Science Press, 7, pp. 297-305, 2011.

Song, S.C., "Thermal-Hydraulic Performance of a Printed Circuit Heat Exchanger in an Air Test Loop," Korea Advanced Institute of Science and Technology, Master Thesis, 2005.

Special Metals, http://www.specialmetals.com/assets/smc/documents/alloys/inconel/inconel-alloy-617.pdf, Accessed on July 9, 2017.

Thulukkanam, K., "Heat Exchanger Design Handbook," CRC Press, 2013.

Tsuzuki, N., Kato, Y., and Ishiduka, T., "High Performance Printed Circuit Heat Exchanger," Applied Thermal Engineering, 27, pp. 1702-1707, 2007.

U.S. Energy Information Administration (EIA), "International Energy Outlook 2017," IEO2017, 2017.

Wakao, N. and Kaguei, S., "Heat and Mass Transfer in Packed Beds," Gordon and Breach Science Publishers, New York, NY, 364, 1982.

Wang, C., "Design, Analysis and Optimization of the Power Conversion System for the Modular Pebble Bed Reactor System," Massachusetts Institute of Technology, Ph.D. Dissertation, 2003.

Wang, L., Chen, M., Shi, S., Che, D., and Sun, X., "Multi-Objective Optimization of a Printed Circuit Heat Exchanger Design," Proceedings of the 17th International Topical Meeting on Nuclear Reactor Thermal Hydraulics (NURETH-17), Xi'an, China, September 3 - 8, 2017.

Wegman, K.R., "Numerical Modeling of a Printed Circuit Heat Exchanger Based on Experimental Results from the High-Temperature Helium Test Facility," The Ohio State University, Master Thesis, 2016.

Williams, D.F., Toth, L.M., and Clarno, K.T., "Assessment of Candidate Molten Salt Coolants for the Advanced High-Temperature Reactor (AHTR)," Oak Ridge National Laboratory, ORNL/TM-2006/12, 2006.

Xu, X., Ma, T., Lei, L., Zeng, M., Chen, Y., Huang, Y., and Wang, Q., "Optimization of Fin Arrangement and Channel Configuration in an Airfoil Fin PCHE for Supercritical CO_2 Cycle," Applied Thermal Engineering, 70, pp. 867-875, 2014.

Yoon, S.J., O'Brien, J., Chen, M., Sabharwall, P., and Sun, X., "Development and Validation of Nusselt Number and Friction Factor Correlations for Laminar Flow in Semi-Circular Zigzag Channel of Printed Circuit Heat Exchanger," Applied Thermal Engineering, 123, pp. 1327-1344, 2017.

Yoon, S.J., Wegman, K., O'Brien, J., Sabharwall, P., and Sun, X., "An Analytical Methodology to Evaluate Thermal-Hydraulic Performance of Compact Heat Exchangers, Accounting for Heat Loss," Proceedings of International Congress on Advances in Nuclear Power Plants, San Francisco, CA, April 17-20, 2016.

Zhang, X., Sun, X., Christensen, R.N., Anderson, M., and Carlson, M., "Optimization of S-Shaped Fin Channels in a Printed Circuit Heat Exchanger for Supercritical CO_2 Test Loop," The 5th International Supercritical CO_2 Power Cycles Symposium, San Antonio, Texas, March 29-31, 2016.

Zwaan, S.J., Boer, B., Lathouwers, D., and Kloosterman, J.L., "Static Design of a Liquid-Salt-Cooled Pebble Bed Reactor (LSPBR)," Annals of Nuclear Energy, 34, pp. 83-92, 2007.

Appendix

Diffusion-Bonded CHX Design Code

```
%************************************************************************
% One-Dimensional Code for Diffusion-Bonded CHX Designs
%************************************************************************

clear;clc;close all
Q = 600e6;  % Total thermal power, W
thi = 800;  % Hot-side inlet temperature, C
tho = 543;  % Hot-side outlet temperature, C
tci = 520;  % Cold-side inlet temperature, C
tco = 776;  % Cold-side outlet temperature, C
ph = 7e3;   % Hot-side inlet pressure, kPa
pc = 7.9e3; % Cold-side inlet pressure, kPa
Hhi = refpropm('H','T',thi+273.15,'P',ph,'helium');    % Hot-side inlet
Enthalphy, J/kg
Hho = refpropm('H','T',tho+273.15,'P',ph,'helium');    % Hot-side outlet
Enthalphy, J/kg
Hci = refpropm('H','T',tci+273.15,'P',pc,'helium');    % Cold-side inlet
Enthalphy, J/kg
Hco = refpropm('H','T',tco+273.15,'P',pc,'helium');    % Cold-side outlet
Enthalphy, J/kg
mh = Q/(Hhi-Hho);   % Hot-side mass flow rate, kg/s
mc = Q/(Hco-Hci);   % Cold-side mass flow rate, kg/s
Tlm = ((thi-tco)-(tho-tci))/log((thi-tco)/(tho-tci));   % LMTD, C
nc = floor(3.1/2.5e-3);
np = 8440;
c = nc*np;
mhe = mh/(c/2);
mce = mc/(c/2);
d = 2e-3;
dh = pi*d/(pi+2);
ac = 1/2*1/4*pi*d^2;
tp = 1.63e-3;
te = tp-pi/8*d;
k = @(x) 1.554057e-2*x+13.13049;
n = 100;
dt = (thi-tho)/n;
th(1) = thi;
tc(1) = tco;
q1(1) = 1;
reh(1) = 1;
rec(1) = 1;
nuh(1) = 1;
```

```
nuc(1) = 1;
fh(1) = 1;
fc(1) = 1;
hh(1) = 1;
hc(1) = 1;
dph(1) = 1;
dpc(1) = 1;
u(1) = 1;
q2(1) = 1;
q(1) = 1;
dl(1) = 0;
dL(1) = 0;

for i = 1:n
    th(i+1) = th(i)-dt;
    q1(i) = mhe*(refpropm('H','T',th(i)+273.15,'P',ph,'helium')-
refpropm('H','T',th(i+1)+273.15,'P',ph,'helium'));
    reh(i) =
mhe*dh/(refpropm('V','T',(th(i)+th(i+1))/2+273.15,'P',ph,'helium')*ac);
    tc(i+1) =
refpropm('T','H',(refpropm('H','T',tc(i)+273.15,'P',pc,'helium')-
q1(i)/mce),'P',pc,'helium')-273.15;
    rec(i) =
mhe*dh/(refpropm('V','T',(tc(i)+tc(i+1))/2+273.15,'P',pc,'helium')*ac);
    nuh(i) = 4.089+0.0083*reh(i)^0.86054;
    nuc(i) = 4.089+0.0083*rec(i)^0.86054;
    fh(i) = (15.78+0.06677*reh(i)^0.81258)./reh(i);
    fc(i) = (15.78+0.06677*rec(i)^0.81258)./rec(i);
    hh(i) =
nuh(i)*refpropm('L','T',(th(i)+th(i+1))/2+273.15,'P',ph,'helium')/dh;
    hc(i) =
nuc(i)*refpropm('L','T',(tc(i)+tc(i+1))/2+273.15,'P',pc,'helium')/dh;
    u(i) = 1/(1/hh(i)+1/hc(i)+te/k((th(i)+th(i+1)+tc(i)+tc(i+1))/4));
    dl(i+1) = (u(i)*(0.5*pi*d+d)*((th(i)+th(i+1))/2-
(tc(i)+tc(i+1))/2)/q1(i))^-1;
    dph(i) =
4*fh(i)*dl(i)/dh*mhe^2/(2*refpropm('D','T',(th(i)+th(i+1))/2+273.15,'P',ph,'h
elium')*ac^2);
    dpc(i) =
4*fc(i)*dl(i)/dh*mce^2/(2*refpropm('D','T',(tc(i)+tc(i+1))/2+273.15,'P',pc,'h
elium')*ac^2);
    dL(i+1) = sum(dl);
end
L = sum(dl)
dPh = sum(dph)
dPc = sum(dpc)
nuha = mean(nuh)
nuca = mean(nuc)
reha = mean(reh)
reca = mean(rec)
hha = mean(hh)
hca = mean(hc)
ua = mean(u)
Q = sum(q1)*c/2

figure
```

```
plot(dL,th,'r-') % Plot temperature distributin inside the heat exchanger
hold on
plot(dL,tc,'b-')
%************************************************************************
% Design zigzag-channel PCHE using LMTD method
%************************************************************************
clear
close all
clc
%
format short
helium_cp = 5193.0;         % helium specific heat capacity at constant
temperature,J/kg-C

%************************************************************************
**************************
% Thermal Design Data Input

Qest = 600000000;           % thermal duty,W
thi = 800.0;                % hot-side inlet temperature,C
tci = 520.0;                % cold-side inlet temperature,C
phi = 7.0E6;                % hot-side inlet pressure,Pa
pci = 7.9E6;                % cold-side inlet pressure,Pa
tho = 543;                  % hot-side outlet temperature,C
th_mean = (thi+tho)/2.0;    % average temperature on hot side,C
tco = 776;                  % cold-side outlet temperature,C
tc_mean = (tco+tci)/2.0;    % average temmperature on cold side,C
mh = Qest/helium_cp/(thi-tho);
mc = Qest/helium_cp/(tco-tci);  % mass flow rate for both hot and cold
sides,kg/s
%************************************************************************
**************************
% Geometry Parameters of a Zigzag-Channel PCHE
d = 2/1000.0;               % channel diameter,m
dh = pi*d/(2+pi);           % hydraulic diamter,m
pt = 1.63e-3;
%
% Calculate the LMTD
if abs(thi-tho-(tco-tci)) > 20

            lmtd = ((thi-tco)-(tho-tci))/log((thi-tco)/(tho-tci));
else

            lmtd = ((thi-tco)+(tho-tci))/2.0;
end

%%
theta = 15;             % zigzag angle
nhc = floor(3.1/2.5e-3);% number of channels in one plate
nhplate = 8440/2;       % hot-side number of plates
ncplate = 8440/2;       % cold-side number of plates
n = nhplate*nhc;        % total number of channels
vh = mh/(nhplate*nhc)/(1/2*1/4*pi*d^2*helium_rho(th_mean,phi));     %
velocity on hot side,m/s
reh = (helium_rho(th_mean,phi)*dh*vh)/helium_miu(th_mean)           % Reynold
number on hot side
```

```
vc = mc/(ncplate*nhc)/(1/2*1/4*pi*d^2*helium_rho(tc_mean,pci));     %
velocity on cold side,m/s
rec = (helium_rho(tc_mean,pci)*dh*vc)/helium_miu(tc_mean)           % Reynold
number on cold side

sh=(nhplate+ncplate)*pt;% height of the stack,m

%%
% Calculate the thermal-hydraulic performance
% Calculate the Nusselt Number on hot side

% theta=15
    Nuh = 4.089+0.0083*reh^0.86054

% calculate the Nusselt Number on cold side

    Nuc = 4.089+0.0083*rec^0.86054

hh = Nuh*helium_k(th_mean)/dh           % heat transfer coefficient on hot
side,W/m^2-C
hc = Nuc*helium_k(tc_mean)/dh           % heat transfer coefficient on cold
side,W/m^2-C
%
tp_mean = (th_mean+tc_mean)/2.0;        % estimate the mean temperature of
the plate,C
te = pt-pi/8*d;                         % effective plate thickness,m
k = @(x) 1.554057e-2*x+13.13049;        % thermal conductivity of the plate
material,W/m-C
u = 1.0/((1.0/hh)+(1.0/hc)+te/k(tp_mean))    % overall heat transfer
coefficience,W/m^2-C
l = Qest/n/(u*lmtd*(1/2*pi*d+d))        % heat exchanger lengths,m

%% % theta=15
    fh = (15.78+0.06677*reh^0.81258)/reh;
    fc = (15.78+0.06677*rec^0.81258)/rec; % Fanning friction factors
%%
% Calculate pressure drops
dph = 4.0*fh*l/cos(theta*pi/180.0)*helium_rho(th_mean,phi)*(vh^2.0)/(2.0*dh)
dpc = 4.0*fc*l/cos(theta*pi/180.0)*helium_rho(tc_mean,pci)*(vc^2.0)/(2.0*dh)

%% Fluid and solid thermo-physical properties
function [rho] = helium_rho(T,P)
% R is the gas constant for helium in J/kg-K;
% P is the absolute pressure in Pa
% T is temperature, C.

R = 2077.22;             % J/kg-K

C1 = 9.489433e-4;        % m^3/kg
C2 = 9.528079e-4;        % m^3/kg
C3 = 3.420680e-2;        % K^-1
C4 = 2.739470e-3;        % m^3/kg
C5 = 9.409120e-4;        % K^-1

B = C1 + C2./(1-C3*(T+273.15)) + C4./(1 + C5*(T+273.15));
```

```
rho = P./(R.*(T+273.15) + P.*B); % rho is the density of helium in kg/m^3

end
%=========================================================================
% Yields the thermal conductivity (W/m-C) of Helium at temperature (C)
function [k] = helium_k(T)

k = 2.774*10^(-3).*(T+273.15)^0.701;

end
%=========================================================================
% Yields Dynamic viscosity [N-s/m^2] or [Pa-s] or [kg/m-s] at T (C)
function miu=helium_miu(T)

miu = 3.953*10^-7*((T+273.15).^0.687);

end
%=========================================================================
% Yields the Prandtl number of He gas at Tempearture (C)
function [Pr]=helium_pr(T)

Pr = 0.740*(T+273.15)^-0.014;

end
%=========================================================================
% Yields the thermal conductivity of Alloy 617 at Tempearture (C)
% Density of Alloy 617 is 8360 kg/m^3.
function [k] = alloy617_k(T)

k = 0.0155*T+13.115;

end
```